UNIVERSITY OF CALIFORNIA SAN DIEGO

# Bottom-up Design of Magnetic and Magnetoresistive Materials Using Colloidal Nanoparticles

A dissertation submitted in partial satisfaction of the requirements for
the degree Doctor of Philosophy

in

Materials Science and Engineering

by

Benjamin H. Zhou

Committee in charge:

Professor Jeffrey D. Rinehart, Chair
Professor Renkun Chen
Professor Eric Fullerton
Professor Javier Garay
Professor Alina Schimpf

2022

This dissertation of Benjamin H. Zhou is approved, and it is acceptable in quality and form for publication on microfilm and electronically.

University of California San Diego

2022

# DEDICATION

*To my father*

# TABLE OF CONTENTS

# LIST OF FIGURES

# LIST OF TABLES

# ACKNOWLEDGEMENTS

I must first thank my advisor, Jeff Rinehart. I greatly admire his unending enthusiasm and scientific curiosity, which created a research environment where I was emboldened to pursue all the strands of thought that occurred to me.

I am grateful to all the members of the Rinehart group. Firstly, my seniors Jeremy Hilgar and Yijun Xie, both of whom I learned to be a graduate student from. I have aspired to Jeremy's dedication to experimentation and Yijun's tireless work ethic. To Kyle Kirkpatrick, Phil Bunting and Tara Zand, research was brightened by your fellow enthusiasm for nanomaterials. To Alex Mantanona, Max Bernbeck, and Angelica Orlova, it's been a pleasure working alongside you and admiring your crystal structures. To my undergraduate researchers, Yoyo Wang and Lee Elmont, mentoring you was a great growth experience for me; I only hope that you found the experience valuable as well.

Among my friends, I thank Mike Neville and Joey Palomba for their camaraderie as young, naïve graduate students. I also must thank Daniel Dolan, Sean Emery, and Xiafei Zhang for nearly twenty years of dependable friendship.

I thank Joanne Chan for her unwavering support and enthusiasm. It is no coincidence that my research prospered after we met.

Lastly, I thank my family for their neverending care. I especially thank my father, whose words, experiences, and attitude I perpetually look to for inspiration.

---

Chapter 3, in full, is currently being prepared as a manuscript for publication by Zhou, B.H. and Rinehart, J.D. The dissertation author was the principal researcher and author of this material.

Chapter 4 is a reformatted reprint from the manuscript entitled "A Size Threshold for Enhanced Magnetoresistance in Colloidally Prepared $CoFe_2O_4$ Nanoparticle Solids" by Zhou, B.H. and Rinehart, J.D. The dissertation author was the primary researcher and author of this paper. Reprinted with permission from *ACS Cent. Sci.* **2018**, *4*,1222–1227. Copyright 2018 American Chemical Society.

Chapter 5 is a reformatted reprint from the manuscript entitled “Pseudo Spin Valve Behavior in Prepared Nanoparticle Films” by Zhou, B.H. and Rinehart, J.D. The dissertation author was the primary researcher and author of this paper. Reprinted with permission from *ACS Appl. Electron. Mater.* **2019**, *1*,1065–1069. Copyright 2019 American Chemical Society.

# VITA

2022 Doctor of Philosophy, University of California San Diego

2016 Master of Science, University of California San Diego

2014 Bachelor of Science, University of California, Irvine

## Publications

**Zhou, B.H.**; Rinehart, J.D. "Colloidal Dipolar Ferromagnetism Held Together by Antiferromagnetic Glue" *in prep.*

**Zhou, B.H.**; Rinehart, J.D. "Pseudo Spin Valve Behavior in Colloidally Prepared Nanoparticle Films" *ACS Appl. Electron. Mater.* **2019**, *1*, 1065–1069.

**Zhou, B.H.**; Rinehart, J.D. "A Size Threshold for Enhanced Magnetoresistance in Colloidally Prepared $CoFe_2O_4$ Solids" *ACS Cent. Sci.* **2018**, *4*, 1222–1227.

Adelani, P.O.; Duke, A.N.; **Zhou, B.H.**; Rinehart, J.D. "Role of Magnetic Concentration in Modulating the Magnetic Properties of Ultra-Small FePt Nanoparticles" *Inorganica Chim. Acta*, **2017**, *460*, 114–118.

Avery, A.D.; **Zhou, B.H.**; Lee, J.; Lee, E.; Miller, E.M.; Ihly, R.; Wesenberg, D.; Mistry, K.S.; Guillot, S.L.; Zink, B.L.; Kim, Y.; Blackburn, J.L.; Ferguson, A.J. "Tailored Semiconducting Carbon Nanotube Networks with Enhanced Thermoelectric Properties" *Nature Energy*, **2016**, *1*, 16033.

# ABSTRACT OF THE DISSERTATION

Bottom-up Design of Magnetic and Magnetoresistive Materials Using Colloidal Nanoparticles

by

Benjamin H. Zhou

Doctor of Philosophy in Materials Science and Engineering

University of California San Diego 2022

Professor Jeffrey Rinehart, Chair

Colloidal nanoparticles are an exciting class of materials for their ability to act as tunable building blocks for larger scale materials. The application of nanotechnology to magnetic materials depends on the controlled synthesis of uniform nanoparticles with targeted magnetization and magnetic anisotropy. The work presented in this dissertation has two focuses: one, the development of synthetic techniques which allow for the consistent production of uniform nanoparticles and of novel heterostructured nanoparticles with emergent magnetism, and two, the application of these nanoparticles into bulk magnetic and magnetoresistive assemblies.

A common issue which plagues the study of nanoparticles is the variability of synthesis from written protocol to laboratory practice or even from batch to batch. A set of techniques are detailed which have been developed to ensure consistent recreation of reaction conditions which allow for separate LaMer 'burst' nucleation and growth regimes during synthesis. High-quality, single-phase nanoparticles

synthesized using the preceding techniques were further used as seeds in the synthesis of novel heterostructured nanoparticles exhibiting enhanced exchange bias.

Collective magnetism was studied in assemblies of ferrimagnetic $Fe_3O_4$ and antiferromagnetic CoO nanoparticles. In typical samples consisting only of permanent magnetic nanoparticles, dipolar interactions between the nanoparticles frustrate the orientation of their magnetic moments, often producing a superspin glass state. Conversely, antiferromagnetic nanoparticles, in their dipolar interactions with ferro- or ferrimagnetic nanoparticles, induce a uniaxial magnetic anisotropy and create a superferromagnetic state in the collective magnetism of the nanoparticle assembly.

Synthetic control over nanoparticle morphology was exploited to engineer nanoparticles for the assembly of granular magnetoresistance devices. Magnetoresistance measurements on a series of pellets of differently sized $CoFe_2O_4$ nanoparticles revealed a size threshold beyond which magnetoresistance was greatly diminished. Additionally, the magnetoresistance of $CoFe_2O_4$ was found to be superior to that of $Fe_3O_4$ despite the latter's popularity in magnetoresistance research. Magnetoresistance measurements were also performed on mixed nanoparticle films cast from nanoparticle inks. Tuning of the $CoFe_2O_4$ to $Fe_3O_4$ ratio in the films successfully produced pseudo spin valve magnetoresistance, improving both the magnitude and responsivity of the films' magnetoresistance.

# Chapter 1

# Introduction

## 1.1 New Materials Built through Nanoscience

The overarching theme of my research, dating to before I started graduate school, has been the bottom-up design of materials through the use of nanomaterials. Under this ideal, materials could be pieced together from a multitude of nanoscale building blocks similarly to the superparticle shown in Figure 1.1, combining the individual properties of each building block or even giving rise to emergent properties. The basis of materials engineering is that the structure of a material determines its properties. Structure is effective from atomic scale bonding all the way up to the macroscopic structure of a material that is visible to the human eye. For example, the highly delocalized electronic bonding of metals give them their characteristically high thermal conductivity and ductility. At the macroscopic level, a scratch in a piece of glass can greatly reduce the stress at which the glass fractures. In the past century, the emergence of nanotechnology has enabled a new level of manipulation of materials, at the nanoscale.

Two impactful effects result from the implementation of materials in the range of 1 to 100 nm: the influence of a material's size on its properties and the increased influence of the material's surface. In a bulk material, there are essentially an infinite number of atoms, and the removal or addition of atoms does not affect its intrinsic properties. At the nanoscale, a change in size leads to a significant change in the number of atoms and a significant change to the material properties. Additionally, the dimensions of

nanomaterials overlap with other important physical length scales, notably the exciton Bohr radius as well as the wavelengths of phonons and ultraviolet and visible light. Varying sizes of the same material can therefore interact with other physical phenomena in different ways, *e.g.* the size-tunable emission of visible light from quantum dots.

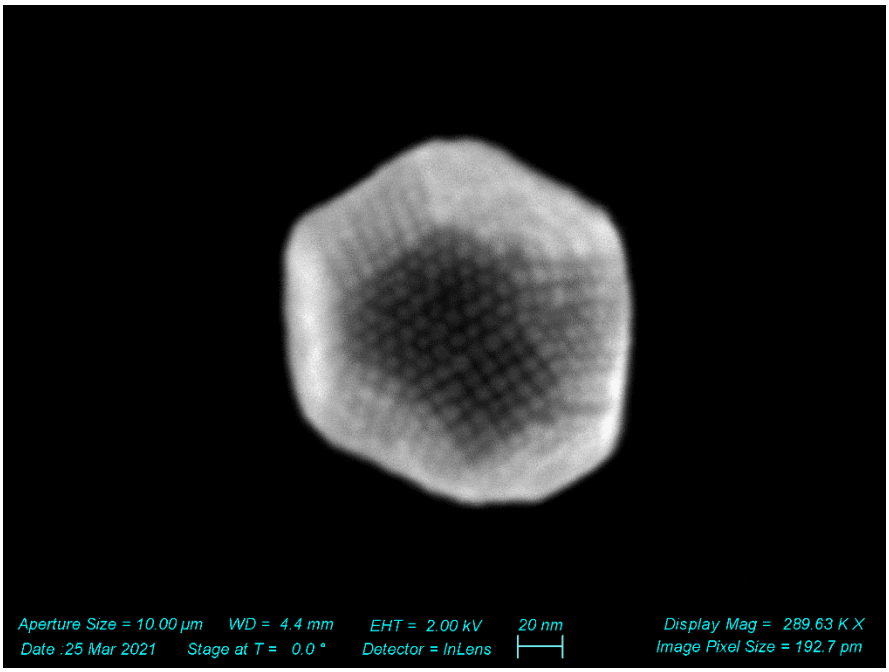


**Figure 1.1.** Scanning electron micrograph of a crystalline superparticle comprised of $Fe_3O_4$ nanoparticles.

The surface of a material has a deterministic role in its chemical reactions and transport phenomena. The atoms at the surface of a material differ inherently from those in the interior bulk, owing to their different coordination environment. The surface atoms are under-coordinated, increasing their reactivity, enhancing their diffusivity, altering their spin orientation, *etc*. The importance of the surface atoms also implies that a nanoparticle's shape can affect its properties based on the different coordination environments present on different facets and edges. These surface effects are more pronounced in nanomaterials, whose ratio of surface atoms to bulk atoms is orders of magnitude greater than for macroscopic materials. A cube of material with side length 1 m and volume of 1 $m^3$ has a surface area of 6 $m^2$. If divided instead into cubes with side length 1 nm, all the 1 nm cubes comprising that same volume have a total surface area of $6x10^9$ $m^2$.

## 1.2 Colloidal Nanoparticles

Colloidal nanoparticles are an expression of nanomaterials which are produced through solution-based chemistry, and which can remain in liquid suspensions for further convenient processing. Two key attributes of colloidal synthesis are its scalability and precision, which set it apart from top-down production methods. Subtractive methods based on lithography are precise but can produce nanoparticles only at wafer-scale and which are immobilized on a substrate.[1-2] On the other hand, milling techniques can produce large amounts of nanoparticles, but with limited control over particle morphology.[3-4] In particular, the colloidal synthesis of inorganic nanoparticles has been highly developed within the past 70 years.[5-8] These colloidal, inorganic nanoparticles are more accurately understood as the combination, depicted in Figure 1.2, of an inorganic core with a 'shell' of ligands coordinated to its surface. These ligands stabilize the surface of the nanoparticle and interact with solvents to stably suspend the nanoparticles in liquid solutions. The most common ligands consist of amphiphilic molecules whose polar headgroup coordinates to the nanoparticle surface, and whose nonpolar tail impart stable suspension in nonpolar solvents like hexane or toluene. Alternatively, charged molecules can form an electrical double layer at the nanoparticle surfaces, suspending the nanoparticles in solvents with high relative permittivity.

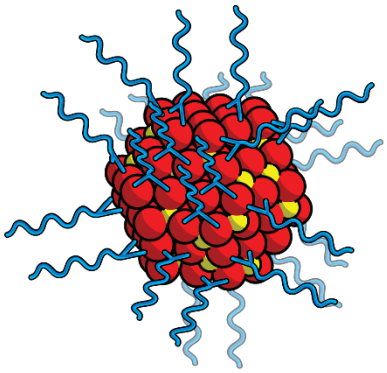

**Figure 1.2.** A depiction of a colloidal, inorganic nanoparticle. The inorganic core is comprised of atoms (red and yellow balls) configured in a crystalline lattice. At the surface of the inorganic core are ligands (blue lines) which coordinate to the surface and interact with the solvent.

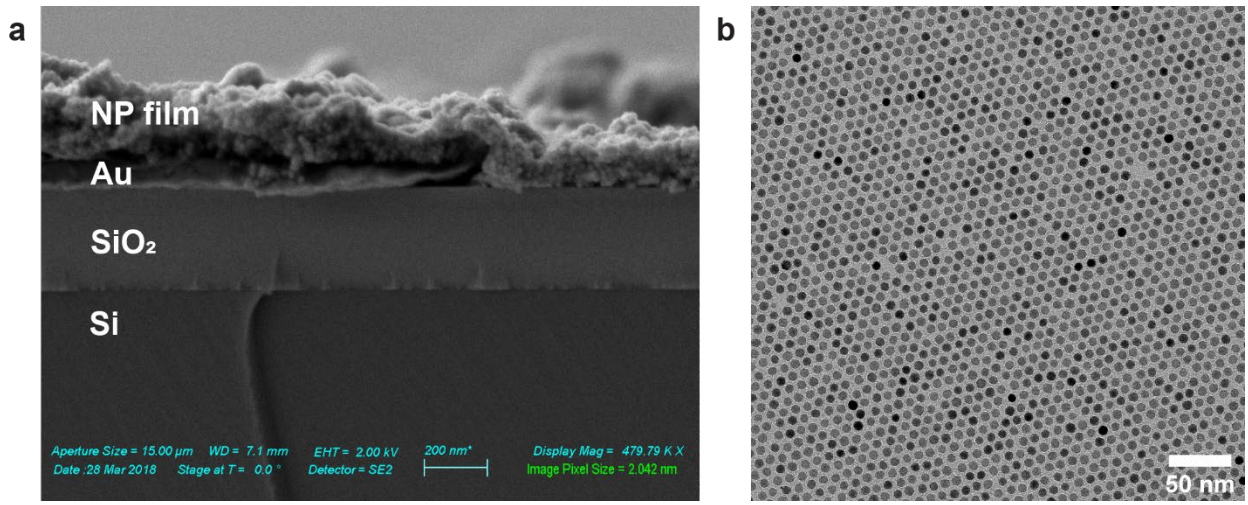


**Figure 1.3.** a) Scanning electron micrograph of a disordered nanoparticle film dropcast onto a gold electrode device. b) Transmission electron micrograph of a crystalline two-dimensional nanoparticle superlattice.

The suspendability of colloidal nanoparticles readily allows for their self-assembly into bulk material forms. Thin films which can be integrated with the planar devices that are ubiquitous in semiconductor research can be made through a number of convenient methods: dropcasting, spin coating, dip coating, or doctor blading. An example of a dropcast nanoparticle film is shown in Figure 1.3a; this film was dropcast onto a silicon substrate with gold electrode pattern to form a magnetoresistance device. For further sophistication, crystalline superlattice films like the one shown in Figure 1.3b can be made based on controlled evaporation of nanoparticle suspensions.[9-11] Three-dimensional assemblies result from evaporation of nanoparticle suspensions confined in microemulsion droplets,[12-14] *e.g.* the superparticle shown in Figure 1.1, or through controlled interactions between nanoparticle ligands.[15] Colloidal nanoparticles can even be utilized in inks for inkjet printing of functional devices, which could result in faster, cheaper production of electronic devices; printing of nanoparticle inks can also be done on flexible substrates, an advancement over the rigid planar substrates that are currently dominant.[16] The development of these solution-deposited assemblies over the past few decades has realized the potential of nanoparticles to generate new materials and properties from the bottom up.[17-19]

## 1.3 Magnetism in Nanoparticles

Size, shape, surfaces and interfaces are all crucial factors in magnetism, and so throughout the history of nanomaterials, they have strongly impacted the properties of magnetic materials. The following sections will detail the key effects which affect magnetism at the nanoscale.

### 1.3.1 Defining the Magnetic State of a Material

Magnetic materials can be classified as ferromagnetic, ferrimagnetic, or antiferromagnetic. In a ferromagnet the localized spin of each atom couples with the others such that they are all aligned with each other, leading to a permanent magnetic moment in the material. Conversely, in an antiferromagnet, the atomic spins are divided into two or more spin sublattices which are anti-aligned to each other, producing a permanent, ordered magnetic state which has no net moment. Finally, a ferrimagnet also consists of two or more spin sublattices which are anti-aligned to each other, but the sublattices are unequal and the material retains a net magnetic moment. Due to their permanent moment, ferrimagnets behave similarly to ferromagnets. The following discussion pertains primarily to ferro- and ferrimagnetic nanoparticles, which find the most use in magnetic applications.

To understand the behavior of these magnetic materials, we must understand the various energies which govern their magnetic state, which are described by the equations below:

$$E_{Zeeman} = -\boldsymbol{m} \cdot \boldsymbol{H} \qquad \textbf{Equation 1.1}$$

$$E_{MCA,u} = KVsin^2(\theta) \qquad \textbf{Equation 1.2}$$

$$E_{demag} = -\frac{\mu_0}{2}\int_{volume} \boldsymbol{M} \cdot \boldsymbol{H_d} dV \qquad \textbf{Equation 1.3}$$

$$E_{exchange} = \int_{volume} \frac{A}{M_s}(\nabla \boldsymbol{M}(\boldsymbol{r}))d^3r \qquad \textbf{Equation 1.4}$$

The first is the Zeeman energy, $E_{Zeeman}$, which develops in response to an externally applied magnetic field and is described by Equation 1.1, where $\boldsymbol{m}$ is the magnetic moment vector and $\boldsymbol{H}$ is the applied field vector. The result of the Zeeman energy is that the moment of the material tends to align with the direction of the applied field.

The second energy is the magnetocrystalline anisotropy energy, $E_{MCA}$, which results from the symmetry of the crystal structure of the material. In a physical sense, $E_{MCA}$ gives the moment of a material one or more preferred orientations, or easy axes, relative to the crystal lattice. The mathematical expression for $E_{MCA}$ differs depending on the crystal system; only the equation for systems with uniaxial anisotropy is shown (Equation 1.2). In Equation 1.2, $K$ is the anisotropy constant, a material constant, $V$ is the volume of the material, and $\theta$ is the angle between the magnetic moment and the easy axis.

An energy which depends on the shape of the material is the demagnetizing field energy, $E_{demag}$, described by Equation 1.3, where $\mu_0$ is the vacuum permeability, $\boldsymbol{M}$ is the magnetization vector field of the material, $\boldsymbol{H_d}$ is the demagnetizing field, and $V$ is the volume of the material. To minimize $E_{demag}$, the material's moment will orient itself with the longest dimensions of the materials. For a rod, the moment will align with the rod axis, while in a thin film, the moment may align in any in-plane direction. On the other hand, in a completely isotropic sphere, the moment has no preferred direction. Another possibility to minimize $E_{demag}$ is to split the material into domains whose magnetizations are oriented in alternating directions. The domain structure minimizes the magnitude of $\boldsymbol{H_d}$, thus minimizing $E_{demag}$.

The final major energy is the exchange energy, $E_{ex}$, described by Equation 1.4, where $M_S$ is the magnitude of the magnetization, $\boldsymbol{r}$ is a vector denoting a position within the material, and $\boldsymbol{M}(\boldsymbol{r})$ is the magnetization vector at position $\boldsymbol{r}$. $A$ is the exchange stiffness, a parameter which is proportional to the exchange constant, $J$, and which describes how strongly two neighboring atomic spins are aligned with each other. By itself, $E_{ex}$ favors the uniform magnetization of a material throughout its volume. In a real material, it competes with the $E_{demag}$ and $E_{MCA}$; the balance between these energies gives rise to the complex domain structures of bulk magnets.

### 1.3.2 Defining the Magnetic State of a Single Nanoparticle

The magnetism of most magnetic nanoparticles can be understood through $E_{Zeeman}$, $E_{MCA}$, and $E_{demag}$, because the nanoparticles are too small to form multiple domains.[20] Furthermore, many nanoparticles are found in isotropic forms like spheres, truncated octahedra, or cubes, removing the influence of $E_{demag}$. Thus,

the magnetic state of a nanoparticle can be approximated by the picture in Figure 1.4a – a typical nanoparticle has a single domain with a uniform magnetic moment which orients itself with the easy axes of the material in the absence of a field. The moment must overcome an energy barrier set by $E_{MCA}$ to rotate between the energetically equivalent easy directions of the material. As an increasing magnetic field is applied, the applied field stabilizes a particular direction and destabilizes the opposite; when a large enough field (red curve, Figure 1.4b) is applied, the moment of the nanoparticle can easily flip to the direction of the field.

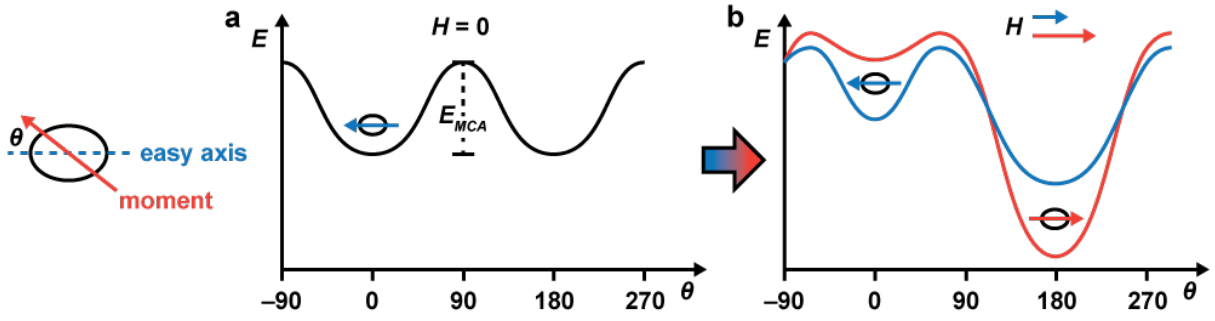


**Figure 1.4.** Schematic of energy of a nanoparticle's moment for different orientations relative to its easy axis. a) When no magnetic field is applied, both easy axis directions are equivalent. b) One direction is favored when a magnetic field is applied. For small fields (blue), the energy barrier between the two easy axis directions is large and the moment is trapped in its original direction. At larger fields (red) the moment's original direction is destabilized enough for it to rotate to the field direction.

The energy barrier resulting from $E_{MCA}$ is the basis for magnetic hysteresis in nanoparticles. That is, the resulting magnetic state of a material after applying a field is dependent on its original state. For example, if the nanoparticle in Figure 1.4a started with a right-pointing moment and the blue magnetic field in Figure 1.4b was applied, the nanoparticle would end with a right-pointing moment, rather than left-pointing as is depicted in Figure 1.4b. The hysteresis of a material is characterized by its coercivity, $H_c$, and remanence, $M_r$, which are depicted in Figure 1.5a. The coercivity is the applied field required to reverse a material's magnetization from one direction to the other, while the remanence is the permanent magnetization left in a material when the applied field is removed. $H_c$ and $M_r$ are found by measuring the magnetization of the material as magnetic field is scanned forward and back between a large negative field and a large positive field. The coercivity of nanoparticles is determined by the competition between $E_{MCA}$

and $E_{Zeeman}$. A nanoparticle with a large moment will favor the orientation determined by the applied field, while a nanoparticle with a large magnetocrystalline anisotropy energy will favor the easy axis orientations. Because $E_{MCA}$ is proportional to the nanoparticle volume, different sized nanoparticles of the same material have very different coercivities (Figure 1.6). At the nanoscale, thermal energy is of comparable scale to $E_{MCA,}$ and nanoparticle moments are able undergo thermally assisted rotation over the barrier at lower applied fields. For example, a 10 nm wide, spherical $Fe_3O_4$ nanoparticle has an anisotropy barrier of $5.8\times10^{-21}$ J compared to a thermal energy $k_BT$ of $4.1\times10^{-21}$ J at room temperature, where $k_B$ is the Boltzmann constant and $T$ is temperature. On the other hand, a 5 nm wide, spherical $Fe_3O_4$ nanoparticle has a barrier of only $7.2\times10^{-21}$ J. The 10 nm nanoparticle will have a reduced coercivity from a larger nanoparticle, but the 5 nm nanoparticle will have no coercivity at all at room temperature. There is enough thermal energy for the nanoparticle's moment to rotate freely over the barrier through any orientation; in the absence of an applied field, this free rotation causes the nanoparticle to have no net measurable moment. This new magnetic state in small nanoparticles is called superparamagnetism.

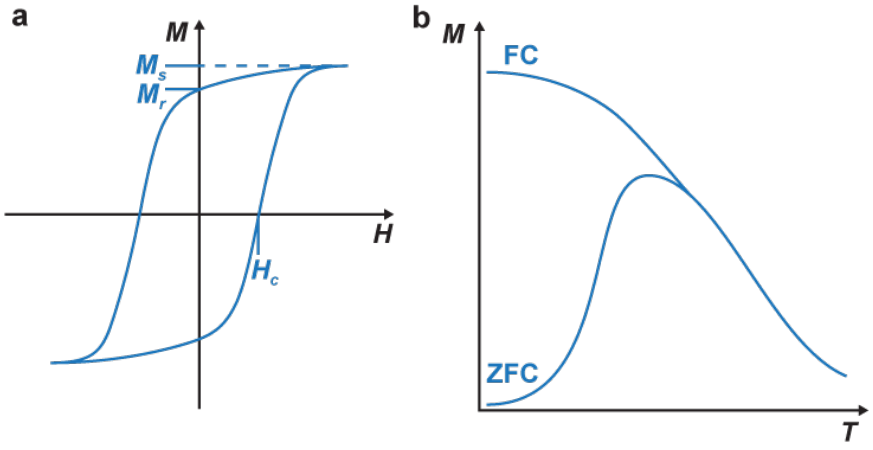


**Figure 1.5.** Schematics of the dependence of magnetization on a) magnetic field and b) temperature in ferro- or ferrimagnetic nanoparticles. Also depicted are key magnetic parameters: coercivity ($H_c$), saturation magnetization ($M_s$), and remanent magnetization ($M_r$). The two curves in b) are warming curves measured after cooling in zero field (ZFC) or a finite field (FC).

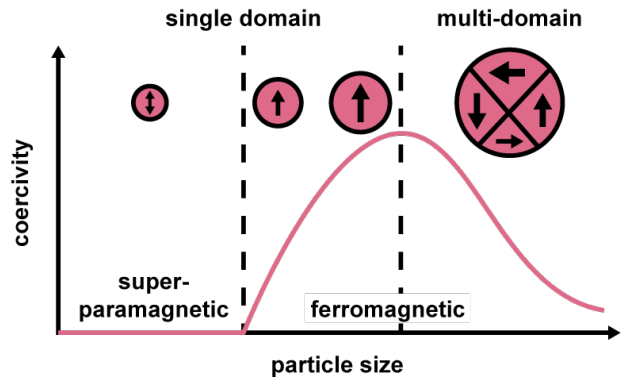


**Figure 1.6.** Schematic of the effect of a particle's size on its coercivity and magnetic state.

The size-dependent magnetism of nanoparticles can be further characterized by the temperature dependence of their magnetization (Figure 1.5b). Typically, the magnetization is measured in a small, applied field as the temperature is increased. This measurement is done after cooling without an applied field (zero field cooled, ZFC) or after cooling with an applied field (field cooled, FC). The ZFC magnetization of an ensemble of nanoparticles is zero at low temperatures. The nanoparticle moments are randomly oriented without the influence of an applied field and cancel each other out, a configuration which is frozen in place upon cooling. Because the applied field is small, it cannot reorient the nanoparticle moments over their anisotropy barriers. As thermal energy is added back to the system with increasing temperature, the effective barrier shrinks, and the nanoparticle moments begin to align themselves with the field direction. As the temperature is further increased, the nanoparticles' anisotropy barriers are overtaken by thermal energy and the nanoparticles transition to the superparamagnetic state. At these temperatures, the ZFC magnetization begins to decrease as the orientation of their moments fluctuates more and more. When a magnetic field is applied to the superparamagnetic nanoparticles at high temperatures, their moments are biased in the direction of the field. This aligned configuration is frozen in under FC conditions and the FC magnetization is large at low temperatures. Increasing temperature decreases the FC magnetization as thermal energy allows the moments' orientations to fluctuate. With further increasing temperature, the nanoparticles become superparamagnetic, and the FC magnetization converges with the ZFC magnetization. Where there is a large splitting between the ZFC and FC magnetizations, the nanoparticles are considered 'blocked' and they display hysteresis in their magnetization vs field curves.

Where the ZFC and FC magnetizations overlap, the nanoparticles are 'unblocked' superparamagnets. The transition temperature between these two regimes known as the blocking temperature, $T_B$, reflects the magnitude of $E_{MCA}$ as well as the size of the nanoparticles.

A final size-dependent property of magnetic nanoparticles is their saturation magnetization, $M_s$, shown in Figure 1.5a. $M_s$ is the sum of all the atomic spins in a material, and is considered an intrinsic property in bulk materials. However, the surface atoms of a nanoparticle may become decoupled and disoriented from the bulk atoms. Thus, the moments of the surface atoms may not contribute or even detract from the total magnetization of the nanoparticle. Differently sized nanoparticles will therefore display different saturation magnetizations owing to their relative numbers of surface atoms.

### 1.3.3 Magnetism of Many Interacting Nanoparticles

In most real devices or samples based on magnetic nanoparticles, the nanoparticles are packed closely together, and their moments can interact with each other. Therefore, the magnetism of an assembly of nanoparticles can deviate significantly from the individual magnetic properties of its constituents. The two ways that the nanoparticles can interact magnetically are through exchange coupling and dipolar coupling.

$$E_{ex,interNP} = -J\,\boldsymbol{m_1}\cdot\boldsymbol{m_2} \qquad \textbf{Equation 1.5}$$

$$E_{dipolar} = -\frac{\mu_0}{4\pi|\boldsymbol{r}|^3}[3(\boldsymbol{m_1}\cdot\hat{\boldsymbol{r}})(\boldsymbol{m_2}\cdot\hat{\boldsymbol{r}}) - \boldsymbol{m_1}\cdot\boldsymbol{m_2}] \qquad \textbf{Equation 1.6}$$

Exchange coupling involves the alignment of two adjacent moments, $\boldsymbol{m_1}$ and $\boldsymbol{m_2}$, with a coupling strength of $J$ (Equation 1.5). In colloidal nanoparticles, the existence of exchange coupling requires close contact between their inorganic cores. However, the nanoparticles' surface ligands typically keep them too far apart to observe exchange coupling. Dipolar coupling is a long-range effect which affects almost all collections of nanoparticles. The dipolar coupling energy $E_{dipolar}$ is described by Equation 1.6, where $\mu_0$ is the vacuum permeability, $\boldsymbol{r}$ is the vector from one nanoparticle to the other, $\hat{\boldsymbol{r}}$ is a unit vector collinear to $\boldsymbol{r}$, and $\boldsymbol{m_1}$ and $\boldsymbol{m_2}$ are the nanoparticles' moments. When $\boldsymbol{r}$ is orthogonal to $\boldsymbol{m_1}$ and $\boldsymbol{m_2}$, $E_{dipolar}$ favors anti-alignment of the moments, while ferromagnetic alignment of the moments is favored when $\boldsymbol{r}$, $\boldsymbol{m_1}$, and $\boldsymbol{m_2}$

are all parallel. The complexity of dipolar coupling means that the orientation of a collection of magnetic nanoparticles has a complex energy landscape with many orientationally frustrated, metastable energy wells. The effects of interparticle dipolar interactions will be discussed in more detail in Chapter 3.

## 1.4 Giant and Tunneling Magnetoresistance

Magnetoresistance describes several physical phenomena which alter the electrical resistance of a material in response to the application of a magnetic field. The implementation of nanomaterials in magnetoresistance devices has driven the discovery of increasingly sensitive magnetoresistance effects, from anisotropic magnetoresistance (AMR) to giant magnetoresistance (GMR) and continuing to tunnel magnetoresistance (TMR). The $\Delta R/R_{max}$ (where $R_{max}$ is the maximum resistance, which occurs at zero applied field, and $\Delta R$ is the difference between the resistance at a given magnetic field, $R$, and $R_{max}$) possible in these devices has increased by orders of magnitude, from a couple percent in AMR to tens of percent in GMR and hundreds of percent in TMR.[21-23] In turn, the implementation of magnetoresistance devices in hard drive read heads is partly responsible for the exponential growth in data storage density that occurred in the past few decades. The technological importance of these new magnetoresistance effects led to the award of the 2007 Nobel Prize in Physics to the discoverers of GMR.[24-25] The basic structure which is necessary to produce GMR and TMR is a nanoscale trilayer device of two magnetic materials separated by

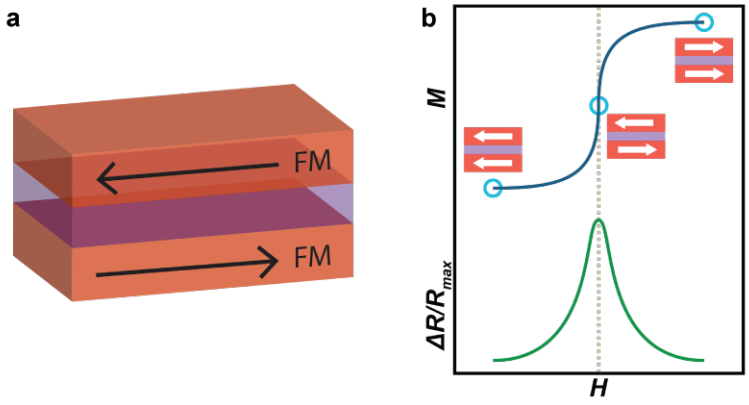


**Figure 1.7.** Illustrations of a) a trilayer of two magnetic materials (FM) separated by a nonmagnetic material (middle purple layer) and the dependence of b) the magnetization ($M$) and magnetoresistance ($\Delta R/R_{max}$) on magnetic field for such a device.

a nonmagnetic spacer (Figure 1.7a). For both GMR and TMR, the resistance of the device depends on the relative orientation of the moments of the two magnetic layers. As shown in Figure 1.7b, when the layers' moments are aligned, the device has low resistance, but when the layers' moments are anti-aligned, the device has high resistance. This change in resistance can be understood through the lens of a parallel, two current model, in which electrons flow through the devices through two channels, one for each of the spin types of the electrons. When the magnetic layers are anti-aligned, both spin channels allow only a low current, giving a high device resistivity. When the magnetic layers are aligned, the majority spin channel allows a large current while the minority spin channel has a low current; overall, the device has a low resistivity. In a GMR device, the spacer is metallic, and the majority and minority spin channels are controlled by spin dependent scattering. Meanwhile, in TMR, the spacer is insulating, and the spin channels are subject to spin dependent tunneling.

Soon after the discovery of GMR in thin film multilayers, it was also produced in granular materials.[26-27] These materials consisted of magnetic grains dispersed within a nonmagnetic, metallic matrix; they were first produced by phase segregation of immiscible Cu-Co alloys. As with thin film multilayers, replacement of the metallic matrix with an insulating one produced TMR in these granular materials.[28] Pairs of adjacent magnetic grains separated by the nonmagnetic matrix emulate the basic trilayer structure in thin film GMR devices. While the structure and interfaces in these granular GMR materials could not match the precision of thin film devices, the sheer number of magnetic grains and interfaces between them allowed the granular materials to approach the thin films' sensitivity. In recent years, the development of colloidal nanoparticle synthesis has jumpstarted the study of magnetoresistance in granular materials.[29-33] Magnetic nanoparticles can now be produced with precise size, shape, facets, *etc*. and assembled into structures with much more controlled interfaces. These nanoparticle assemblies have the potential to multiply the magnetoresistance of a precise interface by the large numbers of participating particles. Excitingly, these nanoparticles possess a rich parameter space with which to engineer magnetoresistance that has yet to be fully explored.

## 1.5 Organization of Chapters

The following chapters detail our efforts to build magnetoresistance and magnetic materials with rationally prepared colloidal nanoparticles. Chapter 2 covers the development of synthetic techniques to enable production of a variety of monodisperse nanoparticles with well-defined size and shape dependent properties. These single-phase nanoparticles were then used as seeds to create heterostructured nanoparticles exhibiting enhanced exchange bias. The study of exchange bias also led to the study in Chapter 3, of mixed assemblies of antiferromagnetic nanoparticles and ferrimagnetic nanoparticles. We discovered that the antiferromagnetic nanoparticles induced a superferromagnetic state with enhanced coercivity, despite a lack of strong exchange coupling with the ferrimagnetic nanoparticles. The success of the synthetic techniques in Chapter 2 also led to the study in Chapter 4, of the magnetoresistance in a size series of an understudied material, $CoFe_2O_4$. This size series study revealed a threshold for large $\Delta R/R_{max}$ which could serve as an important design criterion for future materials. In Chapter 5, we combined $CoFe_2O_4$ nanoparticles with $Fe_3O_4$ nanoparticles to realize the pseudo spin valve structure in a granular material, improving not only the magnitude $\Delta R/R_{max}$ but also its responsivity.

## 1.6 References


1. Bedanta, S.; Seki, T.; Iwama, H.; Shima, T.; Takanashi, K., Superferromagnetism in Dipolarly Coupled $L1_0$ FePt Nanodots with Perpendicular Magnetization. *Appl. Phys. Lett.* **2015,** *107* (15).

2. Susarrey-Arce, A.; Czajkowski, K. M.; Darmadi, I.; Nilsson, S.; Tanyeli, I.; Alekseeva, S.; Antosiewicz, T. J.; Langhammer, C., A Nanofabricated Plasmonic Core–Shell-Nanoparticle Library. *Nanoscale* **2019,** *11* (44), 21207-21217.

3. Goya, G. F., Handling the Particle Size and Distribution of $Fe_3O_4$ Nanoparticles through Ball Milling. *Solid State Commun.* **2004,** *130* (12), 783-787.

4. Salah, N.; Habib; Khan; Memic; Azam; Al, H.; Zahed; Habib, High-Energy Ball Milling Technique for ZnO Nanoparticles as Antibacterial Material. *Int. J. of Nanomedicine* **2011**.

5. Brust, M.; Walker, M.; Bethell, D.; Schiffrin, D. J.; Whyman, R., Synthesis of Thiol-Derivatised Gold Nanoparticles in a Two-Phase Liquid–Liquid System. *J. Chem. Soc., Chem. Commun.* **1994,** *0* (7), 801-802.

6. Lohse, S. E.; Murphy, C. J., Applications of Colloidal Inorganic Nanoparticles: From Medicine to Energy. *J. Am. Chem. Soc.* **2012,** *134* (38), 15607-15620.

7. Murray, C. B.; Norris, D. J.; Bawendi, M. G., Synthesis and Characterization of Nearly Monodisperse CdE (E = Sulfur, Selenium, Tellurium) Semiconductor Nanocrystallites. *J. Am. Chem. Soc.* **2002,** *115* (19), 8706-8715.

8. Stöber, W.; Fink, A.; Bohn, E., Controlled Growth of Monodisperse Silica Spheres in the Micron Size Range. *J. Colloid Interface Sci.* **1968,** *26* (1), 62-69.

9. Dong, A.; Chen, J.; Vora, P. M.; Kikkawa, J. M.; Murray, C. B., Binary Nanocrystal Superlattice Membranes Self-Assembled at the Liquid–Air Interface. *Nature* **2010,** *466* (7305), 474-477.

10. Wei, J.; Schaeffer, N.; Pileni, M.-P., Ligand Exchange Governs the Crystal Structures in Binary Nanocrystal Superlattices. *J. Am. Chem. Soc.* **2015,** *137* (46), 14773-14784.

11. Wen, T.; Majetich, S. A., Ultra-Large-Area Self-Assembled Monolayers of Nanoparticles. *ACS Nano* **2011,** *5* (11), 8868-8876.

12. Wang, D.; Dasgupta, T.; van der Wee, E. B.; Zanaga, D.; Altantzis, T.; Wu, Y.; Coli, G. M.; Murray, C. B.; Bals, S.; Dijkstra, M.; van Blaaderen, A., Binary Icosahedral Clusters of Hard Spheres in Spherical Confinement. *Nat. Phys.* **2020,** *17* (1), 128-134.

13. Xie, Y.; Vincent, A. H.; Chang, H.; Rinehart, J. D., Strengthening Nanocomposite Magnetism through Microemulsion Synthesis. *Nano Res.* **2018,** *11* (8), 4133-4141.

14. Yang, Y.; Wang, B.; Shen, X.; Yao, L.; Wang, L.; Chen, X.; Xie, S.; Li, T.; Hu, J.; Yang, D.; Dong, A., Scalable Assembly of Crystalline Binary Nanocrystal Superparticles and Their Enhanced Magnetic and Electrochemical Properties. *J. Am. Chem. Soc.* **2018,** *140* (44), 15038-15047.

15. Santos, P. J.; Cao, Z.; Zhang, J.; Alexander-Katz, A.; Macfarlane, R. J., Dictating Nanoparticle Assembly via Systems-Level Control of Molecular Multivalency. *J. Am. Chem. Soc.* **2019,** *141* (37), 14624-14632.

16. Nayak, L.; Mohanty, S.; Nayak, S. K.; Ramadoss, A., A Review on Inkjet Printing of Nanoparticle Inks for Flexible Electronics. *J. Mater. Chem. C* **2019,** *7* (29), 8771-8795.

17. Choi, J.-H.; Wang, H.; Oh, S. J.; Paik, T.; Sung, P.; Sung, J.; Ye, X.; Zhao, T.; Diroll, B. T.; Murray, C. B.; Kagan, C. R., Exploiting the Colloidal Nanocrystal Library to Construct Electronic Devices. *Science* **2016,** *352* (6282), 205-208.

18. Han, D.; Guo, G.; Yan, Y.; Li, T.; Wang, B.; Dong, A., Pomegranate-Like, Carbon-Coated $Fe_3O_4$ Nanoparticle Superparticles for High-Performance Lithium Storage. *Energy Storage Mater.* **2018,** *10*, 32-39.

19. Lan, X.; Chen, M.; Hudson, M. H.; Kamysbayev, V.; Wang, Y.; Guyot-Sionnest, P.; Talapin, D. V., Quantum Dot Solids Showing State-Resolved Band-Like Transport. *Nat. Mater.* **2020,** *19* (3), 323-329.

20. Coey, J. M. D., Magnetism and Magnetic Materials. Cambridge University Press: Cambridge, 2010; p 266.

21. Chappert, C.; Fert, A.; Van Dau, F. N., The Emergence of Spin Electronics in Data Storage. *Nat. Mater.* **2007,** *6* (11), 813-823.

22. Ikeda, S.; Hayakawa, J.; Lee, Y. M.; Matsukura, F.; Ohno, Y.; Hanyu, T.; Ohno, H., Magnetic Tunnel Junctions for Spintronic Memories and Beyond. *IEEE Trans. Electron Devices* **2007,** *54* (5), 991-1002.

23. Tsymbal, E. Y.; Pettifor, D. G., Perspectives of Giant Magnetoresistance. *Solid State Phys.* **2001**. *56*. 113-237.

24. Baibich, M. N.; Broto, J. M.; Fert, A.; Vandau, F. N.; Petroff, F.; Eitenne, P.; Creuzet, G.; Friederich, A.; Chazelas, J., Giant Magnetoresistance of (001)Fe/(001) Cr Magnetic Superlattices. *Phys. Rev. Lett.* **1988,** *61* (21), 2472-2475.

25. Binasch, G.; Grunberg, P.; Saurenbach, F.; Zinn, W., Enhanced Magnetoresistance in Layered Magnetic-Structures with Antiferromagnetic Interlayer Exchange. *Phys. Rev. B* **1989,** *39* (7), 4828-4830.

26. Berkowitz, A. E.; Mitchell, J. R.; Carey, M. J.; Young, A. P.; Zhang, S.; Spada, F. E.; Parker, F. T.; Hutten, A.; Thomas, G., Giant Magnetoresistance in Heterogeneous Cu-Co Alloys. *Phys. Rev. Lett.* **1992,** *68* (25), 3745-3748.

27. Xiao, J. Q.; Jiang, J. S.; Chien, C. L., Giant Magnetoresistance in Nonmultilayer Magnetic Systems. *Phys. Rev. Lett.* **1992,** *68* (25), 3749-3752.

28. Fujimori, H.; Mitani, S.; Ohnuma, S., Tunnel-Type GMR in Co-Al-O Insulated Granular System — Its Oxygen-Concentration Dependence. *J. Magn. Magn. Mater.* **1996,** *156* (1-3), 311-314.

29. Wang, T.; Luan, Z. Z.; Ge, J. Y.; Liu, L.; Wu, D.; Lv, Z. P.; Zuo, J. L.; Sun, S. H., Enhancing Low-Field Magnetoresistance in Magnetite Nanoparticles via Zinc Substitution. *Phys. Chem. Chem. Phys.* **2018,** *20* (25), 17245-17252.

30. Lv, Z. P.; Luan, Z. Z.; Cai, P. Y.; Wang, T.; Li, C. H.; Wu, D.; Zuo, J. L.; Sun, S. H., Enhancing Magnetoresistance in Tetrathiafulvalene Carboxylate Modified Iron Oxide Nanoparticle Assemblies. *Nanoscale* **2016,** *8* (24), 12128-12133.

31. Kohiki, S.; Kinoshita, T.; Nara, K.; Akiyama-Hasegawa, K.; Mitome, M., Large, Negative Magnetoresistance in an Oleic Acid-Coated $Fe_3O_4$ Nanocrystal Self-Assembled Film. *ACS Appl. Mater. Interfaces* **2013,** *5* (22), 11584-11589.

32. Chen, J.; Ye, X.; Oh, S. J.; Kikkawa, J. M.; Kagan, C. R.; Murray, C. B., Bistable Magnetoresistance Switching in Exchange-Coupled $CoFe_2O_4$-$Fe_3O_4$ Binary Nanocrystal Superlattices by Self-Assembly and Thermal Annealing. *ACS Nano* **2013,** *7* (2), 1478-86.

33. Anil Kumar, P.; Ray, S.; Chakraverty, S.; Sarma, D. D., Engineered Spin-Valve Type Magnetoresistance in $Fe_3O_4$-$CoFe_2O_4$ Core-Shell Nanoparticles. *Appl. Phys. Lett.* **2013,** *103* (10), 102406.

# Chapter 2

# Colloidal Synthesis of Nanoparticles with Targeted Magnetic Properties

## 2.1 Introduction

The many methods to produce colloidal inorganic nanoparticles include co-precipitation,[1-2] sol-gel,[3-4] hydrothermal,[5] and micelle-templated[6-7] syntheses. Among these other methods, high temperature thermal decomposition in organic solvents is notable for its ability to produce nanoparticles of high crystallinity and monodispersity. The necessary reactants of these syntheses are metal-organic compounds, which are the precursors to the inorganic nanoparticle cores, and surfactant molecules, which help to direct the growth of the nanoparticles during synthesis and act as stabilizing surface ligands in the end product. The basis for the production of monodisperse nanoparticles with this method is typically understood through the LaMer model of 'burst' nucleation followed by particle growth.[8] In an ideal synthesis (Figure 2.1a), the metal-organic precursors decompose and produce increasingly supersaturated concentrations of monomer (an intermediate species which coalesces to form the crystalline inorganic core of the nanoparticle). At a high enough concentration, $C_N$, the monomers nucleate homogeneously. With a sufficiently high nucleation rate, the reaction mixture is depleted of monomers and no further nucleation takes place; these are the conditions for 'burst' nucleation. A growth stage follows the 'burst'

nucleation, wherein the remaining monomers add to the existing nuclei. Because the nuclei are all formed at once, they undergo similar growth stages and finish the reaction at similar sizes. On the other hand, if the initial nucleation event does not sufficiently deplete the reaction mixture of monomers to below $C_N$, or if multiple nucleation events occur (Figure 2.1b), multiple sets of nuclei undergo different amounts of growth, resulting in a polydisperse product.

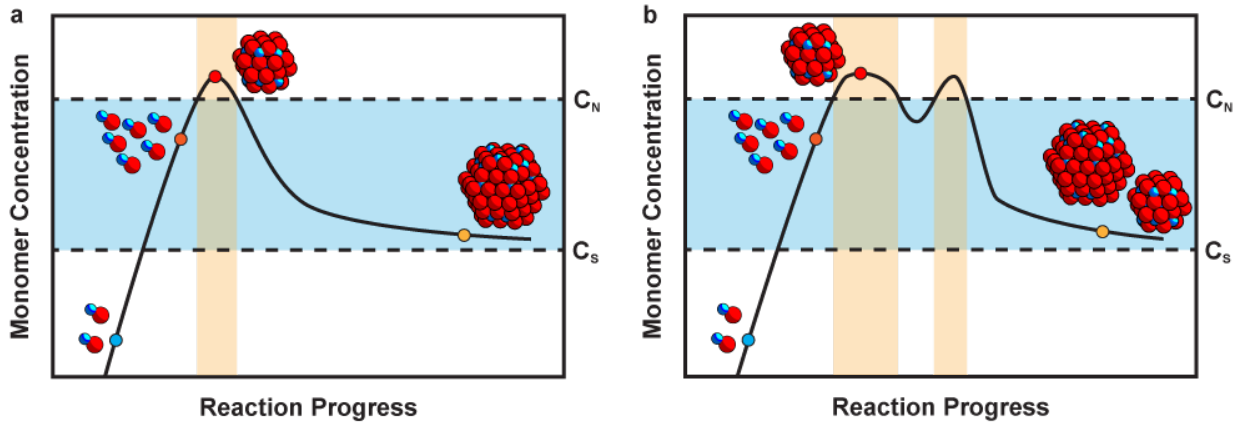


**Figure 2.1.** Depiction of monomer concentration vs reaction progress in a) an ideal LaMer synthesis, resulting in a monodisperse nanoparticle product and b) a synthesis lacking a distinct nucleation event, resulting in a polydisperse nanoparticle product.

Although there is a vast chemical parameter space of metal-organic precursors, surfactants, and solvents with which to optimize nanoparticle syntheses, the design of a synthesis of monodisperse nanoparticles must ultimately satisfy the requirement of separation of the nucleation and growth processes. Fulfillment of this condition is often related to reaction conditions rather than the intricacies of chemical bonding. Differences in reaction conditions may also be responsible for the common occurrence of nominally equivalent syntheses producing nanoparticles with different sizes and dispersities. To this end, in the following section I present synthetic techniques which facilitate consistent formation of monodisperse nanoparticles in nanoparticle syntheses which cover a variety of the chemical parameter space.

## 2.2 General Synthetic Techniques to Produce Monodisperse Nanoparticles

### 2.2.1 Improving Nanoparticle Morphology

The challenge which prompted development of new synthetic techniques was a synthesis of iron oxide nanocubes from iron(III) oleate with sodium oleate as a surfactant.[9] This synthesis of iron oxide nanocubes can be seen as a modification of the synthesis of spherical iron oxide nanoparticles from iron(III) oleate and oleic acid as surfactant, first reported by Hyeon and coworkers.[10] Using the standard Schlenk technique depicted in Figure 2.2a, monodisperse, spherical nanoparticles were easily made. However, upon trying to reproduce the nanocube synthesis from Heiss and coworkers with standard Schlenk technique, no nanoparticles were obtained, indicating a suppression of nucleation by the addition of sodium oleate. A solution to this failed synthesis was found from the work of Cao and coworkers, who discovered the importance of bubbling to promote 'burst' nucleation and ultimately the formation of monodisperse nanoparticles.[11] Bubbling enables large amounts of heat transfer which promotes both the endothermic and exothermic chemical reactions involved in thermal decomposition of precursors and formation of the nanoparticles' crystal lattices. In a typical solvothermal nanoparticle synthesis, this bubbling is achieved by

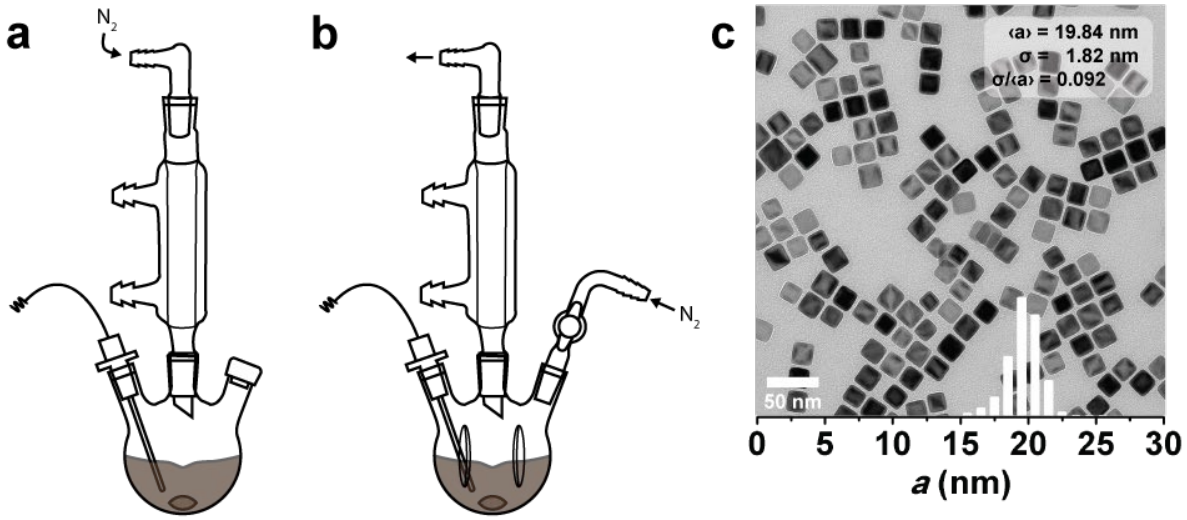


**Figure 2.2.** Drawings of the glassware used for nanoparticle synthesis using a) standard Schlenk technique and b) a modified setup with a flowing atmosphere and Morton flask. c) Transmission electron micrograph of iron oxide nanocubes resulting from synthesis using the modified setup in b).

vigorous boiling of the solvent at reflux; Cao and coworkers showed that bubbling produced by reducing the pressure in the reaction system or by a needle flowing inert gas through the reaction mixture was equally effective. The combination of a slight overpressure of $N_2$ gas in the standard Schlenk setup and the nucleation suppressing effect of sodium oleate prevented the iron oxide nanocubes from nucleating. By switching the inert gas supply in the reaction setup to a needle flowing $N_2$ through the reaction mixture, nanocubes were successfully obtained. With further experimentation, the setup in Figure 2.2b was developed, producing the monodisperse nanocubes in Figure 2.2c. With a flowing atmosphere rather than a static inert gas blanket and a Morton flask, which introduces turbulence to the stirring of the reaction mixture, the modified setup consistently produces vigorous bubbling at reflux.

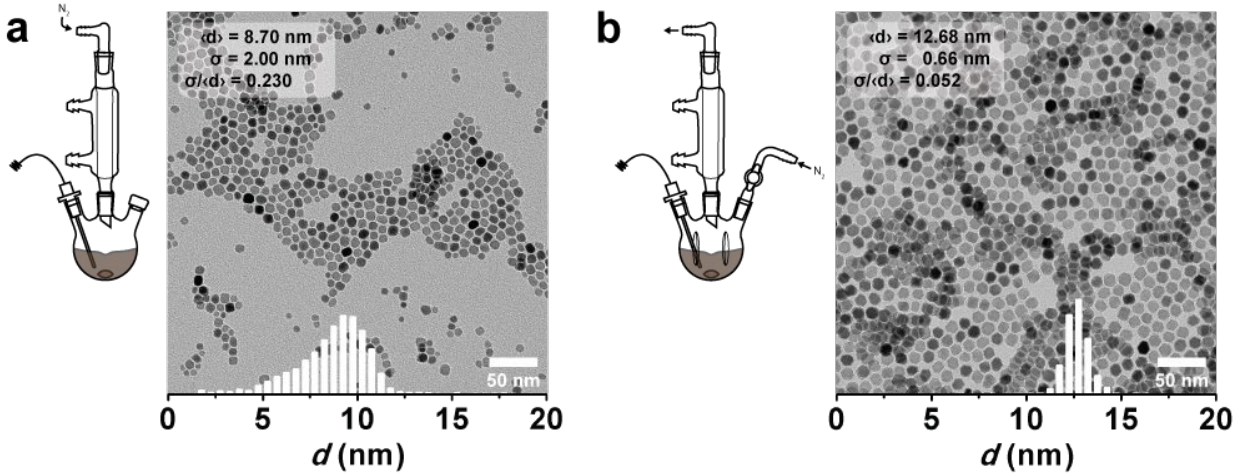


**Figure 2.3.** Transmission electron micrographs of $Fe_3O_4$ nanoparticles produced from $Fe(acac)_3$ using a) standard Schlenk technique and b) the modified setup.

The modified setup has proven able to improve the monodispersity of nanoparticles from other syntheses as well. Another popular synthesis of iron oxide nanoparticles involves the decomposition of iron(III) acetylacetonate, $Fe(acac)_3$, in the presence of oleic acid and oleylamine surfactants. Under a blanket of inert gas, refluxing acetone produced by the decomposition of acetylacetonate bumps violently and causes large temperature and pressure fluctuations.[12] In certain cases, the bumping can even dislodge glassware at their ground glass joints, posing a safety hazard and ruining the reaction. Using the modified setup, the flowing $N_2$ carries the acetone and other volatile byproducts out of the reaction system, allowing

more precise control of the reaction temperature. The improvement in reaction conditions is evident in the dispersity and morphology of the respective nanoparticles, shown in Figure 2.3. The nanoparticles made using standard Schlenk technique do not have a uniform shape and have a large size distribution (measured by the coefficient of variation, CV = $\sigma/\langle d \rangle$, where $\sigma$ and $\langle d \rangle$ are the standard deviation and average of the nanoparticle diameters, respectively). On the other hand, the nanoparticles produced using the modified setup all have the same truncated octahedral shape, with a vastly improved CV = 0.052.

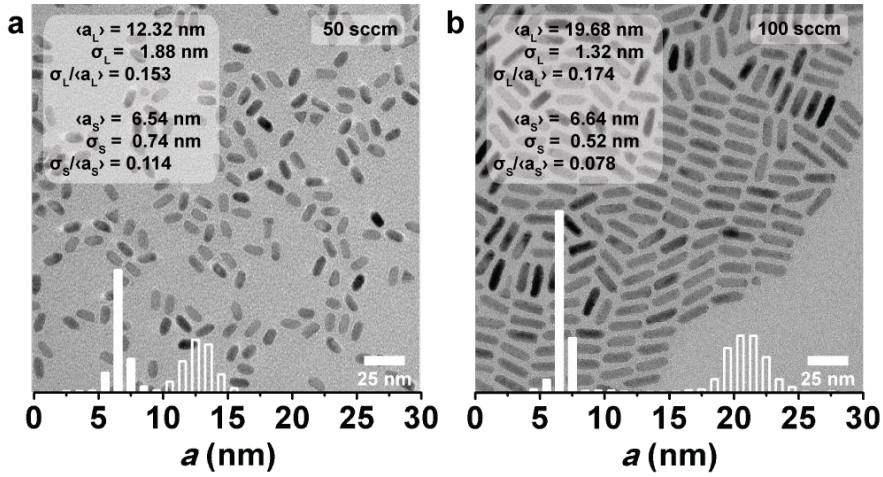


**Figure 2.4.** Transmission electron micrographs of *wz*-CoO nanorods synthesized with $N_2$ flow rates of a) 50 sccm and b) 100 sccm.

Another synthesis which is improved using the modified setup is the synthesis of *wz*-CoO nanorods from the decomposition of cobalt(II) oleate. First reported by Hyeon and coworkers,[13] this synthesis was investigated in further detail by Schaak and coworkers, who found issues which prevented consistent production of *wz*-CoO nanoparticles.[14] Firstly, synthesis of the cobalt(II) oleate precursor sometimes resulted in an additional white precipitate. Removal of this impurity prevented the decomposition of the cobalt(II) oleate to form nanoparticles, even at reflux temperatures up to 320°C. Reaction of the 'crude' cobalt(II) oleate from which the impurity had not been removed would only sometimes result in a nanoparticle product. To reliably decompose the cobalt(II) oleate and produce nanoparticles, Schaak and coworkers had to add basic additives to the synthesis, which produced either cone-shaped or golf tee-shaped nanoparticles rather than the pencil-shaped nanorods first reported by Hyeon and coworkers. Alternatively,

an extra step of purging the reaction system with flowing Ar gas for 2 h at 240°C could be performed to produce bullet-shaped nanoparticles. In our first attempts to synthesize cobalt(II) oleate, we indeed observed the formation of a white precipitate. However, when the reaction system was first nominally purged of air by flowing $N_2$ over the top of the condenser attached to the reaction flask, and the reaction was then performed under an inert $N_2$ blanket, cobalt(II) oleate was consistently formed without any additional byproducts. Thermal decomposition of this cobalt(II) oleate in the modified setup reliably resulted in pencil-shaped nanorods with only a single heating step. An additional 2 h purge step was unnecessary as $N_2$ was flowed through the reaction system for the duration of the synthesis. Besides allowing for a shorter, simpler synthesis, the modified setup also provided another lever of control through the flow rate of $N_2$. Figure 2.4 shows TEM images of *wz*-CoO nanorods synthesized with $N_2$ flow rates of 50 and 100 sccm, resulting in nanorods of similar widths, but lengths of 12.32 nm and 19.68 nm respectively.

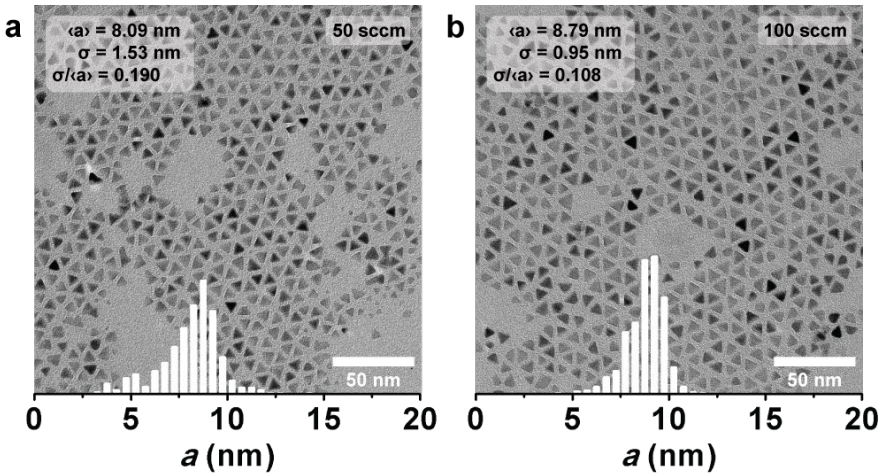


**Figure 2.5.** Transmission electron micrograph of *rs*-CoO nanoparticles synthesized with a) 50 sccm and b) 100 sccm of $N_2$.

Zhong and coworkers reported that decomposing cobalt(II) oleate in the presence of the fatty alcohol 1-dodecanol resulted in the formation of *rs*-CoO nanoparticles of varying morphologies. When about 20 equivalents of 1-dodecanol (to cobalt(II) oleate) was used, roughly tetrahedral nanoparticles were formed.[15] With slight modifications (10 equivalents of oleyl alcohol replacing the 1-dodecanol) and using the modified setup, tetrahedral nanoparticles of more uniform shape were obtained. Furthermore,

controlling the flow rate of $N_2$ through the reaction system as shown in Figure 2.5, where the CV of the nanoparticles was nearly halved by increasing the $N_2$ flow rate from 50 to 100 sccm.

### 2.2.2 Controlling Structural and Chemical Composition

In addition to improving nanoparticle morphology and adding flow rate as a degree of synthetic control, the modified setup also allows for the safe use of non-inert gases during synthesis. In this work, only $O_2$ has been added to the reaction atmosphere, but other gases like $H_2$ could also be used safely. Several observations inspired the addition of $O_2$ to our synthesis of iron oxide nanoparticles. Firstly, as Rinaldi and coworkers noted, solvothermal synthesis of iron oxide from iron oleate is performed under inert conditions, leaving the question of "in the absence of oxygen, how can metal oxide nanoparticles be formed successfully and reproducibly?"[16] Secondly, while many reports on synthesis using iron oleate claim the direct formation of magnetite ($Fe_3O_4$) or maghemite ($Fe_2O_3$) (two related forms of spinel iron oxide which are difficult to distinguish from each other) our experiments consistently produced nanoparticles with a wüstite (*rs*-FeO) core and an oxidized spinel iron oxide shell when performed without addition of $O_2$. The presence of the *rs*-FeO core can be seen by transmission electron microscopy (TEM, Figure 2.6a) and by

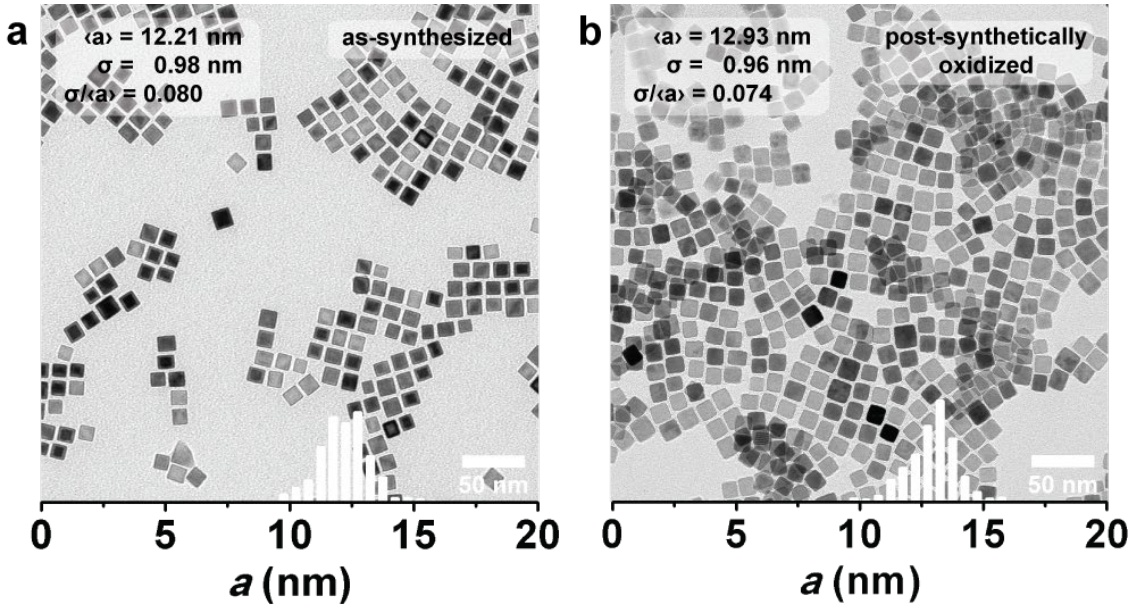


**Figure 2.6.** Transmission electron micrographs of iron oxide nanocubes a) directly out of synthesis, showing a core/shell structure, and b) after post-synthetic oxidation, showing a homogeneous phase throughout each nanoparticle.

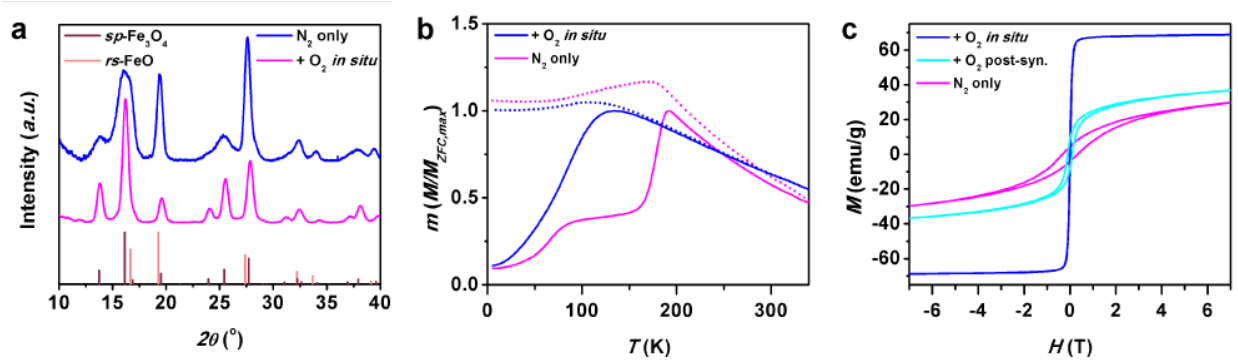


**Figure 2.7.** a) X-ray diffraction patterns collected with Mo Kα radiation, b) normalized magnetization vs temperature, and c) magnetization vs field measured at 5 K, of iron oxide nanoparticles synthesized under inert conditions and with the addition of $O_2$. The curves in b) are measured after cooling to 5 K without an applied field (ZFC, solid lines) and after cooling under a field of 100 Oe (FC, dotted lines), and are normalized to the maximum ZFC magnetization.

x-ray diffraction (XRD, blue line in Figure 2.7a). It is also evident from the precipitous drop in the zero-field-cooled (ZFC) magnetization of the nanoparticles (solid magenta line, Figure 2.7b) at its Néel temperature ($T_{N,\ rs\text{-}FeO}$ = 198 K). Nanoparticles synthesized with an inert atmosphere had to be annealed at 100°C in air for 12 h to oxidize the wüstite to spinel iron oxide (Figure 2.6b). However, this low temperature oxidation process is imprecise and can leave antiphase boundary defects in the nanoparticles' crystal lattices.[17] Even when XRD and TEM show no obvious secondary phases or defect structures, the magnetization of post-synthetically oxidized nanoparticles can be diminished from and the coercivity greater than expected for highly crystalline spinel iron oxide (Figure 2.7c).

Rinaldi and coworkers demonstrated that adding $O_2$ to the reaction atmosphere at reflux could oxidize the iron oxide nanoparticles *in situ* to the spinel phase. The *in-situ* oxidation at the high reflux temperature produced single-crystalline nanoparticles that were free of antiphase boundaries. We found the same result when adding $O_2$ during reflux, with resulting nanoparticles showing only peaks corresponding to spinel iron oxide in their XRD patterns (Figure 2.7a), lacking a peak at the Néel temperature in their ZFC magnetization (Figure 2.7b), and having a high saturation magnetization and no coercivity (Figure 2.7c). In our experiments, we further showed that higher concentrations of $O_2$ could produce pure magnetite nanoparticles. Nanoparticles synthesized with 8.5% $O_2$ displayed a sharp corner in their ZFC magnetization just above 100 K (Figure 2.8f), an indication of the Verwey transition. This metal-insulator transition only

presents itself in magnetite and is very sensitive to the stress state and stoichiometry of the crystal lattice. Although nanoparticles synthesized with smaller amounts of oxygen still displayed the large saturation magnetization and minimal coercivity of spinel iron oxide, they showed no evidence of the Verwey transition Figure 2.8d,e.

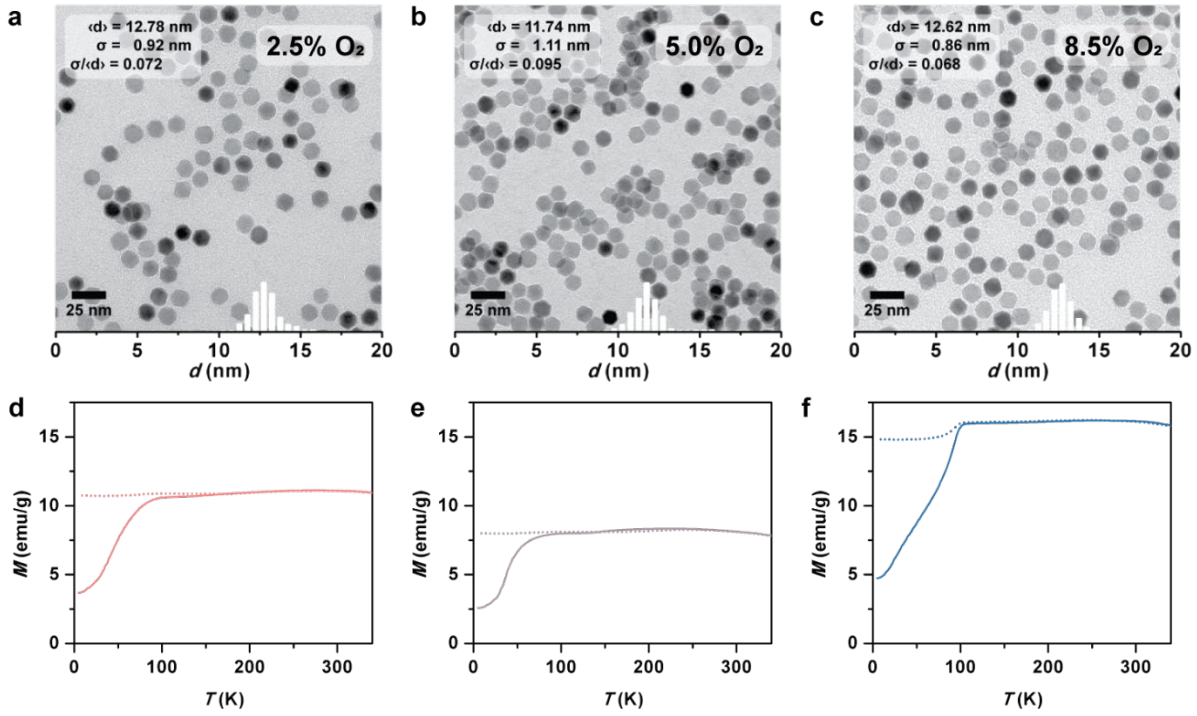


**Figure 2.8.** a-c) Transmission electron micrographs and d-f) plots of ZFC (solid lines) and FC (dotted lines) magnetization vs temperature measured at 100 Oe of iron oxide nanoparticles synthesized with 2.5%, 5%, and 8.5% $O_2$, respectively.

## 2.3 Heterostructured Nanoparticles with Extrinsic Magnetic Anisotropy

The development of nanoparticles with higher coercivity and remanent magnetization is crucial for their application in spintronic devices, as will be further discussed in Chapter 4. The crucial parameter which can supply these properties is the magnetocrystalline anisotropy of the nanoparticles. Nanoparticles of materials with greater intrinsic anisotropy can be synthesized – notably $CoFe_2O_4$, or cobalt-substituted magnetite, has roughly 20 times more anisotropy than magnetite and can be synthesized with the same methods and in the same nanoparticle forms. Other material phases with even greater anisotropy (e.g. $L1_0$

FePt or $SmCo_5$) are difficult to directly produce in stable, colloidal forms.[18-20] An alternative to the intrinsic magnetocrystalline anisotropy of the material is to add extrinsic anisotropy. Two notable sources of extrinsic anisotropy are shape anisotropy and exchange bias. Three dimensional surfaces depicting the energy associated with each orientation of the magnetic moment are shown for an isotropic $Fe_3O_4$ nanoparticle (Figure 2.9a) and an $Fe_3O_4$ nanorod with a length twice its diameter (Figure 2.9b). The magnetic anisotropy associated with the nanorod's shape is nearly 3 times its magnetocrystalline anisotropy. However, while shape anisotropy could serve as a strong source of magnetic anisotropy, many common magnetic materials like the ferrites have cubic crystal structures and are difficult to synthesize as anisotropic nanoparticles. A more accessible form of extrinsic anisotropy in nanoparticles comes from exchange bias. Exchange bias results from the interfacing of a permanent magnet with an antiferromagnet, and has been well developed in both thin film multilayers[21-22] and heterostructured nanoparticles.[23-25] Exchange coupling at the interface causes the permanent magnet's atomic spins to align themselves with the direction of the interfacial atomic spins of the antiferromagnet, leading to a shift in the hysteresis loop and increase in coercivity shown in Figure 2.10. Where a permanent magnet alone has a field-symmetric hysteresis, the exchange-biased material requires a larger magnetic field to reverse its magnetization from the direction imposed by the antiferromagnet and a lesser field to return it to alignment with the

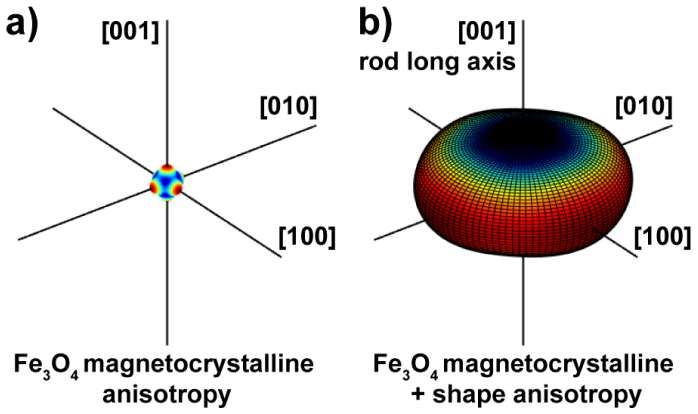


**Figure 2.9.** Energy surfaces depicting the magnetic energy of different orientations of the magnetic moment in a) isotropic and b) rod-shaped $Fe_3O_4$ nanoparticles. The nanorods have a 2:1 aspect ratio of their length to diameter.

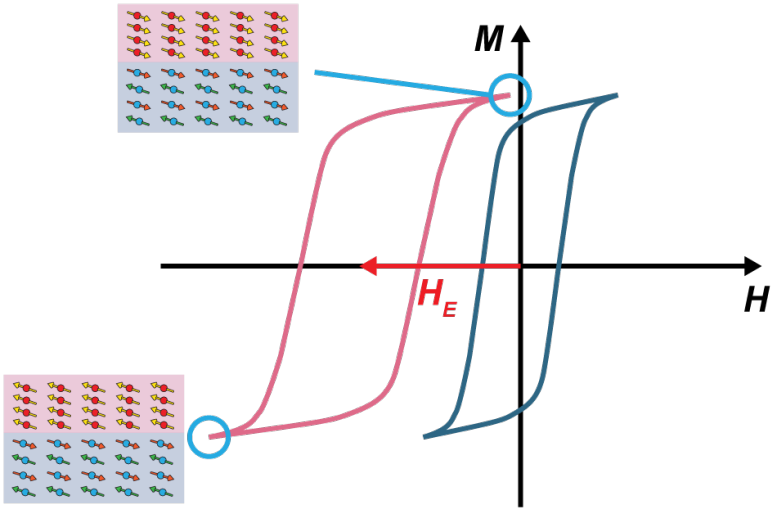


**Figure 2.10.** Diagram of how exchange bias with an antiferromagnet impacts a permanent magnet's magnetic hysteresis and spin alignment. Exchange coupling between the permanent magnet and the antiferromagnet at their interface gives an additional unidirectional anisotropy to the permanent magnet.

antiferromagnet. This shift is quantified by the exchange field, $H_E$, which is measured from the origin to the center of the shifted hysteresis loop.

### 2.3.1 Exchange Biased Core/Shell Nanoparticles

Our approach to optimizing exchange bias in nanoparticles was to first develop high quality antiferromagnetic nanoparticles, which have received less attention than ferro- or ferrimagnetic materials. Two key attributes of antiferromagnets which contribute to their performance in exchange bias are their magnetocrystalline anisotropy and their Néel temperature. Although they exhibit no net moment, antiferromagnets still have an ordered spin structure which has preferred spin orientations within their crystal structure. The strength of this anisotropy is translated to the degree of exchange bias which they can induce. The Néel temperature is the temperature beyond which an antiferromagnetic material becomes paramagnetic and therefore defines the maximum of the temperature range in which an antiferromagnet can be used for exchange bias.

Among the known antiferromagnetic materials, the rock salt structured transition metal monoxides are the most accessible in nanoparticle form. The most notable phases are *rs*-FeO, *rs*-CoO, and *rs*-NiO, which have Néel temperatures of 198, 291, and 525 K, respectively. From their Néel temperatures alone, it would appear that *rs*-NiO is the most desirable phase for exchange bias, but *rs*-CoO has a considerably higher anisotropy than *rs*-NiO.[26] Conveniently, the antiferromagnetic properties of these material phases can be tuned by doping the phases together and controlling the metal composition in the rock salt lattice.[26-28]

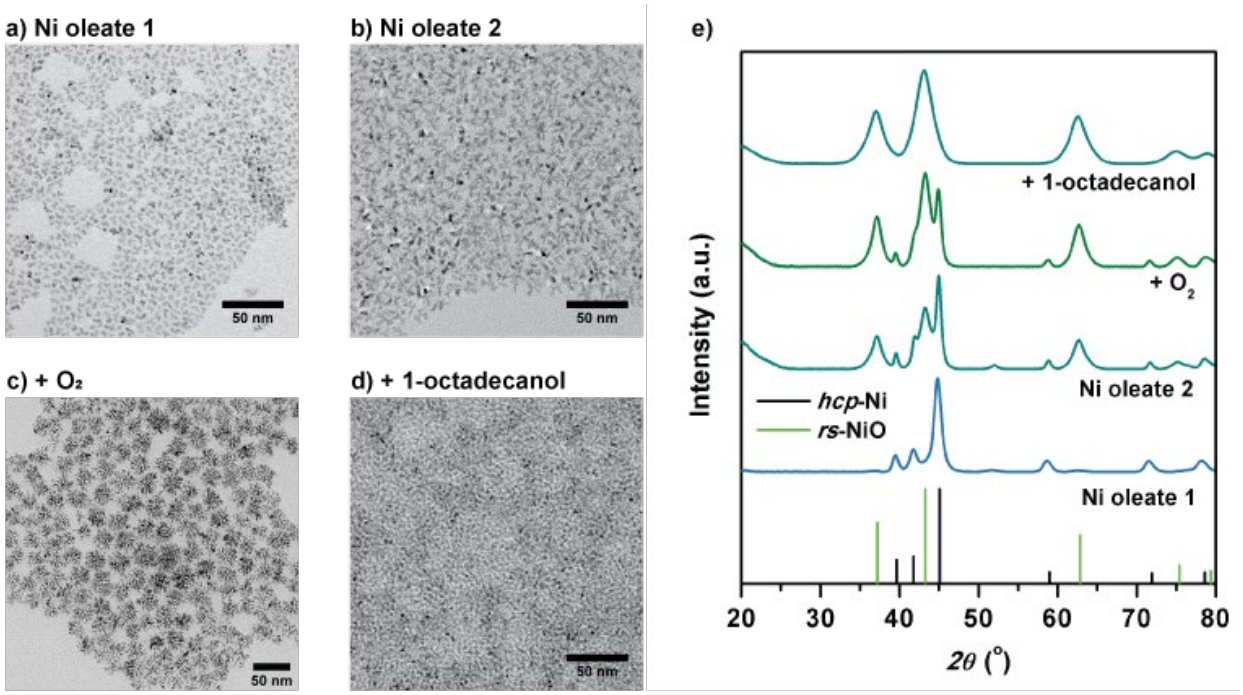


**Figure 2.11.** Transmission electron micrographs of Ni based nanoparticles synthesized by thermal decomposition of a) aged nickel(II) oleate, b) fresh nickel(II) oleate, c) nickel(II) oleate in the presence of $O_2$, and d) nickel(II) oleate in the presence of 1-octadecanol. e) X-ray diffraction patterns corresponding to the same batches of nanoparticles.

With high-quality *rs*-CoO nanoparticles already synthesized (Figure 2.5), we turned our efforts to synthesizing *rs*-NiO nanoparticles through similar methods. However, thermal decomposition of nickel(II) oleate failed to produce *rs*-NiO nanoparticles with a well-defined shape, and often produced clusters of small (<2 nm) particles and metallic *hcp*-Ni instead (Figure 2.11). Buriak and coworkers showed that combining nickel(II) oleate with iron(III) oleate could produce well-defined $Ni_xFe_{1-x}O$ nanoparticles with the rock-salt phase.[29] In our experiments, we indeed found that decomposing a 1:1 mixed nickel(II)/iron(III)

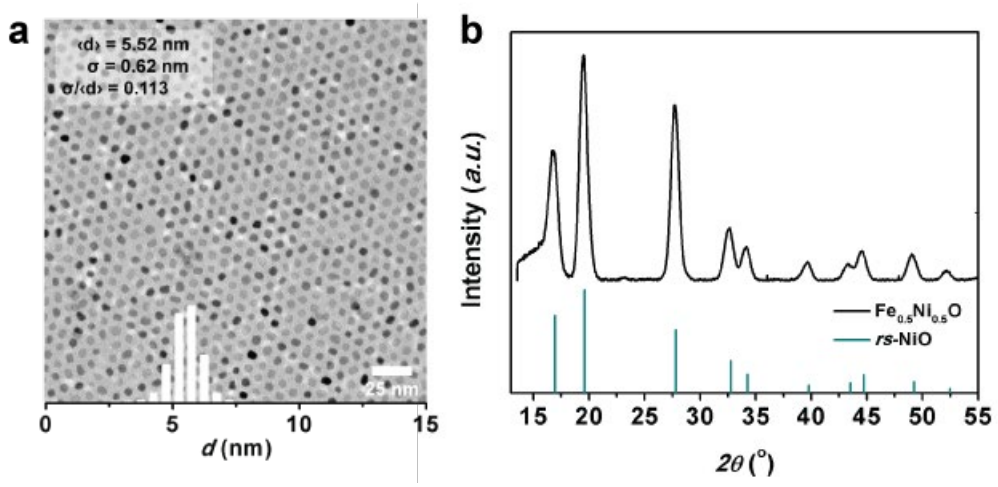


**Figure 2.12.** a) Transmission electron micrograph and b) x-ray diffraction pattern of $Ni_xFe_{1-x}O$ nanoparticles synthesized from a mixed nickel(II)/iron(III) oleate.

oleate in the presence of oleic acid produced nearly spherical nanoparticles with the rock salt structure (Figure 2.12). Inductively coupled plasma mass spectrometry indicated that the nanoparticles had a 1:1.3 ratio of nickel to iron. While we hoped that a similar strategy could be used to synthesize *rs*-$Co_xNi_{1-x}O$, all attempts resulted in misshapen, polypodal nanoparticles, though in the rock salt structure. An alternative approach requiring further investigation might be to first synthesize metallic Ni or $Co_xNi_{1-x}$ nanoparticles, then oxidize them to their rock salt oxides.[30-31]

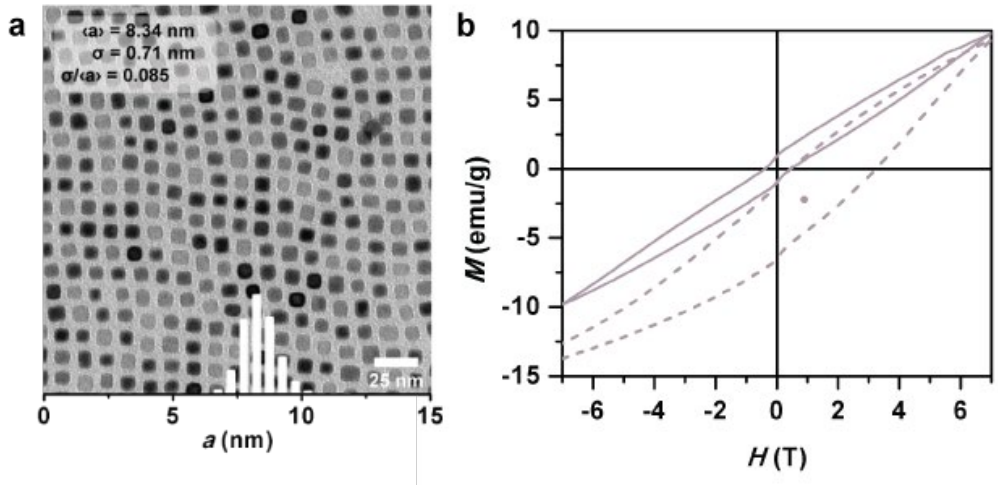


**Figure 2.13.** a) Transmission electron micrograph of $Ni_xFe_{1-x}O@CoFe_2O_4$ core/shell nanoparticles and b) a plot of their magnetization vs field at 5 K after cooling under zero field (solid line) and under a –7 T field (dashed line). The dot indicates the central point in the hysteresis of the field cooled magnetization.

Exchange-biased core/shell nanoparticles were synthesized by combining a metal oleate with antiferromagnetic nanoparticle seeds, then heating-up the mixture to decompose the metal oleate, allowing a secondary metal oxide phase to grow around the seeds. An early attempt involved the growth of $CoFe_2O_4$ on the $Ni_xFe_{1-x}O$ seeds shown in Figure 2.12a. The resulting core/shell nanoparticles are shown in Figure 2.13a; they have a diameter of 8.34 nm, indicating growth of a $CoFe_2O_4$ shell with average thickness of 1.4 nm. Their ZFC hysteresis loop in Figure 2.13b shows rather unremarkable behavior, with a small, ferromagnetic hysteresis from the $CoFe_2O_4$ shell superimposed on the dominant linear response of the antiferromagnetic core. However, after cooling under a –7 T field, the core and shell are exchange coupled leading to large exchange bias. The FC hysteresis loop shown in Figure 2.13b shows a coercivity of 1.3 T and exchange field of 0.9 T. These values greatly outstrip those of comparable *rs*-FeO@$CoFe_2O_4$ nanocubes synthesized by Heiss and coworkers, which had $H_C$ = 0.318 T and $H_E$ = 0.070 T.[32] $H_E$ was measured as the horizontal displacement of the center of the hysteresis loop, while $H_C$ was measured as half the width of the hysteresis loop at its center. The improved exchange bias provided by the $Ni_xFe_{1-x}O$ core over the *rs*-FeO core validates the concept of tuning exchange bias by modifying antiferromagnetic properties through composition. Furthermore, the true coercivity and exchange field of the material are not known, as only a

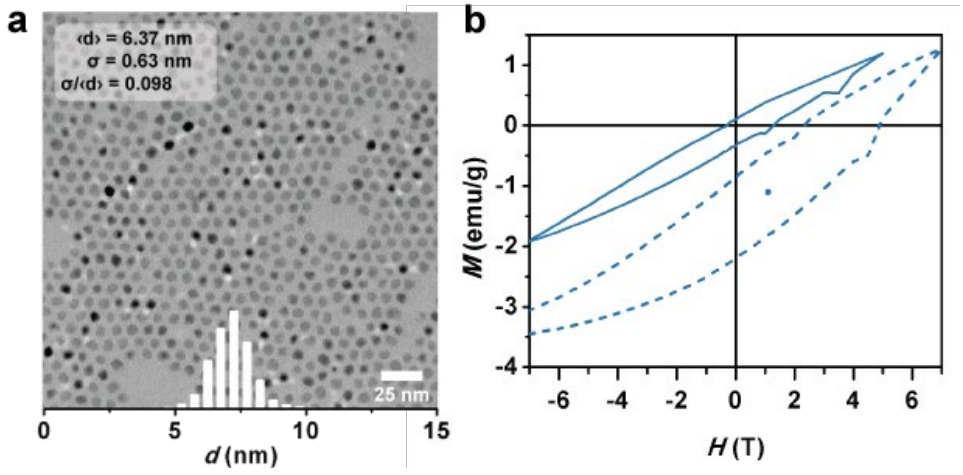


**Figure 2.14.** a) Transmission electron micrograph of *rs*-CoO@$Fe_3O_4$ core/shell nanoparticles and b) a plot of their magnetization vs field at 5 K after cooling under zero field (solid line) and under a –7 T field (dashed line). The dot indicates the central point in the hysteresis of the field cooled magnetization. The zero-field cooled hysteresis loop did not reach +7 T due to instrument error.

minor loop was measured. The lack of overlap between the forward and reverse field scans near ±7 T indicate that the material was not fully magnetically saturated; application of magnetic fields with magnitudes greater than 7 T would presumably further increase the sample's magnetization as well as the coercivity and exchange fields measured.[33]

While substituting nickel into *rs*-FeO nanoparticles improved the exchange bias of the corresponding core/shell nanoparticles, *rs*-CoO core nanoparticles could be expected to provide even greater exchange bias at low temperatures due to their large antiferromagnetic anisotropy compared to the other transition metal monoxides. Core/shell *rs*-CoO@$Fe_3O_4$ nanoparticles were synthesized by heating iron(III) oleate with oleic acid in 1-octadecene to 310ºC, then injecting a suspension of *rs*-CoO seeds in 1-octadecene and maintaining the temperature at 310ºC for 20 min, resulting in the nanoparticles shown in Figure 2.14a. The seeds were injected rather than being heated up with the other reactants in order to maintain their structure and morphology prior to iron oxide growth. The reaction mixture was also maintained at 310ºC rather than being allowed to boil in order to discourage any self-nucleation of iron oxide. The magnetic behavior of the *rs*-CoO@$Fe_3O_4$ nanoparticles was qualitatively similar to that of the $Ni_xFe_{1-x}O$@$CoFe_2O_4$ nanoparticles, but as expected had even greater $H_C$ = 1.75 T and $H_E$ = 1.10 T at 5 K (Figure 2.14b). Again, only a minor loop could be measured, meaning that the true values of $H_C$ and $H_E$ are likely even higher.

The core/shell nanoparticles discussed above have demonstrated the viability improving exchange bias in nanoparticle systems by tuning the antiferromagnetic composition. In spite of the progress shown, the application of exchange biased nanoparticles with large $H_C$ and $H_E$ at room temperature is held back by the lack of antiferromagnetic seeds which have high anisotropy and Néel temperatures. Further work in this area is needed to develop well-defined $Ni_xCo_{1-x}O$ nanoparticles which have these attributes.

### 2.3.2 Mushroom Heterostructures with Enhanced Coercivity

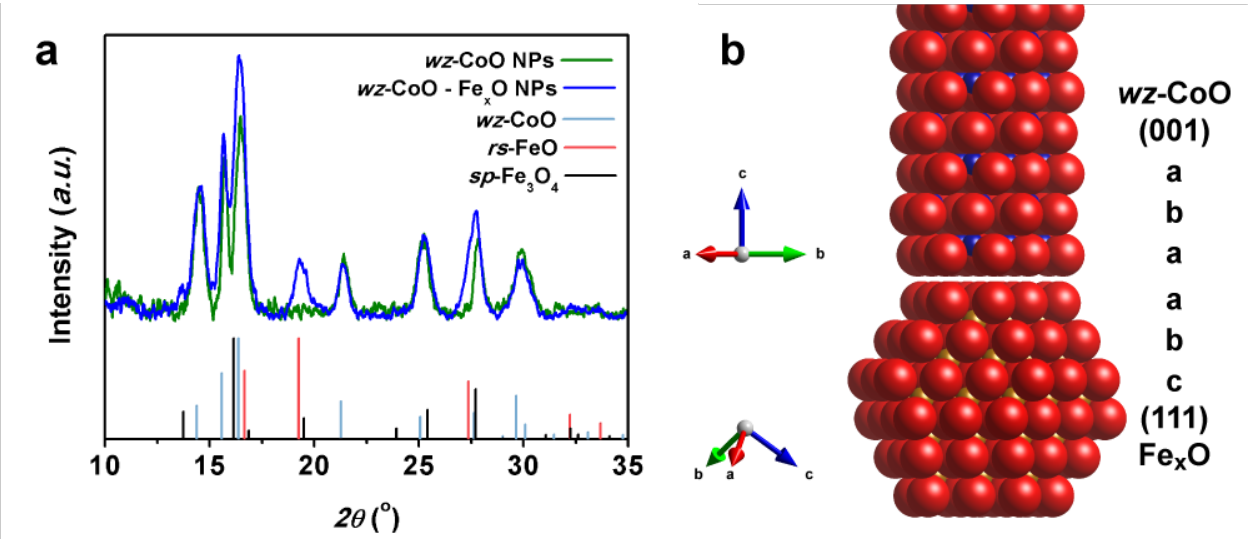


**Figure 2.15.** a) X-ray diffraction patterns of *wz*-CoO seeds and the $Fe_xO$/*wz*-CoO mushroom heterostructures grown from them. b) Depiction of the hexagonal *wz*-CoO and cubic iron oxide lattices and the equivalence of their respective close-packed (001) and (111) planes.

The successful synthesis of the *wz*-CoO nanorods in Figure 2.4 inspired us to pursue the addition of magnetic shape anisotropy to ferrite nanoparticles. While the ferrites have cubic crystal structures and are therefore difficult to synthesize in anisotropic forms, *wz*-CoO is both epitaxially compatible with other transition metal oxides and easily synthesized in anisotropic forms. Initially, attempts were made to use cation exchange to dope iron into the *wz*-CoO nanorods to form $CoFe_2O_4$ nanorods. However, these attempts were unsuccessful due to the instability of the *wz*-CoO, a metastable phase of CoO. Subsequently, seed mediated growth was used to coat the *wz*-CoO nanorods with an iron oxide shell instead. However, rather than form a continuous shell around the nanorods, iron oxide nanoparticles nucleated at one end of the nanorods, forming the mushroom heterostructure depicted in Figure 2.15b. These mushroom heterostructures were grown by injecting a suspension of *wz*-CoO seeds in 1-octadecene into a 310°C mixture of iron(II) oleate, oleic acid, and 1-octadecene. The seeds were injected rather than included in the initial reaction mixture to preserve their morphology throughout the synthesis; *wz*-CoO is known to be sensitive to acid.[14]

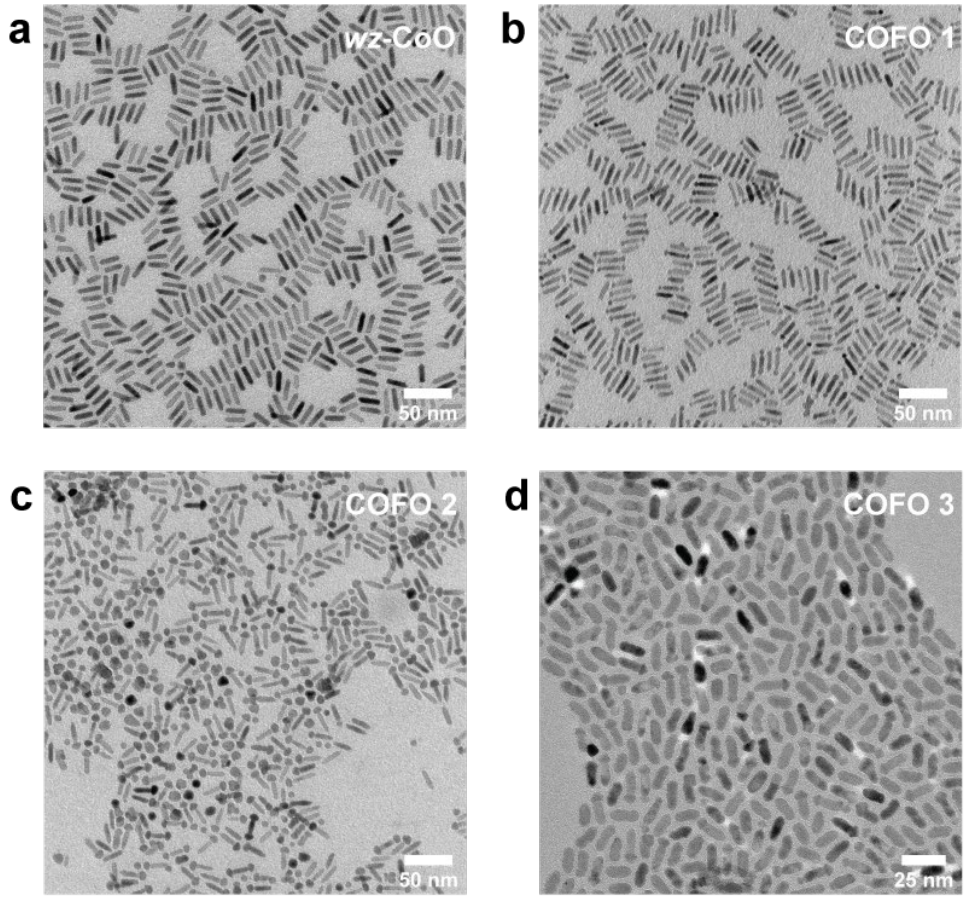


**Figure 2.16.** Transmission electron micrographs of a) *wz*-CoO seeds and b–d) *wz*-CoO/iron oxide mushroom heterostructured nanoparticles from three different syntheses.

Separate trials of similar syntheses of *wz*-CoO/iron oxide heterostructured nanoparticles resulted in a variety of morphologies of nanoparticles, a partial sample of which are shown in Figure 2.16b–d. The variability in these nanoparticles' morphologies extends to their magnetic behavior, shown in Figure 2.17. A particularly difficult trait to control is the nucleation of iron oxide onto the *wz*-CoO nanorods; in some samples, a single iron oxide particle attached to the $(00\bar{1})$ facet of the *wz*-CoO was the dominant motif (Figure 2.16d). Other samples showed a large number of *wz*-CoO nanorods with an iron oxide particle grown on each end (Figure 2.16b) while others even had three iron oxide particles grown onto one nanorod, two attached to the $(00\bar{1})$ facet and one grown on the $(001)$ tip (Figure 2.16c).

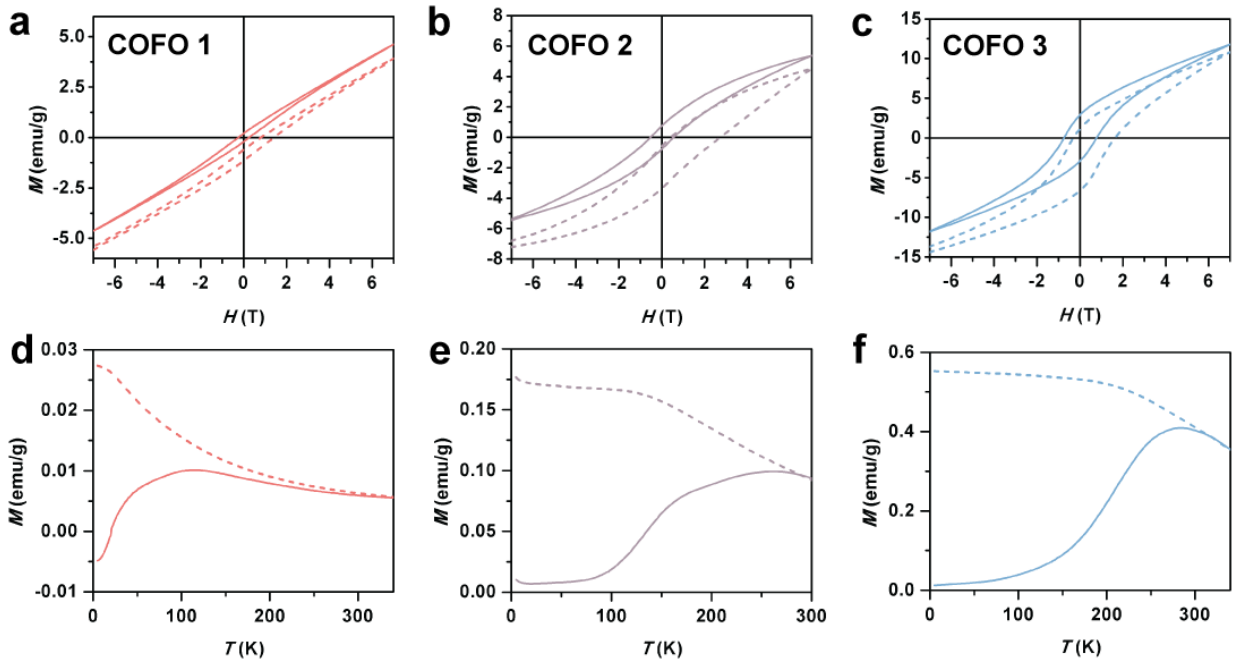


**Figure 2.17.** a–c) Plots of magnetization vs magnetic field at 5 K after cooling under zero field (solid line) and after cooling under –7 T (dashed line) and d–f) plots of magnetization vs temperature with an applied field of 100 Oe after cooling to 5 K under zero field (solid line) and under a 100 Oe field (dashed line) for *wz*-CoO/iron oxide mushroom heterostructured nanoparticles from three different syntheses.

A common theme for nanoparticles from most syntheses was an XRD pattern similar to the one shown in Figure 2.15a, with two clearly evident phases, *wz*-CoO and *rs*-FeO, and the possibility of the presence of small amounts of *sp*-$Fe_3O_4$. This phase composition is consistent with the composition of purely iron oxide nanoparticles synthesized from iron oleate, which are made of a *rs*-FeO core whose outer surface is oxidized to *sp*-$Fe_3O_4$ (Figure 2.7a). The composition of the *wz*-CoO/iron oxide heterostructured nanoparticles is intriguing because of the apparent stabilization of the *rs*-FeO from oxidation by the presence of the *wz*-CoO. One possibility is that during the synthesis, interdiffusion of cobalt and iron creates a mixed *rs*-$Co_xFe_{1-x}O$ phase which does not readily oxidize. However, more detailed TEM experiments are necessary to investigate the elemental composition of the nanoparticles.

Another commonality between many of the samples of *wz*-CoO/iron oxide heterostructured nanoparticles is the qualitative magnetic behavior depicted in Figure 2.17b,c,e,f. These nanoparticles showed both a vertical and horizontal shift in their FC hysteresis loops; both features result from exchange bias with the antiferromagnetic *wz*-CoO. Additionally, many samples had coercivities near $H_C$ = 1 T at 5

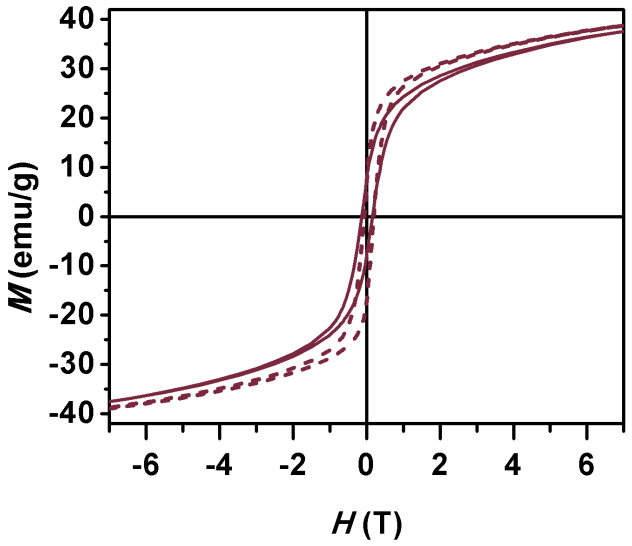


**Figure 2.18.** Magnetization vs field of *rs*-FeO@$Fe_3O_4$ core/shell nanoparticles at 5 K after cooling under zero field (solid line) and under –7 T (dashed line).

K, much greater than expected for any pure iron oxide nanoparticles. In *rs*-FeO@$Fe_3O_4$ core/shell nanoparticles of comparable size to the iron oxide particles grown on the *wz*-CoO nanorods ($d$ = 7.5 nm), only a minimal exchange bias of $H_E$ = 0.07 T was observed, compared to exchange fields $H_E$ = 0.3–0.5 T for the *wz*-CoO/iron oxide nanoparticles. The *rs*-FeO@$Fe_3O_4$ nanoparticles reached an improved coercivity of only $H_C$ = 0.13 T and showed no vertical shift in their FC hysteresis loop (Figure 2.18). The ZFC and FC magnetization vs temperature behavior in Figure 2.17f was also typical of the mushroom heterostructured nanoparticles, with a peak in ZFC magnetization very near 300 K. Their FC magnetization monotonically decreases with increasing temperature, converging with the ZFC magnetization just after it peaks. These consistent features of the ZFC and FC magnetization show that the mushroom heterostructures have high blocking temperatures and a correspondingly large magnetic anisotropy. The strong exchange bias and high blocking temperature provided by the *wz*-CoO and *rs*-FeO in the mushroom heterostructures is surprising given the *wz*-CoO is expected (though not yet fully understood) to be a weak, noncollinear antiferromagnet with a low Néel temperature near 125 K.[34-35]

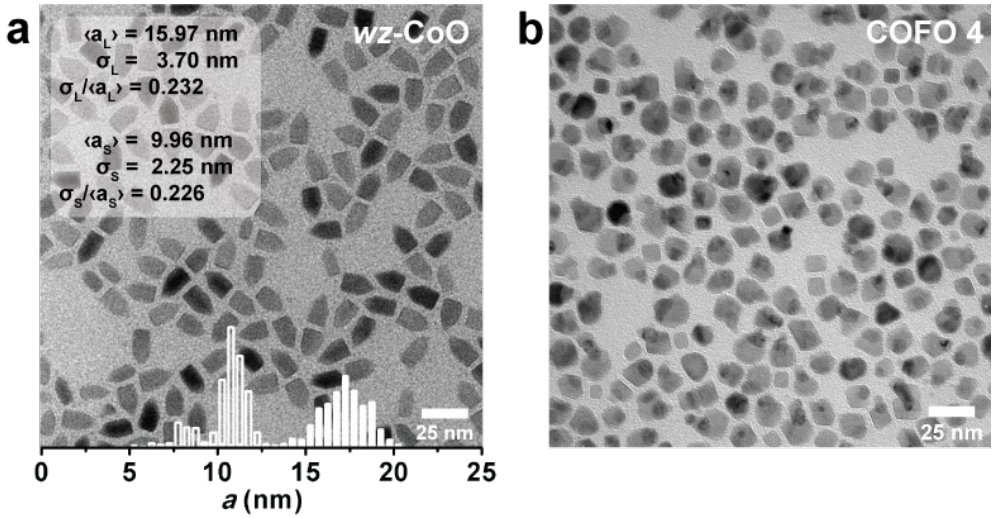


**Figure 2.19.** Transmission electron micrographs of a) wide-based *wz*-CoO nanoparticles and b) the same *wz*-CoO nanoparticles after attempted seeded growth of iron oxide.

It has proven difficult to elucidate the factors affecting exchange bias in the mushroom heterostructures. Besides a lack of synthetic control over their morphology, attempts to vary the *wz*-CoO seeds prevented the mushroom heterostructures from forming. Doubling the concentration of cobalt(II) oleate in synthesis of the *wz*-CoO produced nanorods with similar length, but greater width (Figure 2.19a). However, growth of iron oxide onto these wide-based *wz*-CoO nanorods caused them to transform. Their nanorod morphology was not evident in the product nanoparticles; while certain nanoparticles showed evidence of multiple phases, there was not a consistent heterostructured motif (Figure 2.19b). Further understanding of these unique nanoparticles will likely require more highly detailed structural analysis, *e.g.* high-resolution TEM or scanning tunneling electron microscopy with elemental mapping and Mössbauer spectroscopy. Another boon to a better understanding would be increasing yield of the mushroom heterostructures with respect to self-nucleated, spherical iron oxide nanoparticles and pristine *wz*-CoO nanorods, two byproducts which are inevitably produced in all syntheses. One step towards obtaining pure samples of mushroom heterostructures is the assembly of nanorods through depletion attraction.[36] This method allows for the separation and removal of self-nucleated, spherical iron oxide nanoparticles, producing samples for bulk study with increased purity.

## 2.4 References


1. LaGrow, A. P.; Besenhard, M. O.; Hodzic, A.; Sergides, A.; Bogart, L. K.; Gavriilidis, A.; Thanh, N. T. K., Unravelling the Growth Mechanism of the Co-Precipitation of Iron Oxide Nanoparticles with the Aid of Synchrotron X-Ray Diffraction in Solution. *Nanoscale* **2019,** *11* (14), 6620-6628.

2. Wu, J.-H.; Ko, S. P.; Liu, H.-L.; Kim, S.; Ju, J.-S.; Kim, Y. K., Sub 5 nm Magnetite Nanoparticles: Synthesis, Microstructure, and Magnetic Properties. *Mater. Lett.* **2007,** *61* (14-15), 3124-3129.

3. Dong, W.; Zhu, C., Use of Ethylene Oxide in the Sol–Gel Synthesis of α-$Fe_2O_3$ Nanoparticles from Fe(III) Salts. *J. Mater. Chem.* **2002,** *12* (6), 1676-1683.

4. Niederberger, M., Nonaqueous Sol–Gel Routes to Metal Oxide Nanoparticles. *Acc. Chem. Res.* **2007,** *40* (9), 793-800.

5. Takami, S.; Sato, T.; Mousavand, T.; Ohara, S.; Umetsu, M.; Adschiri, T., Hydrothermal Synthesis of Surface-Modified Iron Oxide Nanoparticles. *Mater. Lett.* **2007,** *61* (26), 4769-4772.

6. Carrot, G.; Valmalette, J. C.; Plummer, C. J. G.; Scholz, S. M.; Dutta, J.; Hofmann, H.; Hilborn, J. G., Gold Nanoparticle Synthesis in Graft Copolymer Micelles. *Colloid Polym. Sci.* **1998,** *276* (10), 853-859.

7. Eastoe, J.; Hollamby, M. J.; Hudson, L., Recent Advances in Nanoparticle Synthesis with Reversed Micelles. *Adv. Colloid Interface Sci.* **2006,** *128-130*, 5-15.

8. LaMer, V. K.; Dinegar, R. H., Theory, Production and Mechanism of Formation of Monodispersed Hydrosols. *J. Am. Chem. Soc.* **1950,** *72* (11), 4847-4854.

9. Kovalenko, M. V.; Bodnarchuk, M. I.; Lechner, R. T.; Hesser, G.; Schäffler, F.; Heiss, W., Fatty Acid Salts as Stabilizers in Size- and Shape-Controlled Nanocrystal Synthesis: The Case of Inverse Spinel Iron Oxide. *J. Am. Chem. Soc.* **2007,** *129* (20), 6352-6353.

10. Park, J.; An, K.; Hwang, Y.; Park, J.-G.; Noh, H.-J.; Kim, J.-Y.; Park, J.-H.; Hwang, N.-M.; Hyeon, T., Ultra-Large-Scale Syntheses of Monodisperse Nanocrystals. *Nat. Mater.* **2004,** *3* (12), 891-895.

11. Lynch, J.; Zhuang, J.; Wang, T.; LaMontagne, D.; Wu, H.; Cao, Y. C., Gas-Bubble Effects on the Formation of Colloidal Iron Oxide Nanocrystals. *J. Am. Chem. Soc.* **2011,** *133* (32), 12664-12674.

12. Hoene, J. V.; Charles, R. G.; Hickam, W. M., Thermal Decomposition of Metal Acetylacetonates: Mass Spectrometer Studies. *J. Phys. Chem.* **1958,** *62* (9), 1098-1101.

13. An, K.; Lee, N.; Park, J.; Kim, S. C.; Hwang, Y.; Park, J.-G.; Kim, J.-Y.; Park, J.-H.; Han, M. J.; Yu, J.; Hyeon, T., Synthesis, Characterization, and Self-Assembly of Pencil-Shaped CoO Nanorods. *J. Am. Chem. Soc.* **2006,** *128* (30), 9753-9760.

14. Buck, M. R.; Biacchi, A. J.; Schaak, R. E., Insights into the Thermal Decomposition of Co(II) Oleate for the Shape-Controlled Synthesis of Wurtzite-Type CoO Nanocrystals. *Chem. Mater.* **2014,** *26* (3), 1492-1499.

15. Zhang, Y.; Zhu, J.; Song, X.; Zhong, X., Controlling the Synthesis of CoO Nanocrystals with Various Morphologies. *J. Phys. Chem. C* **2008,** *112* (14), 5322-5327.

16. Unni, M.; Uhl, A. M.; Savliwala, S.; Savitzky, B. H.; Dhavalikar, R.; Garraud, N.; Arnold, D. P.; Kourkoutis, L. F.; Andrew, J. S.; Rinaldi, C., Thermal Decomposition Synthesis of Iron Oxide Nanoparticles with Diminished Magnetic Dead Layer by Controlled Addition of Oxygen. *ACS Nano* **2017,** *11* (2), 2284-2303.

17. Nedelkoski, Z.; Kepaptsoglou, D.; Lari, L.; Wen, T.; Booth, R. A.; Oberdick, S. D.; Galindo, P. L.; Ramasse, Q. M.; Evans, R. F. L.; Majetich, S.; Lazarov, V. K., Origin of Reduced Magnetization and Domain Formation in Small Magnetite Nanoparticles. *Sci. Rep.* **2017,** *7* (1).

18. Li, Q.; Wu, L.; Wu, G.; Su, D.; Lv, H.; Zhang, S.; Zhu, W.; Casimir, A.; Zhu, H.; Mendoza-Garcia, A.; Sun, S., New Approach to Fully Ordered fct-FePt Nanoparticles for Much Enhanced Electrocatalysis in Acid. *Nano Lett.* **2015,** *15* (4), 2468-2473.

19. Ma, Z.; Yue, M.; Liu, H.; Yin, Z.; Wei, K.; Guan, H.; Lin, H.; Shen, M.; An, S.; Wu, Q.; Sun, S., Stabilizing Hard Magnetic $SmCo_5$ Nanoparticles by N-Doped Graphitic Carbon Layer. *J. Am. Chem. Soc.* **2020,** *142* (18), 8440-8446.

20. Shen, B.; Yu, C.; Su, D.; Yin, Z.; Li, J.; Xi, Z.; Sun, S., A New Strategy to Synthesize Anisotropic $SmCo_5$ Nanomagnets. *Nanoscale* **2018,** *10* (18), 8735-8740.

21. Nogués, J.; Schuller, I. K., Exchange Bias. *J. Magn. Magn. Mater.* **1999,** *192* (2), 203-232.

22. You, C. Y.; Goripati, H. S.; Furubayashi, T.; Takahashi, Y. K.; Hono, K., Exchange Bias of Spin Valve Structure with a Top-Pinned $Co_{40}Fe_{40}B_{20}$/IrMn. *Appl. Phys. Lett.* **2008,** *93* (1).

23. González, J. A.; Andrés, J. P.; López Antón, R.; De Toro, J. A.; Normile, P. S.; Muñiz, P.; Riveiro, J. M.; Nogués, J., Maximizing Exchange Bias in Co/CoO Core/Shell Nanoparticles by Lattice Matching between the Shell and the Embedding Matrix. *Chem. Mater.* **2017,** *29* (12), 5200-5206.

24. Lottini, E.; López-Ortega, A.; Bertoni, G.; Turner, S.; Meledina, M.; Van Tendeloo, G.; de Julián Fernández, C.; Sangregorio, C., Strongly Exchange Coupled Core|Shell Nanoparticles with High Magnetic

Anisotropy: A Strategy toward Rare-Earth-Free Permanent Magnets. *Chem. Mater.* **2016,** *28* (12), 4214-4222.

25. Meiklejohn, W. H.; Bean, C. P., New Magnetic Anisotropy. *Phys. Rev.* **1957,** *105* (3), 904-913.

26. Carey, M. J.; Berkowitz, A. E., Exchange Anisotropy in Coupled Films of $Ni_{81}Fe_{19}$ with NiO and $Co_xNi_{1-x}O$. *Appl. Phys. Lett.* **1992,** *60* (24), 3060-3062.

27. Borchers, J. A.; Carey, M. J.; Erwin, R. W.; Majkrzak, C. F.; Berkowitz, A. E., Spatially Modulated Antiferromagnetic Order in CoO/NiO Superlattices. *Phys. Rev. Lett.* **1993,** *70* (12), 1878-1881.

28. Mandziak, A.; D. Soria, G.; Prieto, J. E.; Prieto, P.; Granados-Miralles, C.; Quesada, A.; Foerster, M.; Aballe, L.; de la Figuera, J., Tuning the Néel Temperature in an Antiferromagnet: the Case of $Ni_xCo_{1-x}O$ Microstructures. *Sci. Rep.* **2019,** *9* (1).

29. Bau, J. A.; Li, P.; Marenco, A. J.; Trudel, S.; Olsen, B. C.; Luber, E. J.; Buriak, J. M., Nickel/Iron Oxide Nanocrystals with a Nonequilibrium Phase: Controlling Size, Shape, and Composition. *Chem. Mater.* **2014,** *26* (16), 4796-4804.

30. Marusak, K. E.; Johnston-Peck, A. C.; Wu, W.-C.; Anderson, B. D.; Tracy, J. B., Size and Composition Control of CoNi Nanoparticles and Their Conversion into Phosphides. *Chem. Mater.* **2017,** *29* (7), 2739-2747.

31. Xu, W.; Ji, M.; Chen, Y.; Zheng, H.; Wang, L.; Peng, D.-L., Nickel Colloidal Superparticles: Microemulsion-Based Self-Assembly Preparation and Their Transition from Room-Temperature Superparamagnetism to Ferromagnetism. *J. Phys. Chem. C* **2021,** *125* (10), 5880-5889.

32. Bodnarchuk, M. I.; Kovalenko, M. V.; Groiss, H.; Resel, R.; Reissner, M.; Hesser, G.; Lechner, R. T.; Steiner, W.; Schäffler, F.; Heiss, W., Exchange-Coupled Bimagnetic Wüstite/Metal Ferrite Core/Shell Nanocrystals: Size, Shape, and Compositional Control. *Small* **2009,** *5* (20), 2247-2252.

33. Harres, A.; Mikhov, M.; Skumryev, V.; Andrade, A. M. H. d.; Schmidt, J. E.; Geshev, J., Criteria for Saturated Magnetization Loop. *J. Magn. Magn. Mater.* **2016,** *402*, 76-82.

34. Han, M. J.; Kim, H.-S.; Kim, D. G.; Yu, J., Collinear and Noncollinear Spin Ground State of Wurtzite CoO. *Phys. Rev. B* **2013,** *87* (18).

35. Roca, A. G.; Golosovsky, I. V.; Winkler, E.; López-Ortega, A.; Estrader, M.; Zysler, R. D.; Baró, M. D.; Nogués, J., Unravelling the Elusive Antiferromagnetic Order in Wurtzite and Zinc Blende CoO Polymorph Nanoparticles. *Small* **2018,** *14* (15).

36. Baranov, D.; Fiore, A.; van Huis, M.; Giannini, C.; Falqui, A.; Lafont, U.; Zandbergen, H.; Zanella, M.; Cingolani, R.; Manna, L., Assembly of Colloidal Semiconductor Nanorods in Solution by Depletion Attraction. *Nano Lett.* **2010,** *10* (2), 743-749.

# Chapter 3

# Colloidal Dipolar Superferromagnetism Held Together by Antiferromagnetic Glue

## 3.1 Introduction

Colloidal magnetic nanoparticles are material building blocks whose properties can be tuned to benefit a wide range of applications from biomedical separations,[1-3] sensing,[4-5] and imaging,[6-7] to data storage or spintronics.[8-11] Magnetite, or $Fe_3O_4$, is likely the most common magnetic phase used in nanoparticle form, owing to its chemical stability and an abundance of synthetic methods which can produce $Fe_3O_4$ in a variety of forms.[12-16] The development of synthetic methods has led to highly sophisticated, tunable nanoparticles with optimized crystallinity,[17-18] shape,[19] size,[14] and surfaces.[20-21] However, in its most fundamental nanoscale magnetic unit – a single phase, single domain, isotropic nanoparticle – even $Fe_3O_4$ is limited in its magnetic properties by the first two magnetic forces depicted in Figure 3.1: the Zeeman energy ($E_{Zeeman}$) and magnetocrystalline anisotropy energy ($E_{MCA}$). The Zeeman effect can be explained simply as favoring alignment of the nanoparticle's moment with the direction of an applied magnetic field. The magnetocrystalline anisotropy is tied to the symmetry of the nanoparticle's crystal structure, and thus favors orientation of the moment to certain crystallographic directions. The magnitudes of both forces depend intrinsically on the material constituting the nanoparticle and are

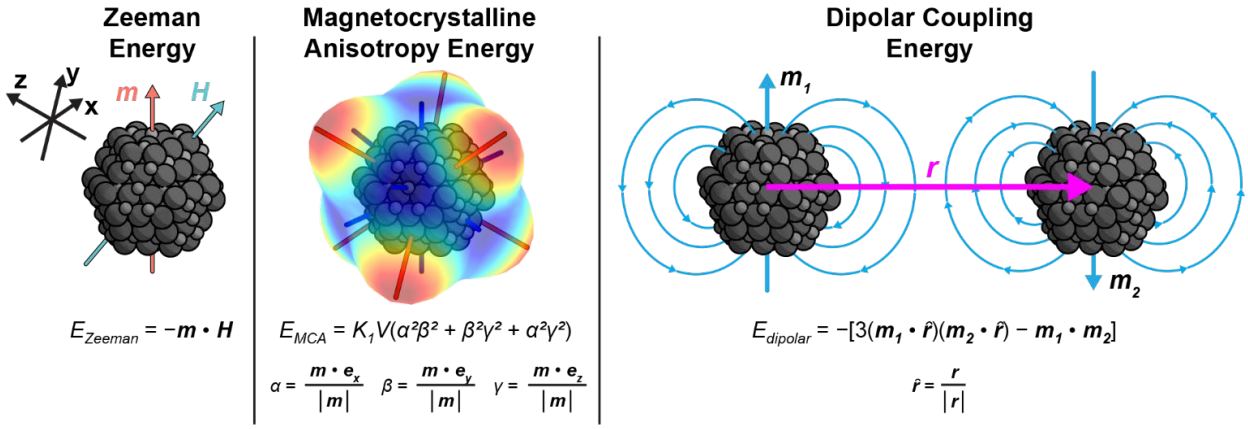


**Figure 3.1.** Depictions and equations of the magnetic energies governing the magnetic state of an $Fe_3O_4$ nanoparticle. Zeeman energy (left), $E_{Zeeman}$, depends on the relative alignment of the nanoparticle moment, $\boldsymbol{m}$, and the magnetic field vector, $\boldsymbol{H}$. Magnetocrystalline anisotropy energy (middle), $E_{MCA}$, is depicted as a surface whose radial magnitude and color denotes the magnitude of $E_{MCA}$ in a given direction. The red lines depict the direction of $E_{MCA}$ maxima, or hard axes, and the blue lines depict the direction of $E_{MCA}$ minima, or easy axes, which are favored orientations for the nanoparticle moment. Finally, dipolar coupling energy (right), can favor antiferromagnetic or ferromagnetic alignment of two nanoparticle moments depending on their relative position and orientation. Its magnitude is dependent on the interparticle distance, $\boldsymbol{r}$. $\boldsymbol{e}_x$, $\boldsymbol{e}_y$, and $\boldsymbol{e}_z$ are the Cartesian basis vectors.

multiplied by the nanoparticle's size. The Zeeman energy is proportional to the nanoparticle's moment, which depends on the intrinsic magnetization of the material, while the magnetocrystalline anisotropy energy is dependent on the material's anisotropy constant, $K$. Other factors which typically affect nanoparticle properties, like shape or surface chemistry, provide only small perturbations to the nanoparticle magnetism.[20, 22-23]

In applications requiring hard magnetism, the most limiting factor is the magnetocrystalline anisotropy, which sets an upper limit for the material's coercivity, $H_c$. Magnetite can be doped with Co to increase its anisotropy by over twenty times;[24] nanoparticles of $CoFe_2O_4$ ($d$ = 20 nm) can reach $H_c$ = 137 mT at room temperature.[8] Larger coercivities can be reached with other materials such as FePt or $SmCo_5$, but they are difficult to produce in robust, tunable nanoparticle forms. In order to break past the limits set by a material's intrinsic properties, a second phase can be introduced, which through interactions with the first phase, adds additional magnetic anisotropy. A powerful example of the biphasic approach is exchange bias, in which strong exchange coupling at the interface between a ferro- or ferrimagnet and an antiferromagnet can increase the coercivity by multiple orders of magnitude over the ferro/ferrimagnet

alone.[25] Exchange bias systems bring their own difficulties to study, as the constituent materials must be epitaxially compatible and the crucial interface between them is challenging to control, especially in colloidal nanoparticles.

Within ensembles of many nanoparticles, an alternate source of anisotropy emerges from the dipolar coupling between pairs of nanoparticles. The nature of dipolar coupling is antiferromagnetic when the nanoparticle moments are orthogonal to the interparticle axis, as shown in the two rightmost particles of Figure 3.1, but switches to ferromagnetic with nanoparticle moments parallel to the interparticle axis. The competition between the Zeeman, magnetocrystalline anisotropy, and dipolar energies in a random (in spatial distribution and/or orientation) ensemble of nanoparticles leads to a collective state of frustrated nanoparticle moments, or superspins. This state is termed a superspin glass for its similarity to the spin glass state found in dilute magnetic alloys, e.g. Au(Fe). Superspin glasses are commonly found in samples of magnetic nanoparticles which are often studied as random-close-packed powders, and strongly affect the magnetic behavior of the nanoparticles.[26-27] In this work, we study assemblies of antiferromagnetic CoO nanoparticles with $Fe_3O_4$ nanoparticles. These nanoparticle combinations are produced merely by mixing nanoparticle suspensions of each type together. In contrast to exchange bias systems, only dipolar coupling exists between the two phases, yet we observe large improvements to the coercivity. We show that the presence of antiferromagnets in the nanoparticle ensembles produces a superferromagnetic state rather than a superspin glass, which is responsible for the coercivity enhancement.

## 3.2 Results and Discussion

### 3.2.1 Magnetic Properties of $Fe_3O_4$ Nanoparticles

$Fe_3O_4$ nanoparticles were synthesized based on methods first reported by Park *et al.*,[14] in which an iron oleate precursor was thermally decomposed using oleic acid as a surfactant and 1-octadecene as the solvent. Transmission electron microscopy (TEM) analysis revealed the formation of monodisperse

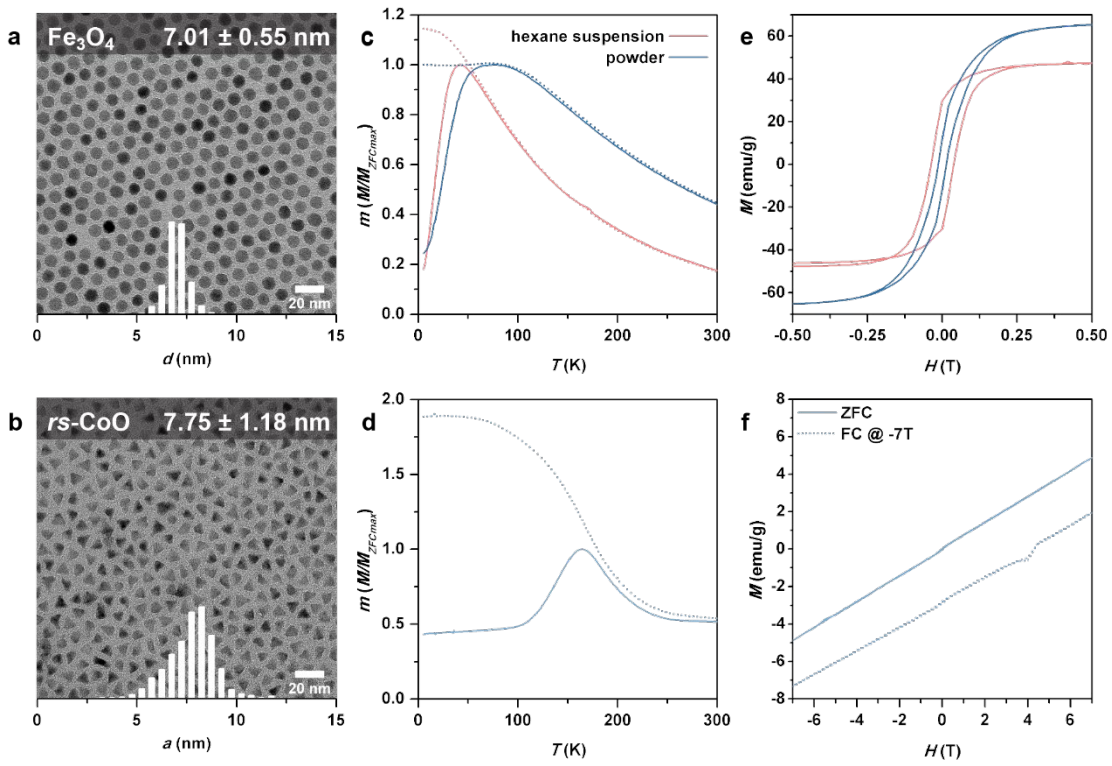


**Figure 3.2.** Transmission electron micrographs (TEM) of a) $Fe_3O_4$ and b) *rs*-CoO nanoparticles with overlaid size histograms. Plots of normalized magnetization vs temperature under zero-field-cooled (ZFC, solid lines) and field-cooled (FC, dotted lines) with an applied field of 0.01 T for c) $Fe_3O_4$ and d) *rs*-CoO nanoparticles. The moments were normalized to the maximum ZFC magnetization. Magnetization vs magnetic field at 5 K for the e) $Fe_3O_4$ and f) *rs*-CoO nanoparticles.

spherical nanoparticles (Figure 3.2a). The magnetic properties of the $Fe_3O_4$ nanoparticles were established through zero-field cooled (ZFC) and field cooled (FC) warming curves and hysteresis loop measurements done with a superconducting quantum interference device (SQUID) magnetometer. Two $Fe_3O_4$ nanoparticle samples were prepared: a dilute hexane suspension (0.25 mg/mL) to study the isolated single particle properties, and a dry, compacted powder. The hexane suspension of $Fe_3O_4$ NPs has a ZFC warming curve which shows a narrow peak at $T_p$ = 40 K, indicating the set of $Fe_3O_4$ NPs has a narrow distribution of blocking temperatures. Its low temperature FC magnetization starts well above the ZFC peak magnetization, then continually decreases with increasing temperature, converging with the ZFC curve shortly after the ZFC peak at $T_p$ = 40 K. On the other hand, the ZFC curve of the powder sample displays a much broader peak at a higher temperature ($T_p$ = 75 K); the low temperature FC magnetization is roughly equal to the ZFC peak magnetization value but dips below the ZFC peak before converging with the ZFC

curve at temperatures above $T_p$. Both the broadness of the ZFC peak and its increased $T_p$ for the powder sample are indicative of a superspin glass, a state resulting from the random, frustrated interactions between the closely spaced nanoparticles.[27-30]

The influence of the superspin glass state on hysteresis loops of magnetic nanoparticles has not been widely reported. It is often stated that direct exchange interactions between particles are magnetizing while dipolar interactions are demagnetizing, but we have found no systematic measurements of hysteresis loops of samples with varying interparticle interaction strengths. Figure 3.2e shows hysteresis loops of magnetization vs. magnetic field for both $Fe_3O_4$ samples, measured between –7 and 7 T at 5 K. The dilute hexane suspension sample shows a considerably lower saturation magnetization than the powder sample due to error stemming from the small mass of $Fe_3O_4$ present in that sample (~10 μg). Additionally, each point in the hysteresis loop of the hexane suspension sample required significant background subtraction of the diamagnetic signal from hexane. While the isolated $Fe_3O_4$ nanoparticles in the hexane suspension have a coercivity of $H_c$ = 33 mT, that is reduced to $H_c$ = 14 mT in the powder sample. Because the nanoparticles are coated with oleic acid ligands, it is assumed that they are not in contact with each other and can only interact through dipolar coupling. As described in the literature, the addition of dipolar interactions to the $Fe_3O_4$ nanoparticles reduces their coercivity or demagnetizes them.[31]

### 3.2.2 Magnetic Properties of *rs*-CoO Nanoparticles

*rs*-CoO nanoparticles were synthesized based on methods first reported by Zhang *et al.*,[32] in which a cobalt oleate precursor was thermally decomposed with oleyl alcohol and 1-octadecene. Based on the triangular cross-sections shown in TEM of the resulting product, we deduce that tetrahedral nanoparticles were formed. ZFC and FC warming curves were also collected on a compacted powder of the *rs*-CoO nanoparticles (Figure 3.2d). The ZFC warming curve starts at a low magnetization at low temperatures, gradually increasing to a peak near $T_p$ = 160 K, then decaying back to its low temperature value. The FC curve monotonically decreases as the temperature is increased, nearing the ZFC curve above $T_p$ but never overlapping. The *rs*-CoO nanoparticles display similar temperature dependent magnetization behavior to

the isolated $Fe_3O_4$ nanoparticles despite the *rs*-CoO phase being antiferromagnetic. This behavior can be attributed to uncompensated spins existing from defects or on the surface of the nanoparticles, which collectively give a ferromagnetic signal.[33] The presence of a peak in the ZFC warming curve indicates that these uncompensated spins are correlated below $T_p \sim 160$ K but are thermally decoupled into a superparamagnetic state at higher temperatures. Measurements of magnetic moment versus field between –7 and 7 T at $T = 5$ K further illustrate the presence of the uncompensated spins.[34] When the *rs*-CoO nanoparticles were cooled to $T = 5$ K without an applied field, their moment was proportional to the magnitude of the applied field. This proportional (and very small) susceptibility represents the purely antiferromagnetic response to an applied field wherein the spin sublattices of the antiferromagnet are slightly canted by the applied field. When the *rs*-CoO nanoparticles were cooled to $T = 5$ K under $H = –7$ T, their moment maintained a linear relationship with the applied field, having the same susceptibility but with a negative vertical offset. Under FC conditions, the uncompensated spins are strongly pinned by the antiferromagnetic core in the direction of the applied field, such that they maintain their orientation throughout the field scan from –7 to 7 T.

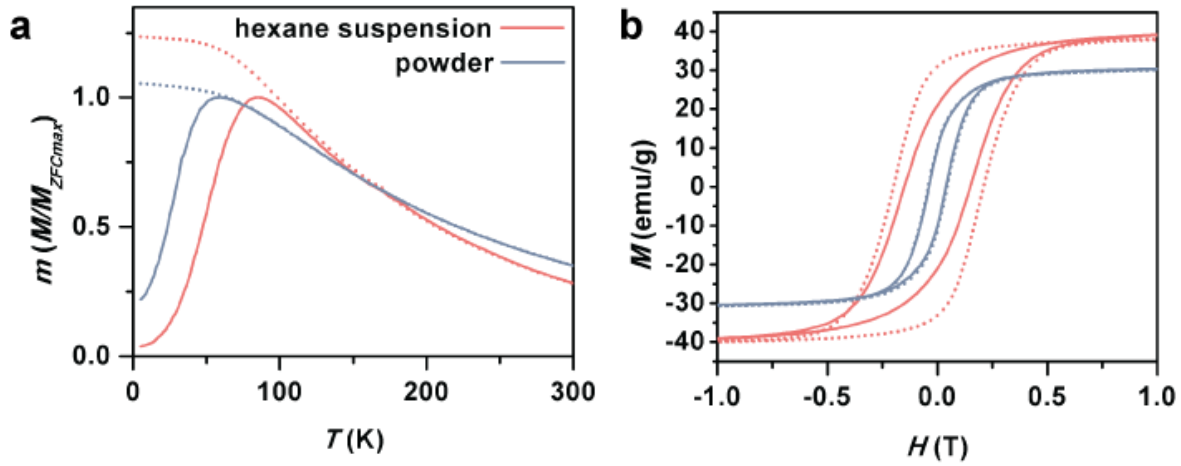


**Figure 3.3.** a) Plots of magnetization vs temperature with a field of 0.01 T under ZFC (solid lines) and FC (dotted lines) conditions and b) plots of magnetization vs field at 5 K under ZFC (solid lines) and FC ($H_{FC}$ = –7 T, dotted lines) conditions for the mixed $Fe_3O_4$ and *rs*-CoO samples.

### 3.2.3 Superferromagnetism in Mixed Assemblies of $Fe_3O_4$ and *rs*-CoO Nanoparticles

Hexane suspensions of the $Fe_3O_4$ and *rs*-CoO nanoparticles were combined to form a mixed suspension (1:1 mass ratio, 50 mg/mL based on total mass of both types of nanoparticles). One portion of the mixed suspension was dried to a powder, while another portion was sealed within a quartz tube. In measurements of magnetic moment versus temperature, both mixed samples showed evidence of only one magnetic phase, with only one ZFC peak visible in each curve in Figure 3.3a. The $Fe_3O_4$ and *rs*-CoO nanoparticles must be strongly coupled, even in the non-close-packed hexane suspension sample. A back-of-the-envelope calculation based on the concentration of nanoparticles in suspension indicates that they are about 60 nm apart. The mixed samples' magnetization values in the ZFC warming measurement both peak at a higher temperature, at $T_p = 60$ K for the powder sample and at $T_p = 85$ K for the hexane suspension, than for the isolated $Fe_3O_4$ nanoparticles (*cf.* $T_p = 75$ and 40 K, respectively). Neither sample shows the broad ZFC peak or the low temperature FC dip associated with the presence of a superspin glass. Given the much smaller moment of the *rs*-CoO nanoparticles compared to the $Fe_3O_4$ nanoparticles, the dipolar interactions are expected to be much weaker in the mixed powder compared to the purely $Fe_3O_4$ powder. This relation was indeed observed in the lower ZFC peak temperature of the mixed powder. Surprisingly, the mixed hexane suspension has an even higher ZFC peak temperature than either the $Fe_3O_4$ or mixed powders despite its dipolar interactions being further weakened by the distancing of its nanoparticles from each other.

Measurements of magnetic moment versus field were conducted on the mixed samples at $T = 5$ K both after cooling without an applied field (ZFC) and after cooling under $H = -7$ T (FC). The mixed powder sample had a slightly enhanced coercivity, $H_c = 40$ mT, over the isolated $Fe_3O_4$ nanoparticles in dilute hexane suspension, with a negligible difference between its ZFC and FC hysteresis loops. Meanwhile, the mixed hexane suspension had a greatly enhanced ZFC coercivity of $H_c = 150$ mT, almost five times that of the isolated $Fe_3O_4$ nanoparticles. The $T_p$ and $H_c$ values for the $Fe_3O_4$ samples and mixed $Fe_3O_4$ and *rs*-CoO samples can be compared in Table 3.1. We propose that the $Fe_3O_4$ nanoparticles are being oriented into a superferromagnetic state induced by dipolar interactions with the antiferromagnetic *rs*-CoO nanoparticles.

To our knowledge, this is the first observation of superferromagnetism arising solely from dipolar interparticle interactions. Previous reports of dipolar superferromagnetism have depended on the magnetostatic energy stemming from the anisotropic arrangement of an ensemble of nanoparticles.[35-36] The superferromagnetic state consists of the nanoparticle magnetic moments interacting with each other to form a ferromagnetically ordered alignment. This would explain the lack of superspin glass behavior in the mixed samples' ZFC and FC warming curves, as superspin glasses are characterized by randomness in the superspin orientations.

**Table 3.1.** ZFC peak temperatures and coercivities compared between the $Fe_3O_4$ samples and the mixed $Fe_3O_4$ and *rs*-CoO samples.

| Material | Sample Form | $T_p$ (K) | $H_c$ (mT) | |
|---|---|---|---|---|
| | | | ZFC | FC ($H_{FC}$ = –7 T) |
| $Fe_3O_4$ | Dilute hexane suspension (0.25 mg/mL) | 40 | 33 | 33 |
| | Conc. hexane suspension (25 mg/mL) | 50 | 34 | 39 |
| | Powder | 75 | 14 | 14 |
| $Fe_3O_4$ + *rs*-CoO | Conc. hexane suspension (50 mg/mL) | 85 | 150 | 200 |
| | Conc. docosane suspension (50 mg/mL) | 72 | 50 | 50 |
| | Powder | 60 | 40 | 40 |

The superferromagnetism hypothesis is supported by hysteresis loop measurements of a n-docosane suspension of mixed nanoparticles (1:1 mass ratio, 50 mg/mL based on total mass of both types of nanoparticles) (Figure 3.6). This n-docosane suspension was prepared with liquid n-docosane ($T_f$ = 318 K) which was allowed to freeze at room temperature after the nanoparticles were suspended homogenously within it. The ZFC and FC hysteresis loops of the n-docosane suspension were nearly identical to those of the mixed powder sample, with a slight difference in saturation magnetization likely due to sample mass error. In both the mixed powder and the mixed n-docosane suspension, the orientation of the nanoparticles

is fixed at or above room temperature, where the $Fe_3O_4$ and *rs*-CoO nanoparticles are both superparamagnetic and undergo Neel relaxation before reorienting themselves (Brownian relaxation). In this scenario, the nanoparticles would be frozen in a random orientation with negligible influence from interparticle interactions. While the spatial distribution of nanoparticles within the hexane suspension should be similar to that of the n-docosane suspension, the orientation of the nanoparticles in the hexane suspension is fixed at the freezing point of hexane ($T_f$ = 178 K). At this temperature, the nanoparticles' Neel relaxation slows and allows the dipolar interactions to align the nanoparticles into the superferromagnetic state. When the mixed hexane suspension was cooled under $H$ = –7 T, its coercivity was further increased to $H_c$ = 200 mT, over 5 times that of the $Fe_3O_4$ hexanes suspension. In the FC measurement, the nanoparticles still enter the superferromagnetic state, but their easy axes align specifically with the magnetic field direction. As predicted by Stoner Wohlfarth theory, parallel alignment between the magnetic field and the nanoparticles' easy axes maximizes their coercivity; the same particles aligned orthogonally to the field would have zero coercivity.[37]

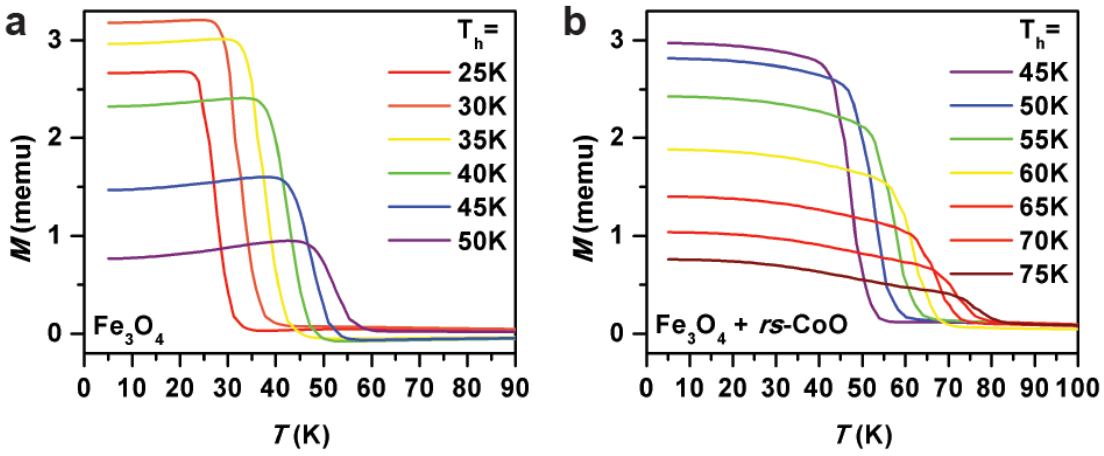


**Figure 3.4.** Plots of isothermal remanent magnetization after cooling under zero-field, with a field stop ($H$ = 0.005 T, wait time of 300 s) at $T_h$ for hexane suspensions of a) the $Fe_3O_4$ nanoparticles (25 mg/mL) and b) the mixed $Fe_3O_4$ and *rs*-CoO nanoparticles (50 mg/mL total).

It is surprising that purely dipolar interactions between non-close-packed nanoparticles are sufficient to boost the mixed hexane suspension's coercivity by five to six times over the $Fe_3O_4$ nanoparticles' intrinsic coercivity. In the $Fe_3O_4$ powder, the dipolar interactions were demagnetizing and

decreased the sample's coercivity. Additionally, in a hexane suspension of $Fe_3O_4$ nanoparticles prepared at the same concentration of $Fe_3O_4$ in the mixed suspension (25 mg/mL), the same coercivity was obtained as for the isolated $Fe_3O_4$ nanoparticles (Figure 3.7). Measurements of the mixed hexane suspension's remanent magnetization after isothermal remanent magnetization (IRM) and direct current demagnetization (DCD) were performed in order to characterize the interparticle interactions present in the sample. The IRM and DCD remanent magnetizations can be combined to calculate $\Delta M(H) = m_{DCD}(H) - 1 + 2m_{IRM}(H)$.[38] The $\Delta M$ versus field plot in Figure 3.8 shows a negative, asymmetric peak in $\Delta M$, indicating that the dominant interaction between particles must be dipolar.

Measurements of isothermal remanent magnetization (IRM) while warming after a field stop at a holding temperature, $T_h$, were performed on hexane suspensions of $Fe_3O_4$ (25 mg/mL) and mixed $Fe_3O_4$ and *rs*-CoO (50 mg/mL total). The samples were first cooled to a temperature below the ZFC peak, $T_h$, without an applied field. Upon reaching $T_h$, a field of $H$ = 5 mT was applied for $t$ = 300 s, then removed. The samples were cooled to $T$ = 5 K and their magnetizations were measured as they were warmed. This measurement procedure is depicted graphically in Figure 3.9. The IRM warming curves for the $Fe_3O_4$ nanoparticles (Figure 3.4a) start at a high magnetization and remain relatively constant as the sample is warmed. As they approach $T_h$ however, the IRM begins to climb; it peaks then drops precipitously just prior to reaching $T_h$. The IRM peaks near each $T_h$ indicates Heisenberg (three-dimensional) spin dimensionality in (super)spin glasses; in other words the nanoparticle superspins can relax through all orientations.[39-41] Although this analysis has previously been done only for (super)spin glasses, we believe it is applicable to our superferromagnet as well, as it is based on a similar ensemble of dipolar-interacting nanoparticles. This result of Heisenberg spin dimensionality reflects the small, cubic magnetocrystalline anisotropy of $Fe_3O_4$. In contrast, with the addition of *rs*-CoO nanoparticles in the mixed sample, the IRM curves (Figure 3.4b) monotonically decrease with increasing temperature, with a precipitous drop again near $T_h$. The monotonic IRM decrease indicates Ising (one-dimensional) spin dimensionality, which must be contributed by the *rs*-CoO nanoparticles. Because they are antiferromagnetic, the *rs*-CoO nanoparticles are not subject to strong

Zeeman forces and can maintain their spin orientation throughout the field range available to us. The orientation of the *rs*-CoO nanoparticle moments is transmitted to the $Fe_3O_4$ nanoparticle moments through dipolar coupling, giving the $Fe_3O_4$ nanoparticles an additional uniaxial anisotropy which results in the enhanced coercivity of the mixed hexane suspension sample.

The coercivity enhancement associated with dipolar superferromagnetism was also produced with combinations of $Fe_3O_4$ with other nanoparticles. CoO nanoparticles can be synthesized in a wurtzite phase by thermal decomposition of cobalt oleate.[42-43] *wz*-CoO is also antiferromagnetic, but its magnetic structure and properties are not well understood because it only exists on the nanoscale.[33, 44-45] Two morphologies of *wz*-CoO were synthesized, cones and pencil-shaped rods, each possessing slightly different antiferromagnetic properties (Figure 3.10). When the *wz*-CoO nanoparticles were mixed with $Fe_3O_4$

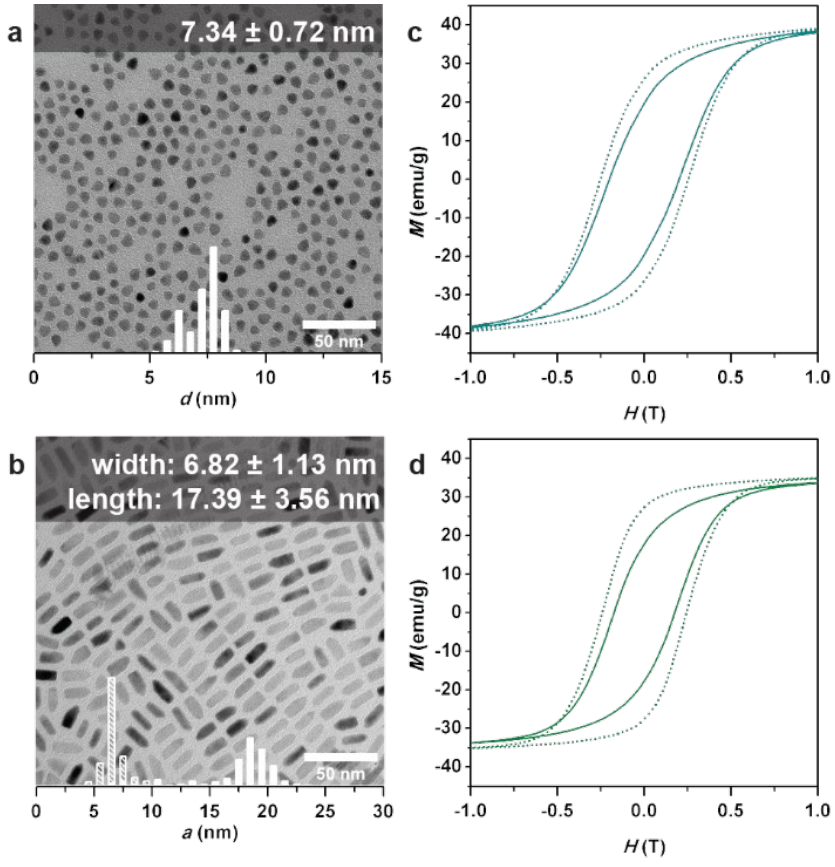


**Figure 3.5.** TEM of *wz*-CoO a) cone-shaped and b) pencil/rod-shaped nanoparticles with overlaid size histograms. Plots of magnetization vs field at 5 K after ZFC (solid lines) and FC ($H$ = –7 T, dotted lines) for mixed hexane suspensions of $Fe_3O_4$ with *wz*-CoO c) cones and d) rods.

nanoparticles in hexane suspensions (1:1 mass ratio, 50 mg/mL by total mass), hysteresis loops of the mixed suspensions, shown in Figure 3.5c-d, again showed greatly enhanced coercivity over the $Fe_3O_4$ nanoparticles. With three different types of antiferromagnetic nanoparticles each producing superferromagnetism when mixed with $Fe_3O_4$ nanoparticles, it is clear that their antiferromagnetism is the crucial ingredient. Further study is needed to elucidate how antiferromagnetic properties affect the superferromagnetism in mixed samples.

## 3.3 Conclusion

We have produced the first instance of superferromagnetism in nanoparticle assemblies which interact only through dipolar interactions. The superferromagnetism is achieved by addition of antiferromagnetic CoO nanoparticles to ferrimagnetic $Fe_3O_4$ nanoparticles in frozen hexane suspensions; it manifests despite the weakened dipolar coupling in the non-close-packed nanoparticles. The presence of the antiferromagnetic nanoparticles in suspension causes the nanoparticles to align themselves with each other before being frozen with the hexane. Superferromagnetism is not produced in n-docosane suspensions or powder samples, in which the nanoparticles are unable to reorient themselves, nor does it appear in hexane suspensions of $Fe_3O_4$ nanoparticles alone. The alignment between CoO and $Fe_3O_4$ nanoparticles adds a uniaxial magnetic anisotropy to the $Fe_3O_4$ nanoparticles, resulting in samples with coercivities five to six times greater than the $Fe_3O_4$ nanoparticles themselves. This result is reproduced with three different types of CoO nanoparticles, each having different morphologies and magnetic properties, but sharing in their antiferromagnetism. This discovery demonstrates a simple and exciting method to extend the properties of magnetic nanoparticles past their intrinsic limits, with a significant material parameter space yet to be explored.

## 3.4 Methods

### 3.4.1 Materials

The nanoparticle synthesis reagents used were iron(III) chloride hexahydrate (97% Sigma-Aldrich), cobalt(II) chloride hexahydrate (98–102%, Fisher Scientific), sodium oleate (97%, TCI), oleic acid (90%, Sigma-Aldrich), oleyl alcohol (85%, Sigma-Aldrich), 1-octadecanol (99%, Sigma-Aldrich), 1-octadecene (90%, Sigma-Aldrich). n-docosane (99%) was purchased from Acros Organics. ACS grade hexane and ethanol were purchased from Fisher. All chemicals were used as received.

### 3.4.2 Synthesis of Metal Oleate Precursors

Iron oleate and cobalt oleate were synthesized according to literature procedures.[14, 46] For iron oleate, iron(III) chloride hexahydrate (4.1 g, 15 mmol) and sodium oleate (13.7 g, 45 mmol) were combined in a 250 mL two-neck round bottom flask with water (30 mL), ethanol (23 mL), and hexane (53 mL). For cobalt oleate, cobalt(II) chloride (3.6 g, 15 mmol) and sodium oleate (9.2 g, 30 mmol) were combined in a 250 mL two-neck round bottom flask with water (30 mL), ethanol (23 mL), and hexane (53 mL). For both precursors, the flask was connected to a thermometer and adapter in its side neck and a water-cooled condenser in its central neck. The flask was then placed in an oil bath (95°C) and brought to reflux (70°C) under a nitrogen blanket (5.5 psig) for four hours. After being cooled to room temperature, the upper organic layer of the reaction mixture was separated and washed with water (30 mL) three times using a separatory funnel. Hexane was evaporated completely from the iron oleate complex, leaving a viscous, red-brown product. This product was stored in a vacuum oven at 70°C for 24 hrs, then dissolved in 1-octadecene (1.4 M) and stored under vacuum in a Schlenk flask. In the case of cobalt oleate, hexane was partially evaporated from the product; 1-octadecene was added to the vivid violet product solution (1.4 M) before continuing to evaporate the hexane. Upon complete removal of hexane, the cobalt oleate/1-octadecene solution was stored under vacuum in a Schlenk flask.

### 3.4.3 Synthesis of $Fe_3O_4$ Nanoparticles

$Fe_3O_4$ nanoparticles were synthesized with modifications of methods first reported by Park et al.[14, 18, 47] The prepared iron oleate/1-octadecene solution (10 mL, 1.4 mmol of iron oleate) was combined with oleic acid (0.7 mmol) in a 50 mL three-neck Morton flask. The Morton flask was connected to a Liebig condenser, thermocouple with adapter, and a stopcock flow adapter, and placed in a heating mantle controlled by a PID temperature controller. The reaction mixture was degassed and backfilled with dinitrogen three times at room temperature, then was brought to 110°C under vacuum. After 30 min the system was backfilled with nitrogen. For the rest of the reaction, 100 sccm of dinitrogen was flowed through the reaction system through a side neck of the Morton flask, out of the condenser attached to the middle neck, and through an oil bubbler. The reaction mixture was heated to 320°C at 3°C/min. After holding at 320°C for 20 min, 5 sccm of dioxygen was added to the gas stream, and the reaction was held at 320°C for another 20 min before being cooled to room temperature.

### 3.4.4 Synthesis of CoO Nanoparticles

*rs*-CoO tetrahedral nanoparticles were synthesized according to a modified literature procedure.[32] Cobalt oleate/1-octadecene solution (20 mL, 2.8 mmol of cobalt oleate) was combined with oleyl alcohol (7.52 g, 14 mmol) in a 100 mL three-neck Morton flask, which was connected to a Liebig condenser, thermocouple with adapter, and a stopcock flow adapter. The flask was placed in a heating mantle controlled by a PID temperature controller. The reaction mixture was degassed and backfilled with dinitrogen three times at room temperature, then was brought to 110°C under vacuum for 30 min. The system was backfilled with dinitrogen, after which 100 sccm of dinitrogen was flowed through the reaction system in the same way as for the $Fe_3O_4$ nanoparticles. The reaction mixture was heated to 320°C at 3°C/min, where it was refluxed for 20 min, then cooled to room temperature. The originally violet cobalt oleate turned a bright royal blue above 110°C and darkened as the reaction proceeded, reaching a dark navy blue around 300°C. Just before reflux, around 318°C, the reaction mixture turned red-brown, indicating the nucleation of *rs*-

CoO nanoparticles. Soon after the nucleation, the growth of the nanoparticles turned the reaction mixture a murky tan.

*wz*-CoO pencil shaped nanorods were synthesized according to a modified literature procedure.[43] Cobalt oleate/1-octadecene solution (10 mL, 1.4 mmol of cobalt oleate) was added to a 50 mL three-neck Morton flask similarly to the preceding syntheses. After degassing, the system was backfilled with dinitrogen and 50 sccm of dinitrogen was flowed through the reaction system. The reaction mixture was heated to 320°C at 3°C/min, where it was refluxed for 20 min, then cooled to room temperature. The reaction followed a similar series of color changes to the *rs*-CoO synthesis until it reached 300°C, but remained a dark navy blue at reflux. After a few minutes at reflux, the reaction mixture appeared to be a murky slate blue. When the reaction was stopped after 20 min at reflux, the final product had an additional green tinge.

*wz*-CoO cone shaped nanoparticles were synthesized similarly to the *wz*-CoO nanorods above. However, at 310°C liquid 1-octadecanol (3.79 g, 14 mmol) was injected into the reaction mixture. The flow adapter used in the previous syntheses was replaced with an addition funnel equipped with a glass stopcock three-way valve in its equalizing arm (Chemglass AF-0547-G-01). Dinitrogen could be flowed (100 sccm) through the three-way valve to the equalizing arm and into the Morton flask, bypassing the addition funnel prior to injection. The injection was performed by opening the funnel's lower stopcock and switching the three-way valve to flow dinitrogen into the addition funnel. The entirety of the 1-octadecanol in the addition funnel was forced out within seconds due to the pressure of the dinitrogen source (~3.5 psig). The injection dropped the reaction temperature to 260°C, which recovered to 320°C after 6 min. The reaction mixture was held at 320°C for 20 min, then cooled to room temperature. The reaction mixture appeared similar to the *wz*-CoO nanorod synthesis up until the injection of 1-octadecanol. After the injection, the reaction mixture remained a dark navy blue, but turned a murky green-blue around 290°C, remaining this color for the duration of the reaction.

### 3.4.5 Purification of Nanoparticles

Following each synthesis of nanoparticles, the reaction mixture was cooled to room temperature then diluted with hexane (30 mL), and ethanol (40 mL) was added as an antisolvent. The resulting mixture was distributed between four centrifuge tubes (50 mL) and centrifuged (8500 rpm, 9289 rcf, 7 min) in order to collect the precipitated nanoparticles in the pellet. The collected nanoparticles were redispersed in hexane (20 mL), and ethanol (20 mL) was added for a second round of centrifugation. Following this step, the resulting pellet of nanoparticles was redispersed and stored in hexane.

### 3.4.6 Characterization

Transmission electron microscopy was performed using an FEI Spirit TEM operating at 120kV. Micrographs were collected by a 2k x 2k Gatan CCD camera. The TEM samples were prepared by drying a dilute hexane suspension of nanoparticles on carbon-coated copper grids. Nanoparticle size analysis was performed using ImageJ with the Huang thresholding algorithm, with a minimum sample size of N = 480 for each batch of nanoparticles.[48]

Magnetic measurements were performed with a Quantum Design MPMS3 SQUID Magnetometer. Hexane suspension samples were prepared for magnetic characterization in custom quartz tubes (D&G Glassblowing, Inc.). After being loaded into a tube, the hexane suspensions were degassed with one freeze-pump-thaw cycle, then refrozen. The quartz tubes were then flame-sealed under static vacuum. Dry powder samples were prepared by packing a portion of powder into VSM Powder Sample Holders (Quantum Design 4096-388). n-docosane suspensions were melted then dispensed into polycarbonate capsules (Quantum Design AGC3) and allowed to resolidify.

Powder X-ray diffraction was performed with a Bruker Diffractometer with a Mo Kα radiation source equipped with an Apex II Area Detector.

## 3.5 Acknowledgements

Chapter 3, in full, is currently being prepared as a manuscript for publication by Zhou, B.H. and Rinehart, J.D. The dissertation author was the principal researcher and author of this material.

## 3.6 Additional Figures

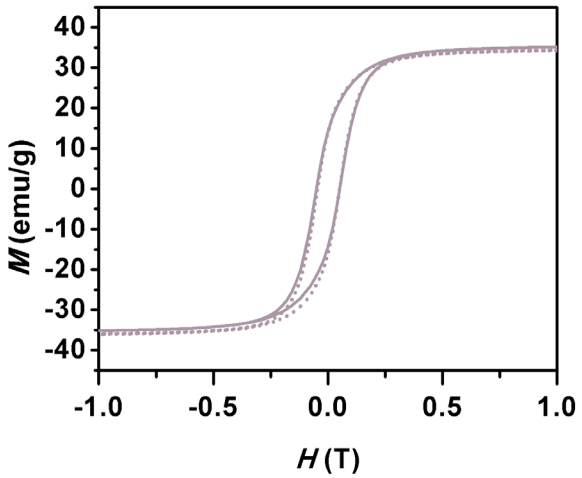


**Figure 3.6.** Zero-field-cooled (ZFC, solid lines) and field-cooled (FC, $H_{FC}$ = –7 T, dotted lines) magnetization vs magnetic field for a mixture of $Fe_3O_4$ and *rs*-CoO nanoparticles suspended in n-docosane.

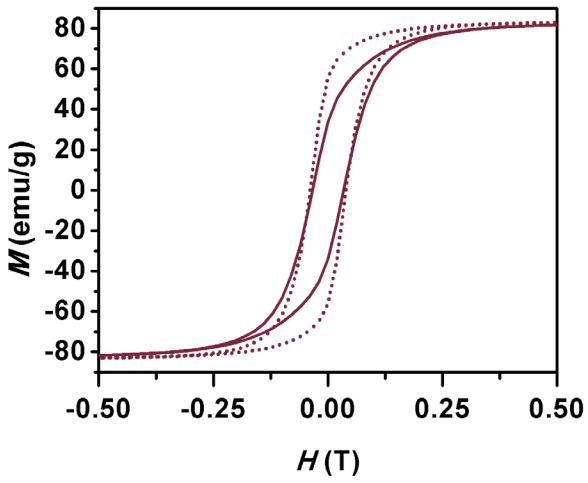


**Figure 3.7.** Zero-field-cooled (ZFC, solid lines) and field-cooled (FC, $H_{FC}$ = –7 T, dotted lines) magnetization vs magnetic field for a hexane suspension of $Fe_3O_4$ nanoparticles (25 mg/mL).

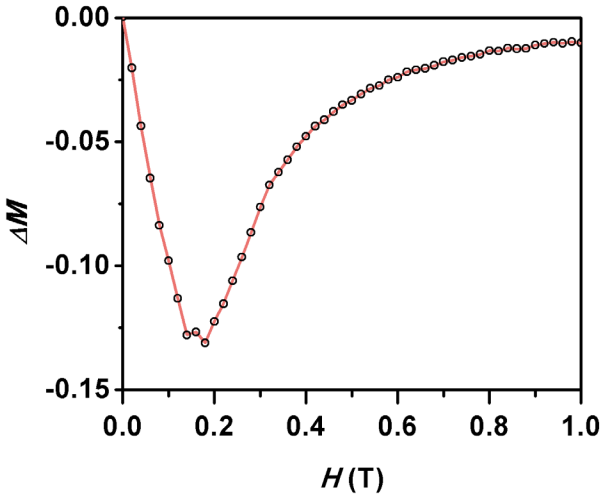


**Figure 3.8.** Plot of $\Delta M$ vs magnetic field for the mixed $Fe_3O_4$ and *rs*-CoO nanoparticles in hexane suspension (50 mg/mL).

To obtain the $\Delta M$ vs magnetic field data in Figure 3.8, remanent magnetization was measured after isothermal remanent magnetization (IRM) and direct current demagnetization (DCD) protocols. In the IRM protocol, the sample was cooled to 5 K in a demagnetized state (zero-field-cooled). A magnetic field, $H$, was applied and then removed, at which point the IRM remanent magnetization, $M_{IRM}$, was measured. This measurement was repeated for $0 \leq H \leq 7$ T. In the DCD protocol, the sample was cooled to 5 K then magnetically saturated with an applied field of –7 T. The field was removed and a reverse field, $H$, was applied. The DCD remanent magnetization, $M_{DCD}$, was then measured. $M_{DCD}$ was again measured for $0 \leq H \leq 7$ T.

Following this data collection procedure, $\Delta M(H)$ was calculated as

$$\Delta M(H) = -m_{DCD}(H) - 1 + 2m_{IRM}(H) \qquad \textbf{Equation 3.1}$$

where $m_{DCD}(H)$ and $m_{IRM}(H)$ are the reduced remanent magnetizations $M_{DCD}(H)/M_{DCD}(7\text{ T})$ and $M_{IRM}(H)/M_{IRM}(7\text{ T})$, respectively.

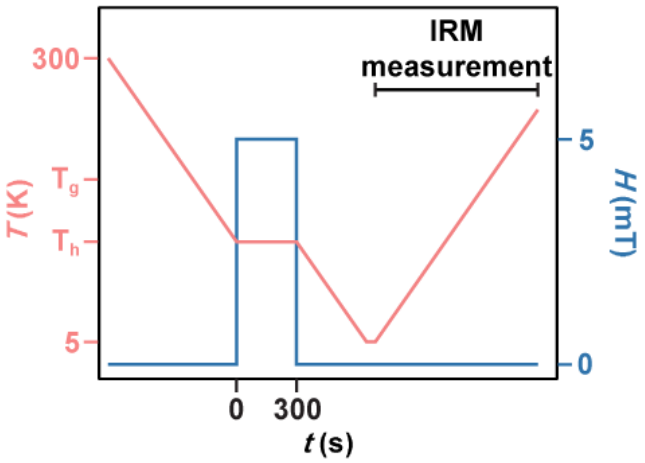


**Figure 3.9.** Graphical depiction of the measurement protocol for measuring isothermal remanent magnetization (IRM) warming curves after a field stop at a holding temperature $T_h$.

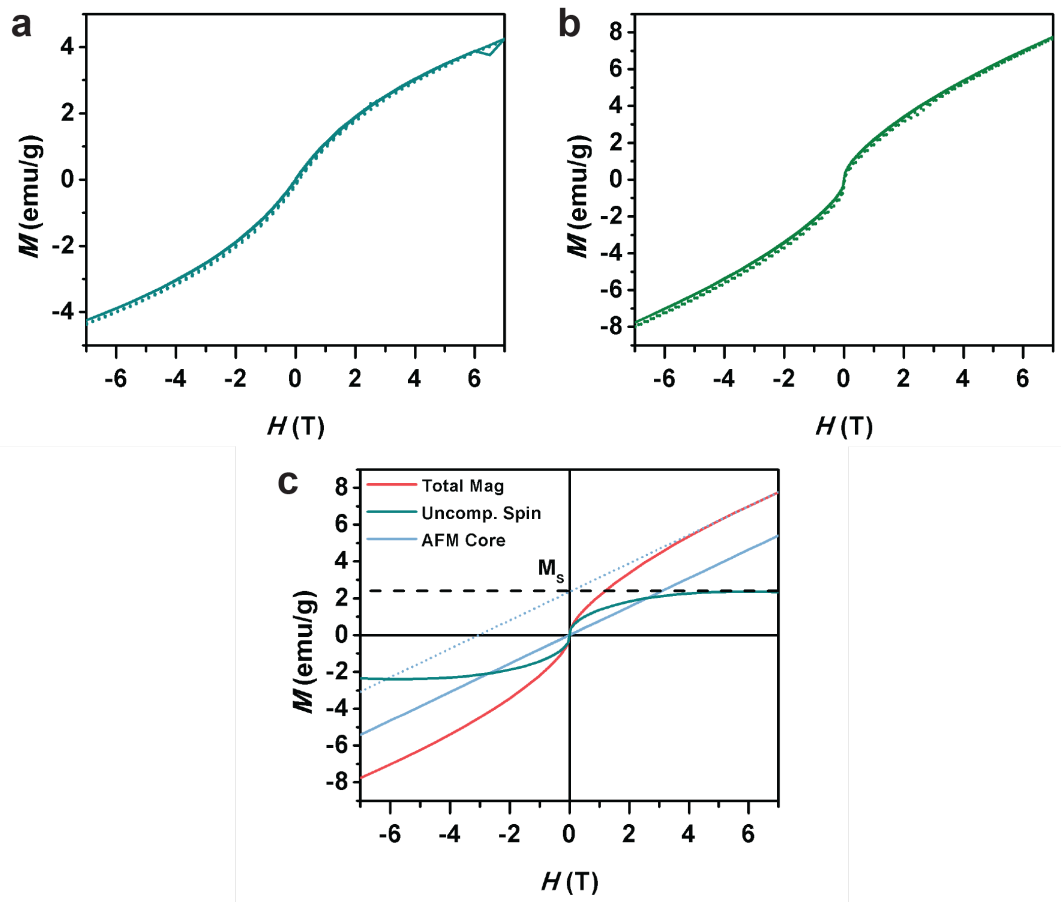


**Figure 3.10.** Zero-field-cooled (ZFC, solid lines) and field-cooled (FC, $H_{FC}$ = –7 T, dotted lines) magnetization vs magnetic field for powders of *wz*-CoO (a) cone-shaped and (b) pencil/rod-shaped nanoparticles. (c) ZFC magnetization vs magnetic field for *wz*-CoO pencil/rod shaped nanoparticles, with additional explanation of the antiferromagnetic behavior in *wz*-CoO.

As opposed to *rs*-CoO, the uncompensated spins in *wz*-CoO are not strongly pinned to the antiferromagnetic core, as shown by the minimal vertical shift between the ZFC and FC curves in Figure 3.10a,b. Decoupled from the antiferromagnetic core, they display ferromagnetic behavior with a sharp increase in magnetization at small fields, then quickly saturating at larger fields.

The magnetic response of the antiferromagnetic core is assumed to be proportional to the applied field, while the uncompensated spins are expected to be completely saturated at large fields. Therefore, antiferromagnetic susceptibility can be found by fitting the slope of the total magnetization at high field. Subtracting a line with this slope and zero intercept from the total magnetization yields the ferromagnetic response of the uncompensated spins.

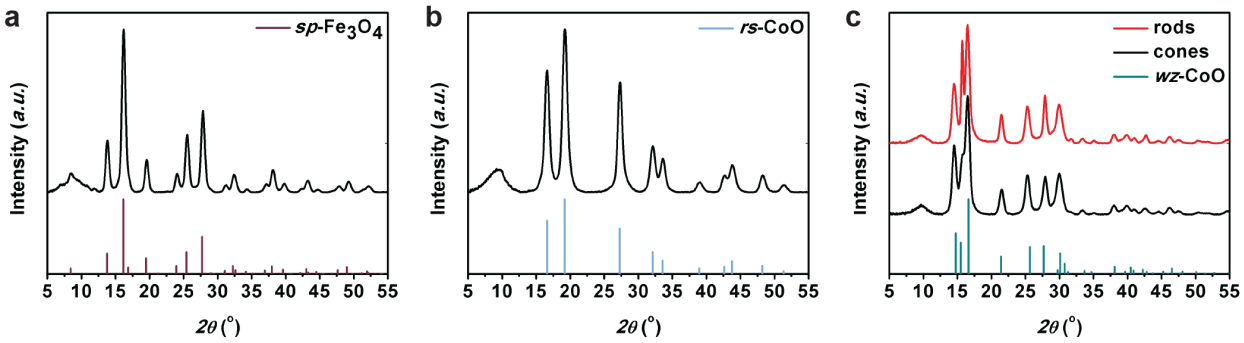


**Figure 3.11.** X-ray diffraction patterns for the (a) $Fe_3O_4$ and (b) *rs*-CoO nanoparticles, as well as the (c) *wz*-CoO cones and rods.

## 3.7 References


1. McCloskey, K. E.; Chalmers, J. J.; Zborowski, M., Magnetic Cell Separation: Characterization of Magnetophoretic Mobility. *Anal. Chem.* **2003,** *75* (24), 6868-6874.

2. Sandu, I.; Cerletti, D.; Claassen, M.; Oxenius, A., Exhausted CD8+ T Cells Exhibit Low and Strongly Inhibited TCR Signaling During Chronic LCMV Infection. *Nat. Commun.* **2020,** *11* (1).

3. Zborowski, M.; Chalmers, J. J., Rare Cell Separation and Analysis by Magnetic Sorting. *Anal. Chem.* **2011,** *83* (21), 8050-8056.

4. Adem, S.; Jain, S.; Sveiven, M.; Zhou, X.; O'Donoghue, A. J.; Hall, D. A., Giant Magnetoresistive Biosensors for Real-Time Quantitative Detection of Protease Activity. *Sci. Rep.* **2020,** *10* (1).

5. Lapitan, L. D. S.; Xu, Y.; Guo, Y.; Zhou, D., Combining Magnetic Nanoparticle Capture and Poly-Enzyme Nanobead Amplification for Ultrasensitive Detection and Discrimination of DNA Single Nucleotide Polymorphisms. *Nanoscale* **2019,** *11* (3), 1195-1204.

6. Cai, Z.; Wu, C.; Yang, L.; Wang, D.; Ai, H., Assembly-Controlled Magnetic Nanoparticle Clusters as MRI Contrast Agents. *ACS Biomater. Sci. Eng.* **2020,** *6* (5), 2533-2542.

7. Graeser, M.; Thieben, F.; Szwargulski, P.; Werner, F.; Gdaniec, N.; Boberg, M.; Griese, F.; Möddel, M.; Ludewig, P.; van de Ven, D.; Weber, O. M.; Woywode, O.; Gleich, B.; Knopp, T., Human-Sized Magnetic Particle Imaging for Brain Applications. *Nat. Commun.* **2019,** *10* (1).

8. Zhou, B. H.; Rinehart, J. D., A Size Threshold for Enhanced Magnetoresistance in Colloidally Prepared $CoFe_2O_4$ Nanoparticle Solids. *ACS Cent. Sci.* **2018,** *4* (9), 1222-1227.

9. Zhou, B. H.; Rinehart, J. D., Pseudo Spin Valve Behavior in Colloidally Prepared Nanoparticle Films. *ACS Appl. Electron. Mater.* **2019,** *1* (7), 1065-1069.

10. Fabris, F.; Lima, E.; Quinteros, C.; Neñer, L.; Granada, M.; Sirena, M.; Zysler, R. D.; Troiani, H. E.; Leborán, V.; Rivadulla, F.; Winkler, E. L., Tunnel Magnetoresistance in Self-Assemblies of Exchange-Coupled Core/Shell Nanoparticles. *Phys. Rev. Appl.* **2019,** *11* (5).

11. Wang, T.; Luan, Z.-Z.; Ge, J.-Y.; Liu, L.; Wu, D.; Lv, Z.-P.; Zuo, J.-L.; Sun, S., Enhancing Low-Field Magnetoresistance in Magnetite Nanoparticles via Zinc Substitution. *Phys. Chem. Chem. Phys.* **2018,** *20* (25), 17245-17252.

12. Bee, A.; Massart, R.; Neveu, S., Synthesis of Very Fine Maghemite Particles. *J. Magn. Magn. Mater.* **1995,** *149* (1-2), 6-9.

13. Chin, A. B.; Yaacob, I. I., Synthesis and Characterization of Magnetic Iron Oxide Nanoparticles via w/o Microemulsion and Massart's Procedure. *J. Mater. Process. Technol.* **2007,** *191* (1-3), 235-237.

14. Park, J.; An, K.; Hwang, Y.; Park, J.-G.; Noh, H.-J.; Kim, J.-Y.; Park, J.-H.; Hwang, N.-M.; Hyeon, T., Ultra-Large-Scale Syntheses of Monodisperse Nanocrystals. *Nat. Mater.* **2004,** *3* (12), 891-895.

15. Sun, S.; Zeng, H.; Robinson, D. B.; Raoux, S.; Rice, P. M.; Wang, S. X.; Li, G., Monodisperse $MFe_2O_4$ (M = Fe, Co, Mn) Nanoparticles. *J. Am. Chem. Soc.* **2003,** *126* (1), 273-279.

16. Wan, J.; Chen, X.; Wang, Z.; Yang, X.; Qian, Y., A Soft-Template-Assisted Hydrothermal Approach to Single-Crystal $Fe_3O_4$ Nanorods. *J. Cryst. Growth* **2005,** *276* (3-4), 571-576.

17. Nedelkoski, Z.; Kepaptsoglou, D.; Lari, L.; Wen, T.; Booth, R. A.; Oberdick, S. D.; Galindo, P. L.; Ramasse, Q. M.; Evans, R. F. L.; Majetich, S.; Lazarov, V. K., Origin of Reduced Magnetization and Domain Formation in Small Magnetite Nanoparticles. *Sci. Rep.* **2017,** *7* (1).

18. Unni, M.; Uhl, A. M.; Savliwala, S.; Savitzky, B. H.; Dhavalikar, R.; Garraud, N.; Arnold, D. P.; Kourkoutis, L. F.; Andrew, J. S.; Rinaldi, C., Thermal Decomposition Synthesis of Iron Oxide Nanoparticles with Diminished Magnetic Dead Layer by Controlled Addition of Oxygen. *ACS Nano* **2017,** *11* (2), 2284-2303.

19. Feld, A.; Weimer, A.; Kornowski, A.; Winckelmans, N.; Merkl, J.-P.; Kloust, H.; Zierold, R.; Schmidtke, C.; Schotten, T.; Riedner, M.; Bals, S.; Weller, H., Chemistry of Shape-Controlled Iron Oxide Nanocrystal Formation. *ACS Nano* **2018,** *13* (1), 152-162.

20. Dong, A.; Ye, X.; Chen, J.; Kang, Y.; Gordon, T.; Kikkawa, J. M.; Murray, C. B., A Generalized Ligand-Exchange Strategy Enabling Sequential Surface Functionalization of Colloidal Nanocrystals. *J. Am. Chem. Soc.* **2010,** *133* (4), 998-1006.

21. Shirmardi Shaghasemi, B.; Dehghani, E. S.; Benetti, E. M.; Reimhult, E., Host–Guest Driven Ligand Replacement on Monodisperse Inorganic Nanoparticles. *Nanoscale* **2017,** *9* (26), 8925-8929.

22. Mitra, A.; Mohapatra, J.; Meena, S. S.; Tomy, C. V.; Aslam, M., Verwey Transition in Ultrasmall-Sized Octahedral $Fe_3O_4$ Nanoparticles. *J. Phys. Chem. C* **2014,** *118* (33), 19356-19362.

23. Qiao, L.; Fu, Z.; Li, J.; Ghosen, J.; Zeng, M.; Stebbins, J.; Prasad, P. N.; Swihart, M. T., Standardizing Size- and Shape-Controlled Synthesis of Monodisperse Magnetite ($Fe_3O_4$) Nanocrystals by Identifying and Exploiting Effects of Organic Impurities. *ACS Nano* **2017,** *11* (6), 6370-6381.

24. Coey, J. M. D., Magnetism and Magnetic Materials. Cambridge University Press: Cambridge, 2010; pp 374-438.

25. Baaziz, W.; Pichon, B. P.; Lefevre, C.; Ulhaq-Bouillet, C.; Greneche, J.-M.; Toumi, M.; Mhiri, T.; Bégin-Colin, S., High Exchange Bias in $Fe_{3-\delta}O4$@CoO Core Shell Nanoparticles Synthesized by a One-Pot Seed-Mediated Growth Method. *J. Phys. Chem. C* **2013,** *117* (21), 11436-11443.

26. Andersson, M. S., Nanoparticle Magnetism: Superspin Glasses. *J. Nanosci. Nanotechnol.* **2019,** *19* (8), 4903-4910.

27. De Toro, J. A.; Lee, S. S.; Salazar, D.; Cheong, J. L.; Normile, P. S.; Muñiz, P.; Riveiro, J. M.; Hillenkamp, M.; Tournus, F.; Tamion, A.; Nordblad, P., A Nanoparticle Replica of the Spin-Glass State. *Appl. Phys. Lett.* **2013,** *102* (18).

28. De Toro, J. A.; Normile, P. S.; Lee, S. S.; Salazar, D.; Cheong, J. L.; Muñiz, P.; Riveiro, J. M.; Hillenkamp, M.; Tournus, F.; Tamion, A.; Nordblad, P., Controlled Close-Packing of Ferrimagnetic Nanoparticles: An Assessment of the Role of Interparticle Superexchange Versus Dipolar Interactions. *J. Phys. Chem. C* **2013,** *117* (19), 10213-10219.

29. Hiroi, K.; Komatsu, K.; Sato, T., Superspin Glass Originating from Dipolar Interaction with Controlled Interparticle Distance Among $\gamma$-$Fe_2O_3$ Nanoparticles with Silica Shells. *Phys. Rev. B* **2011,** *83* (22).

30. Parker, D.; Dupuis, V.; Ladieu, F.; Bouchaud, J. P.; Dubois, E.; Perzynski, R.; Vincent, E., Spin-Glass Behavior in an Interacting $\gamma$-$Fe_2O_3$ Nanoparticle System. *Phys. Rev. B* **2008,** *77* (10).

31. Muscas, G.; Concas, G.; Laureti, S.; Testa, A. M.; Mathieu, R.; De Toro, J. A.; Cannas, C.; Musinu, A.; Novak, M. A.; Sangregorio, C.; Lee, S. S.; Peddis, D., The Interplay Between Single Particle Anisotropy and Interparticle Interactions in Ensembles of Magnetic Nanoparticles. *Phys. Chem. Chem. Phys.* **2018,** *20* (45), 28634-28643.

32. Zhang, Y.; Zhu, J.; Song, X.; Zhong, X., Controlling the Synthesis of CoO Nanocrystals with Various Morphologies. *J. Phys. Chem. C* **2008,** *112* (14), 5322-5327.

33. Roca, A. G.; Golosovsky, I. V.; Winkler, E.; López-Ortega, A.; Estrader, M.; Zysler, R. D.; Baró, M. D.; Nogués, J., Unravelling the Elusive Antiferromagnetic Order in Wurtzite and Zinc Blende CoO Polymorph Nanoparticles. *Small* **2018,** *14* (15).

34. Henne, B.; Ney, V.; de Souza, M.; Ney, A., Exchange-Bias-Like Effect of an Uncompensated Antiferromagnet. *Phys. Rev. B* **2016,** *93* (14).

35. Varón, M.; Beleggia, M.; Kasama, T.; Harrison, R. J.; Dunin-Borkowski, R. E.; Puntes, V. F.; Frandsen, C., Dipolar Magnetism in Ordered and Disordered Low-Dimensional Nanoparticle Assemblies. *Sci. Rep.* **2013,** *3* (1).

36. Yamamoto, K.; Hogg, C. R.; Yamamuro, S.; Hirayama, T.; Majetich, S. A., Dipolar Ferromagnetic Phase Transition in $Fe_3O_4$ Nanoparticle Arrays Observed by Lorentz Microscopy and Electron Holography. *Appl. Phys. Lett.* **2011,** *98* (7).

37. Stoner, E. C.; Wohlfarth, E. P., A Mechanism of Magnetic Hysteresis in Heterogeneous Alloys. *Philos. Trans. R. Soc. A* **1997,** *240* (826), 599-642.

38. Kelly, P. E.; O'Grady, K.; Mayo, P. I.; Chantrell, R. W., Switching Mechanisms in Cobalt-Phosphorus Thin Films. *IEEE Trans. Magn.* **1989,** *25* (5), 3881-3883.

39. Andersson, M. S.; De Toro, J. A.; Lee, S. S.; Mathieu, R.; Nordblad, P., Ageing Dynamics of a Superspin Glass. *EPL* **2014,** *108* (1).

40. Andersson, M. S.; De Toro, J. A.; Lee, S. S.; Normile, P. S.; Nordblad, P.; Mathieu, R., Effects of the Individual Particle Relaxation Time on Superspin Glass Dynamics. *Phys. Rev. B* **2016,** *93* (5).

41. Peddis, D.; Trohidou, K. N.; Vasilakaki, M.; Margaris, G.; Bellusci, M.; Varsano, F.; Hudl, M.; Yaacoub, N.; Fiorani, D.; Nordblad, P.; Mathieu, R., Memory and Superposition in a Superspin Glass. *Sci. Rep.* **2021,** *11* (1).

42. An, K.; Lee, N.; Park, J.; Kim, S. C.; Hwang, Y.; Park, J.-G.; Kim, J.-Y.; Park, J.-H.; Han, M. J.; Yu, J.; Hyeon, T., Synthesis, Characterization, and Self-Assembly of Pencil-Shaped CoO Nanorods. *J. Am. Chem. Soc.* **2006,** *128* (30), 9753-9760.

43. Buck, M. R.; Biacchi, A. J.; Schaak, R. E., Insights into the Thermal Decomposition of Co(II) Oleate for the Shape-Controlled Synthesis of Wurtzite-Type CoO Nanocrystals. *Chem. Mater.* **2014,** *26* (3), 1492-1499.

44. Han, M. J.; Kim, H.-S.; Kim, D. G.; Yu, J., Collinear and Noncollinear Spin Ground State of Wurtzite CoO. *Phys. Rev. B* **2013,** *87* (18).

45. He, X.; Zhong, W.; Yan, S.; Liu, C.; Shi, H.; Au, C.-T.; Du, Y., Transition Temperature of Wurtzite CoO Nanocrystals as Revealed in Comprehensive Magnetic Characterization. *J. Phys. Chem. C* **2014,** *118* (25), 13898-13903.

46. Bronstein, L. M.; Huang, X.; Retrum, J.; Schmucker, A.; Pink, M.; Stein, B. D.; Dragnea, B., Influence of Iron Oleate Complex Structure on Iron Oxide Nanoparticle Formation. *Chem. Mater.* **2007,** *19* (15), 3624-3632.

47. Lynch, J.; Zhuang, J.; Wang, T.; LaMontagne, D.; Wu, H.; Cao, Y. C., Gas-Bubble Effects on the Formation of Colloidal Iron Oxide Nanocrystals. *J. Am. Chem. Soc.* **2011,** *133* (32), 12664-12674.

48. Schneider, C. A.; Rasband, W. S.; Eliceiri, K. W., NIH Image to ImageJ: 25 years of Image Analysis. *Nat. Methods* **2012,** *9* (7), 671-675.

# Chapter 4

# A Size Threshold for Enhanced Magnetoresistance in Colloidally Prepared $CoFe_2O_4$ Nanoparticle Solids

## 4.1 Introduction

Controlling the flow of electrons by switching magnetization was one of the most impactful advancements of the digital revolution. In particular, the discovery of giant magnetoresistance (GMR) led to the first commercial applications of spintronic technology nearly 40 years ago.[1-2] From its initial use in hard drive read-heads, a continuous stream of advances in Giant (GMR), Tunnelling (TMR), Anisotropic (AMR), and other forms of MR have led to smaller, faster, and more sensitive electrical detection. Although reading and writing digital data remains a main driver of MR research, other detection platforms where speed and sensitivity are important have also become prominent. These technologies include navigation,[3-5] biochemical and chemical detection,[6-8] magnetic relaxometry,[9-10] and non-destructive materials testing.[11-13]

One method to improve the sensitivity of an MR-based sensor is to increase the number of magnetic layers traversed by an electron moving through the device. The magnetization of these layers can be either

maximally aligned to enhance the current or anti-aligned to impede it. In commercial devices, this can be done by deposition of multilayer thin-film devices of increasingly complex architecture. Very early on in the development of MR devices, an alternative geometry was proposed wherein small-grain bulk materials would be pressed together or bulk mixtures would be phase-separated into small magnetic domains surrounded by conducting or insulating material.[15-16] Ideally in this geometry, each magnetic grain boundary can be a spin-selecting junction and the total number of junctions is increased by many orders of magnitude. With simple device preparation, minimal materials cost, and low equipment investment, such an architecture could rapidly expand the scope and viability of MR sensing devices. Although early formulations suffered from poor grain boundaries and size distributions, advances in colloidal nanoparticle

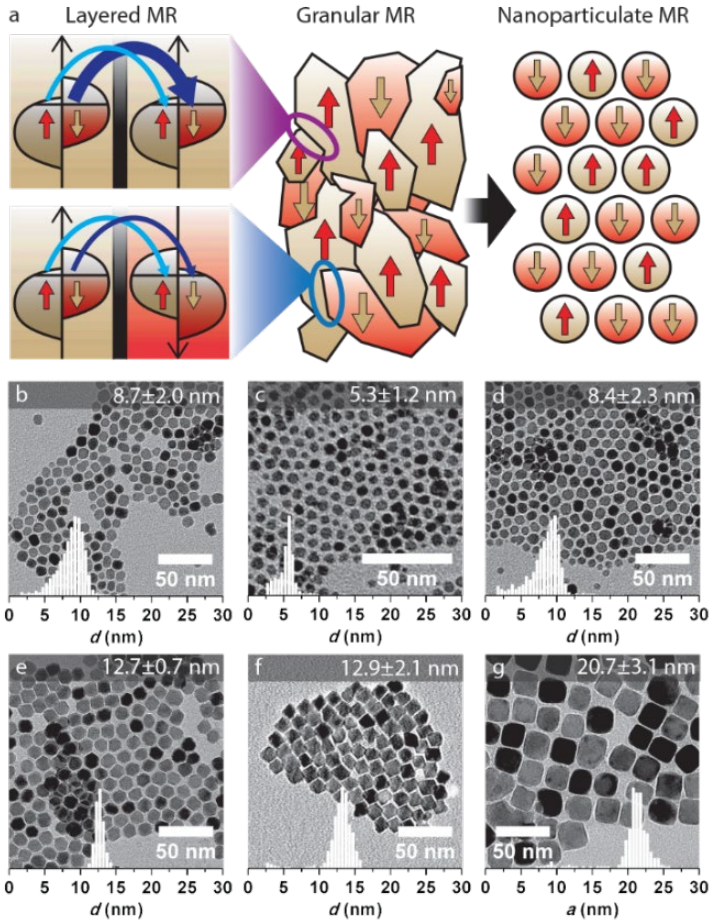


**Figure 4.1.** a) Scheme of the evolution of MR from single-junction thin film devices to multi-junction granular materials to multi-junction nanoparticulate materials with exquisite control over grain properties. Transmission electron micrographs and size distribution histograms of b) $Fe_3O_4$ and c–g) $CoFe_2O_4$ nanoparticles used in this study. The diameter $d$ in b–f) was calculated from the projected area $A$ ($d = \sqrt{4A/\pi}$) while the side length $a$ in g) was calculated as $a = \sqrt{A}$.[14]

synthesis over the past few decades now allow many types of nanoparticles to be chemically synthesized as free-standing particles with tight control over size, morphology, and surface chemistry. This developing synthetic control has led to a re-examining of the viability of granular magnetoresistance via a bottom-up nanochemistry approach.

Overwhelmingly, the most studied material to date is the ferrimagnetic inverse spinel $Fe_3O_4$ (magnetite). Ease of synthesis, stability, strong magnetization and predicted half-metallicity with full spin polarization have all contributed to the prevalence of $Fe_3O_4$ nanoparticle composites as research MR materials. Recent work on granular MR in $Fe_3O_4$ has demonstrated its promise by increasing differential magnetoresistance,

$$\frac{\Delta R}{R} = -\frac{R_H - R_{H_C}}{R_{H_C}} * 100\%, \qquad \textbf{(Equation 4.1)}$$

from 1.2% ($\Delta H$ = 450 mT)[17] to values exceeding 20% at equivalent $\Delta H$.[18] It should be noted that by this definition a perfect magnetoresistor will have $\Delta R/R$ = 100% instead of approaching infinity as in definitions that divide by the lower value of the resistance (Figure 4.5). This empirical evidence suggests that nanostructuring is capable of transforming granular MR from a curiosity into a viable technology; yet, from a synthetic chemistry perspective, only the barest surface of the materials parameter space has been explored.[17-28]

## 4.2 Results and Discussion

### 4.2.1 Synthesis and Processing of the $CoFe_2O_4$ Nanoparticles

Magnetic properties such as coercivity, saturation magnetization, and remnant magnetization are strongly size-dependent in nanomaterials of $d$ = 1–20 nm, yet a study on the MR of well-defined, colloidally prepared materials is lacking from the literature. In this work we perform the first such study using nanoparticles of $CoFe_2O_4$. The greater anisotropy of $CoFe_2O_4$ compared to $Fe_3O_4$ has been used to enhance the MR properties of $Fe_3O_4$ through doping[29] and exchange coupling,[30-31] but the MR of stoichiometric $CoFe_2O_4$ alone has not been studied. Intriguingly, we find that single-domain ferrimagnetism or even

blocked superparamagnetism is unnecessary to observe viable MR at 300 K – the most important factor is nanoparticle size.

Nanoparticles in this work were synthesized according to literature heat-up processes involving the thermal decomposition of Fe(III) and Co(II) acetylacetonate salts in the presence of oleic acid and oleylamine in high boiling point solvents.[32-33] Transmission Electron Microscopy (TEM) statistics were used to verify consistent size and shape for five separate synthetic preparations of $CoFe_2O_4$ ($d$ = 5.3, 8.4, 12.7, 12.9, 20.7 nm) (Figure 4.1b–g) as well as an $Fe_3O_4$ sample ($d$ = 8.7 nm) for comparison. Smaller nanoparticles ($d$ = 5–9 nm) were roughly spherical in shape and larger nanoparticles exhibited some faceting due to growth along preferential crystalline faces. The $d$ = 12.7 nm and $d$ = 12.9 nm samples showed polyhedral shapes while convex cubes are observed for the $d$ = 20.7 nm sample. Of particular note are $d$ = 12.9 nm $CoFe_2O_4$ nanoparticles (Figure 4.1e), which took truncated octahedral forms allowing them to self-assemble into semi-regular lattices. Powder-averaged x-ray diffraction (pXRD) confirmed the inverse spinel crystal structure of $AB_2O_4$ ferrites for all samples (Figure 4.6).

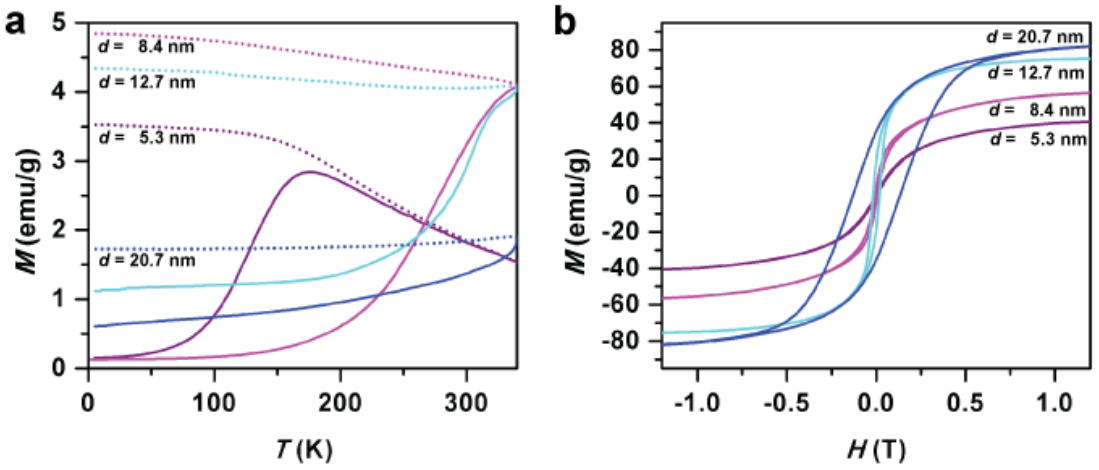


**Figure 4.2.** a) Plots of magnetic moment vs. temperature under zero-field cooled (ZFC, solid lines) and field-cooled (FC, dashed lines) conditions with an applied field of 100 Oe. b) Field dependence of the magnetic moment of $CoFe_2O_4$ nanoparticles measured at 300 K.

As-synthesized nanoparticles form stable colloidal suspensions in non-polar solvents due to the presence of long-chain ligands such as oleic acid and oleylamine. Ligand exchange of the native long-chain ligands to the small inorganic $BF_4^-$ ion was performed according to a literature procedure[34] in order

to improve the conductivity of the final nanoparticle pellets. Although significant work has been done to improve conductivity and even control spin-transport through ligand design,[19-20, 28] in this work we focus on high temperature properties and simply decreasing interparticle distance was sufficient to achieve viable conductivity. The removal of the hydrophobic ligands was evident from the ability to disperse ligand-exchanged nanoparticles in polar solvents such as dimethylformamide. TEM also demonstrates a reduced interparticle spacing in self-assembled layers cast from the $BF_4^-$ exchanged nanoparticles, compared to the TEM of the nanoparticles with their original ligands (Figure 4.7).

### 4.2.2 Magnetic Properties of the $CoFe_2O_4$ Nanoparticles

In the nano-regime, magnetic properties become strongly size-dependent as the particle transitions from multi-domain to single-domain to superparamagnetic behaviour. To characterize the properties of each particle sample, the temperature-dependence of the magnetic moment was examined. Initially, samples were cooled to T = 2 K in the absence of a magnetic field and subsequently subjected to a small field of $H$ = 100 Oe. For samples of all particle diameters, these zero-field-cooled (ZFC) samples are unable to magnetize due to the large thermal barrier to reorienting their magnetic moments. As temperature is raised, the magnetic moment becomes able to freely respond to the external field at its blocking temperature (TB), reaching a magnetic moment equivalent to that of a sample that was cooled under field-cooled (FC) conditions. As expected, $T_B$ is a function of d, with only $CoFe_2O_4$ (d = 5.3 nm) and $Fe_3O_4$ (d = 8.7 nm) becoming unblocked below T = 300 K (Figure 4.2a, Figure 4.9a). To determine the saturation magnetization ($M_S$) and coercive field ($H_C$) of each sample, moment vs. field scans were collected from −7 to 7 Tesla at 300 K. Again, the expected size dependence is observed, with larger particles displaying stronger $H_C$ and higher $M_S$. These results confirm that all samples are within the superparamagnetic regime (Table 4.1).

### 4.2.3 Magnetoresistance Properties of the $CoFe_2O_4$ Nanoparticles

With a structurally and magnetically characterized array of particle sizes, each material then was tested for magnetoresistive properties. For these measurements pressed pellets of each sample were electrically contacted and subjected to a variable magnetic field (Figure 4.3a). At 300 K, $CoFe_2O_4$ ($d$ = 5.3)

was biased under $H = -7$ T and its resistance ($\rho$) was monitored as a function of increasing magnetic field. At large negative fields, the resistance is only weakly dependent on field, yet as $H$ approaches 0 T, the resistance rapidly increases, reaching a maximum value only after reaching $H_C$. Since $CoFe_2O_4$ is an unblocked superparamagnet at 300 K, $H_C = 0$ T. This behavior is consistent with minimal resistance at maximum spin alignment ($M = M_S$) and maximum resistance at minimal spin alignment ($M = 0$; $H = H_C$, Figure 4.8). When field is scanned in the reverse direction (7 T to −7 T), the resistance values are mirrored across the y-axis. When subjected to the maximum magnetic field, $CoFe_2O_4$ ($d$ = 5.3) exhibits $\Delta R/R$ = 19.2%. These results indicate that the MR mechanism at work here does not necessitate ordered magnetism. In fact, since $T_B$ = 175 K for these particles, MR does not even require blocked superparamagnetism. By comparison, $Fe_3O_4$ ($d$ = 8.7 nm) in an equivalent sample and electrode configuration, results in $\Delta R/R$ = 10%, despite significantly higher magnetization values (Figure 4.9b).

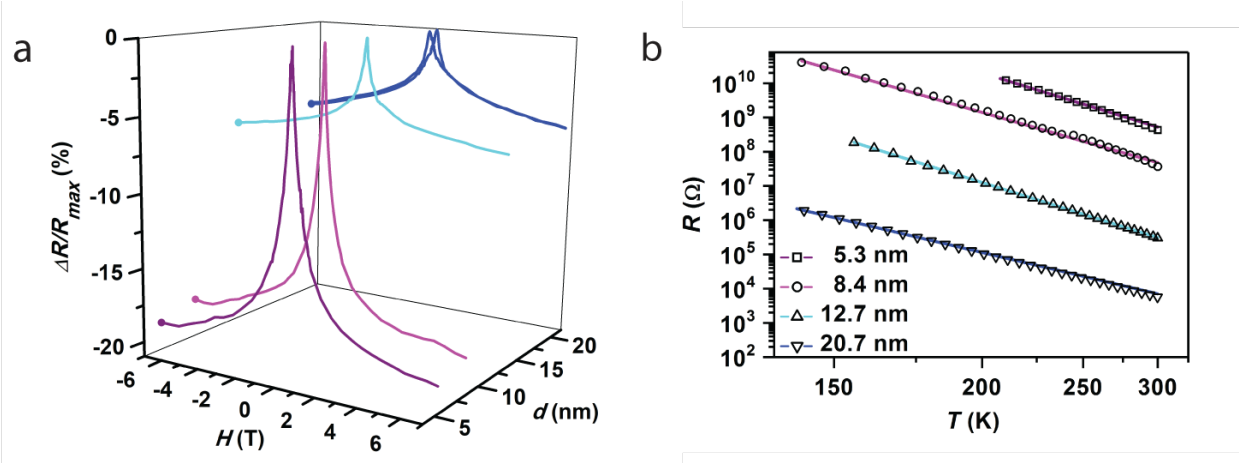


**Figure 4.3.** a) $CoFe_2O_4$ Magnetoresistance at 300 K as a function of magnetic field, $H$, and particle diameter, $d$. The split peaks observed for $d$ = 20.7 nm is a result of magnetic hysteresis (Figure 4.8). b) Temperature-dependent resistance of $CoFe_2O_4$ nanoparticle pellets without an applied magnetic field. Symbols represent measured data points while colored lines are fits based on Equation 4.2.

To study the effect of increasing particle size on the MR, $CoFe_2O_4$ ($d$ = 8.4, 12.7, 20.7 nm) were tested as well. Each sample displays progressively higher $M_S$, $H_C$, and $T_B$ values as expected for superparamagnets with more spin centers, yet a contrasting trend was observed in their MR. $CoFe_2O_4$ ($d$ = 8.4) possesses similar MR ($\Delta R/R$ = 18.4%) to $CoFe_2O_4$ ($d$ = 5.3) despite an enhancement in $M_S$ of over 25%. Surprisingly, this seems to indicate an inherent granular MR value that is inert to size-based effects.

When size is further increased, however, a precipitous drop in MR is observed with $\Delta R/R$ = 6.6 and 6.1% for $CoFe_2O_4$ ($d$ = 12.7 nm) and $CoFe_2O_4$ ($d$ = 20.7 nm), respectively. One possible explanation for this behaviour is that the 5.3 nm and 8.4 nm nanoparticles have significantly lower $H_C$ than the 12.7 nm and 20.7 nm nanoparticles. Coercive granular samples have been predicted to show a decreased magnetoresistance due to decreased ability to break alignment with the anisotropy axis and align with the magnetic field.[35] However, magnetoresistance curves taken at 175 K, where all four nanoparticle samples are blocked, show the same trend in $\Delta R/R$ (Figure 4.10), and it is clear from the $M$ vs. $H$ data that the external field is able to magnetize the sample in all cases. Another possibility is that spin polarization increases as the nanoparticle size decreases. This is consistent with a smaller carrier concentration and shorter distances for electrons to travel between grain interfaces.

### 4.2.4 Temperature Dependent Resistance

Further insight into the charge transport mechanism in these samples can be gleaned from the temperature dependence of the resistance (Figure 4.3b). The zero-field resistance of each $CoFe_2O_4$ sample was measured between 300 K and a lower bound dictated by the instrumentation and sample quality. Within the measured regime, all $CoFe_2O_4$ samples displayed a linear relationship between $lnR$ and $T^{-0.5}$, where $R$ and $T$ are resistance and temperature, respectively. This linear relationship indicates that electrical conductivity occurs via tunnelling of charge carriers between nanoparticles.[35-36] Although exact resistivity values were only obtained for two samples due to sample fragility, the measured resistance values scale similarly due to roughly similar sample geometry. These values follow the trend of larger particles leading to larger resistance per unit length. Resistivity from intergranular tunnelling can be generally described as

$$\rho \propto (1 + P^2 m^2)^{-1} \exp\left(\sqrt{\frac{2\kappa C}{kT}}\right) \qquad \textbf{(Equation 4.2)}$$

where $P$ is the spin polarization, $m$ is the reduced magnetization, $\kappa$ is a tunnelling constant, $C$ is a charging energy, and $k$ is the Boltzmann constant.[35] The $(1 + P^2 m^2)^{-1}$ factor determines the magnetoresistance, while the $\exp(\sqrt{2\kappa C/kT})$ factor determines the overall tunnelling rate. In our samples, the tunnelling rate

should be determined primarily by the charging energy. The tunnelling constant κ depends on barrier height and width, as well as intrinsic material properties, which are invariant across the four $CoFe_2O_4$ samples. However, the charging energy should decrease significantly as the size of the nanoparticles increases, explaining the decreasing resistivity with nanoparticle size observed.

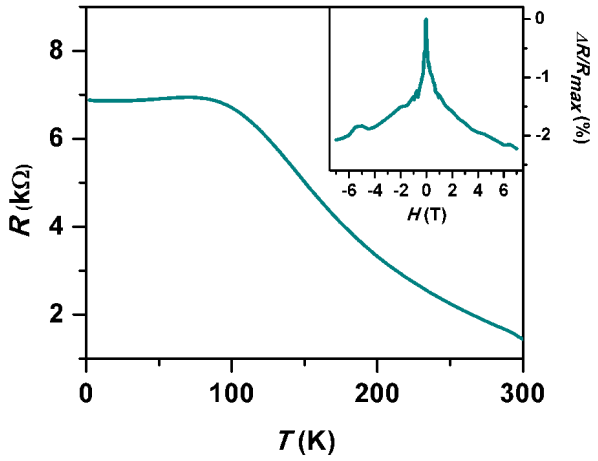


**Figure 4.4.** Temperature dependence of the resistance of octahedrally faceted $d$ = 12.9 nm $CoFe_2O_4$ nanoparticles. (Inset) Room temperature magnetoresistance behavior of the same nanoparticles.

In the course of our study, one sample of $CoFe_2O_4$ ($d$ = 12.9 nm) was discovered to display wholly anomalous MR behavior. Despite size, compositional, and magnetic similarity (Figure 4.11), these particles were synthesized to have an octahedral habit. Temperature dependence of their resistance lacks the characteristic $\ln R \propto T^{-0.5}$ relationship, and the magnitude of the resistance is orders of magnitude lower than that of our other $CoFe_2O_4$ and $Fe_3O_4$ samples. In fact, the temperature dependence shown in Figure 4.4 looks like that of a bulk semiconductor, with an intrinsic region from about 100-300 K and an extrinsic region below 100 K. The greatly decreased resistance of the sample supports the idea that it is behaving as a bulk semiconductor. The truncated octahedral form, lack of bulky ligands, and pressure applied during pellet formation could promote enhanced contact between nanoparticles along matching crystal facets. Fusing of faceted nanoparticles upon ligand removal has been observed in the literature[37-38]. Although discrete particles are still distinguishable by scanning electron microscopy (Figure 4.12), the interfacing of some crystal planes between nanoparticles could provide increased wavefunction overlap between particles,

forming a conductive pathway and eliminating the TMR effect. Charge carriers are able to conduct through this sample similarly to bulk material, rather than by tunnelling between individual nanoparticles. In other applications requiring high conductivity in nanoparticle solids, this mechanism could provide a new materials processing strategy. The decreased $\Delta R/R$ of the 12.9 nm pellet (maximum $\Delta R/R = 2.2\%$) compared to the other $CoFe_2O_4$ samples demonstrates the importance of tunnelling barriers and TMR to strong granular MR.

## 4.3 Conclusions

In this work we have performed the first analysis of the importance of size on the strength of nanoparticle granular MR. Our results demonstrate that the size regime of the particle, more than any specific magnetic parameter, determines the strength of the MR effect. In fact, magnetic ordering or superparamagnetic blocking are not required – thus opening the door to a much wider range of potential MR materials that have remained unexplored. Additionally, it was determined that $CoFe_2O_4$ nanoparticles have comparable or favourable MR values when compared to $Fe_3O_4$. Despite the status of $Fe_3O_4$ as the material of choice in the field, owing to its high predicted spin polarization, the ($d$ = 8.4 nm) $CoFe_2O_4$ nanoparticles showed a higher room temperature maximum $\Delta R/R$ of 18.4%, compared to 10.8% for similarly sized $Fe_3O_4$. These data help demonstrate the value of colloidal synthesis to this field, allowing for wide-ranging and inexpensive exploration of materials with well-defined composition and size in a way that is not possible by traditional top-down methods. Although the methods employed here lack the atomic precision of traditional multilayer thin films, the sheer number of junctions drastically enhances the chances of an observable effect. This both allows for simple screening conditions and suggests that optimization of promising materials could result in drastic improvements.

## 4.4 Experimental

### 4.4.1 Materials

The nanoparticle synthesis reagents used were cobalt(II) acetylacetonate (99%, Acros), iron(III) acetylacetonate (99.9%, Sigma Aldrich), 1,2-hexadecanediol (90%, Sigma Aldrich), oleic acid (90%, Alfa Aesar), oleylamine (70%, Sigma Aldrich), phenyl ether (99%, Sigma Aldrich), and benzyl ether (≥98%, Sigma Aldrich). Nitrosonium tetrafluoroborate ($NOBF_4$, 98%) was purchased from Alfa Aesar. Silver epoxy (Epo-Tek H20E), HPLC grade dichloromethane (DCM), and ACS grade acetone, hexane, ethanol, and toluene were purchased from Fisher. ACS grade Dimethyl formamide (DMF) was purchased from EMD Millipore. All chemicals were used as received.

### 4.4.2 Safety Considerations

Standard laboratory safety protocols were followed in the performance of all procedures described herein. No unexpected hazards were encountered.

### 4.4.3 Synthesis of 8.7 nm $Fe_3O_4$ and 5.3 and 8.4 nm $CoFe_2O_4$ Nanoparticles

$CoFe_2O_4$ nanoparticles ($d$ = 5.3, 8.4 nm) were produced according to Sun *et al.*[32] by thermal decomposition of $M(acac)_x$ (2 mmol) with 1,2-hexadecanediol (10 mmol), oleic acid (6 mmol), and oleylamine (6 mmol) in phenyl ether (10 mL, d = 5.3 nm) or benzyl ether (10 mL, 8.4 nm), where $M(acac)_x$ refers to a 1:2 mixture of $Co(acac)_2$ and $Fe(acac)_3$. The mixture was placed in a 100 mL 3-neck round bottom flask with magnetic stirring and degassed under vacuum at 120°C for 1 h. Under a dinitrogen atmosphere, the mixture was then heated to 200°C and held for 2 h. Subsequently, the mixture was heated to reflux for 1 h, then cooled back to room temperature. The nanoparticles were precipitated with ethanol and centrifugation, then redispersed in hexane. After another cycle of precipitation with ethanol and centrifugation, the nanoparticles were stored in hexane. $Fe_3O_4$ nanoparticles ($d$ = 8.7 nm) were produced similarly to the $CoFe_2O_4$ nanoparticles ($d$ = 8.4 nm), but with $Fe(acac)_3$ (2 mmol) rather than $M(acac)_x$.

### 4.4.4 Synthesis of Octahedral 12.9 nm $CoFe_2O_4$ Nanoparticles

Octahedral $CoFe_2O_4$ nanoparticles ($d$ = 12.9 nm) were synthesized by seeding with $CoFe_2O_4$ (80 mg, $d$ = 8.4 nm) in hexane (4 mL) added to $M(acac)_x$ (2 mmol), 1,2-hexadecanediol (10 mmol), oleic acid (2 mmol), oleylamine (2 mmol), and benzyl ether (10 mL). This reaction mixture was degassed under vacuum at 120°C, heated to 200°C for 1 hr under dinitrogen atmosphere, and heated to reflux for 0.5 h, then cooled to room temperature. The nanoparticles were precipitated with ethanol and centrifugation, then redispersed in hexane. After another cycle of precipitation with ethanol and centrifugation, the nanoparticles were stored in hexane.

### 4.4.5 Synthesis of 12.7 and 20.7 nm $CoFe_2O_4$ Nanoparticles

$CoFe_2O_4$ nanoparticles ($d$ = 12.7, 20.7 nm) were produced according to Yu et al.[33] by thermal decomposition of $M(acac)_x$ (2 mmol) in the presence of oleic acid (12.6 mmol) and oleylamine (12.2 mmol) for 12.7 nm nanoparticles, or oleic acid (18.9 mmol) and oleylamine (18.3 mmol) for 20.7 nm nanoparticles, in benzyl ether (20 mL). The reaction mixture was placed in a 100 mL 3-neck round bottom flask with a magnetic stir bar and degassed by vigorously bubbling dinitrogen through a needle whose tip was placed at the bottom of the flask, while heating at 120°C for 1 h. Following the degassing step, the needle was pulled out so that its tip was above the reaction mixture, and the flow rate of dinitrogen was slowed to a few bubbles per second viewed through an attached oil bubbler. The mixture was heated to 200°C at 5°C/min and held for 2 h, then heated to 290°C at 2°C/min and held for another 2 h before cooling back to room temperature. The nanoparticles were precipitated with ethanol and centrifugation, then redispersed in hexane. After another cycle of precipitation with ethanol and centrifugation, the nanoparticles were stored in hexane.

### 4.4.6 Ligand Exchange of Nanoparticles

The native oleic acid and oleylamine ligands of the nanoparticles were exchanged for the $BF_4^-$ anion according to literature procedure.[34] In a typical procedure, about 2 mL of nanoparticles dispersed in hexane were mixed with about 4 mL of a saturated solution of $NOBF_4$ in DCM, then shaken until

flocculation was observed (typically within a minute). The nanoparticles were then collected with a magnet and the supernatant was discarded. The nanoparticles were redispersed in DMF, then washed by reprecipitating with toluene. After another DMF/toluene washing procedure, the nanoparticles were stored as a DMF suspension.

### 4.4.7 Preparation of Pellets for Magnetoelectric Characterization

Nanoparticle powders were precipitated from colloidal suspensions in DMF by addition of toluene and collected with a magnet. The powders were then dried in a vacuum oven at 60°C. The dry powders were pressed in either a 4 mm (~800 MPa) or 5 mm (~1000 MPa) pellet die for several hours. Gold wires were then contacted to the surface of each pellet with silver epoxy in either a two-wire (for high R samples) or four-wire (low R samples) configuration. The epoxy was cured to improve electrical contact (150°C, 5 min). Finally, the pellets were mounted on printed circuit board sample holders and connected via Duratool 20M4922 solder (60:40 Sn:Pb alloy, rosin activated flux).

### 4.4.8 Characterization

Transmission electron microscopy (TEM) was performed with an FEI Spirit TEM operating at 120kV, with images collected by a 2k x 2k Gatan CCD camera. Samples were prepared by air-drying a dilute hexane solution of nanoparticles on carbon-coated copper grids. Magnetic and magnetoelectric measurements were performed using a Quantum Design MPMS3 SQUID Magnetometer equipped with an Electrical Transport Option. Powder X-ray diffraction was performed on a Bruker Diffractometer with a Mo Kα radiation source and an Apex II Area Detector.

## 4.5 Acknowledgements

This research was funded through the Office of Naval Research Young Investigator Award N00014-16-1-2917. This work was performed in part at the San Diego Nanotechnology Infrastructure (SDNI) of UCSD, a member of the National Nanotechnology Coordinated Infrastructure, which is supported by the National Science Foundation (Grant ECCS-1542148). We also thank Dr. Milan Gembicky

for his assistance with powder X-ray diffraction measurements. J. D. R. would like to express deep gratitude for the enthusiasm, inspiration, and wisdom of Prof. Ami E. Berkowitz.

Chapter 4 is a reformatted reprint from the manuscript entitled “A Size Threshold for Enhanced Magnetoresistance in Colloidally Prepared $CoFe_2O_4$ Nanoparticle Solids” by Zhou, B.H. and Rinehart, J.D. The dissertation author was the primary researcher and author of this paper. Reprinted with permission from *ACS Cent. Sci.* **2018**, *4*,1222–1227. 

## 4.6 Additional Figures

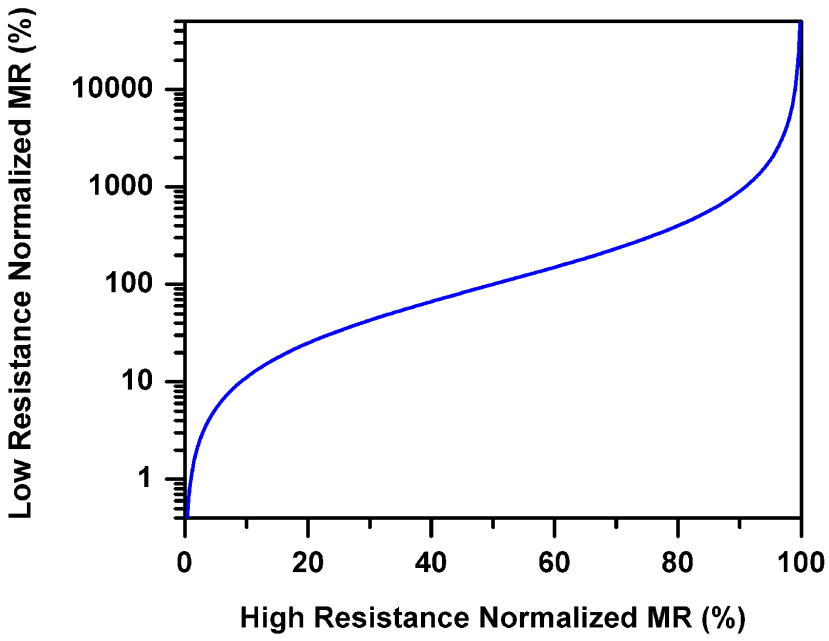


**Figure 4.5.** Differential resistance scaled to the highest resistance value (High Resistance Normalized MR ($\Delta R/R = (R_L - R_H)/R_H$)) vs. differential resistance scaled to the lowest resistance value (Low Resistance Normalized MR ($\Delta R/R = (R_H - R_L)/R_L$)), demonstrating the relationship between the two definitions.

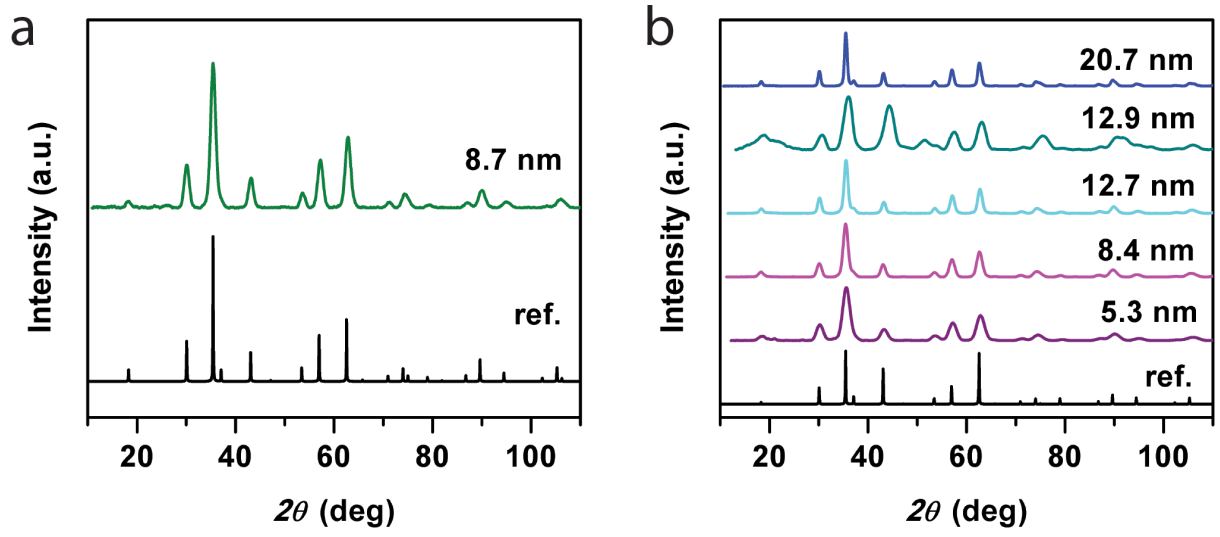


**Figure 4.6.** Powder X-ray diffraction patterns of a) $Fe_3O_4$ and b) $CoFe_2O_4$ nanoparticles, demonstrating their inverse spinel structure.

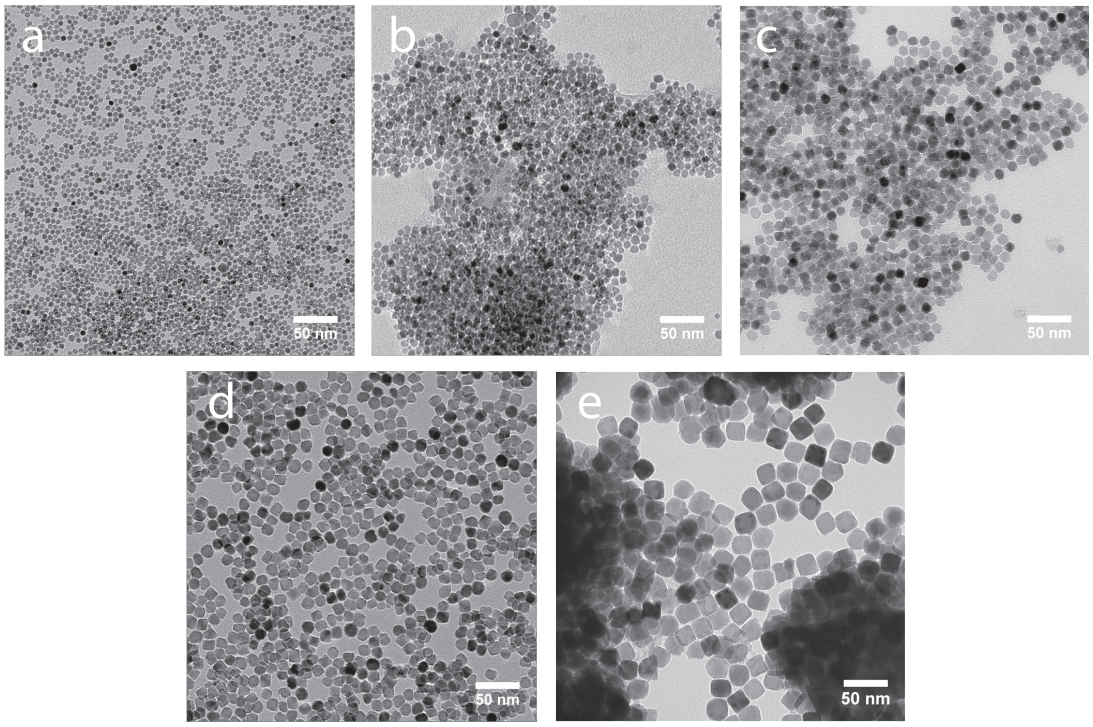


**Figure 4.7.** Transmission electron micrographs of a) $d = 5.3$ nm, b) $d = 8.4$ nm, c) $d = 12.7$ nm, d) $d = 12.9$ nm, and e) $d = 20.7$ nm $CoFe_2O_4$ nanoparticles after $BF_4^-$ ligand exchange.

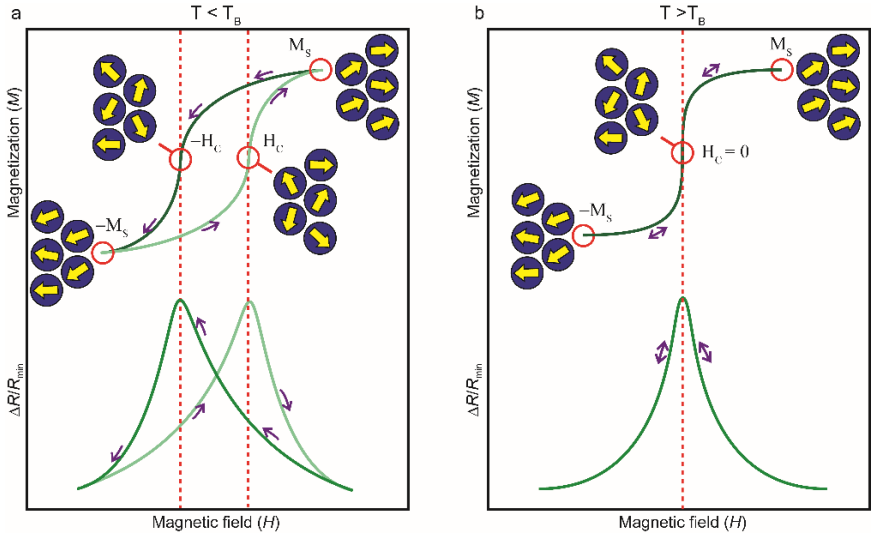


**Figure 4.8.** Overview of the relationship between magnetization vs. field and magnetoresistance vs. field for superparamagnetic samples (a) below and (b) above their blocking temperatures ($T_B$). At points $M_S$ and $-M_S$ (magnetic saturation) the spins are maximally aligned and resistance is minimized. At points $H_C$ and $-H_C$, (coercive field, $M = 0$) the spins are randomly oriented and resistance is maximized.

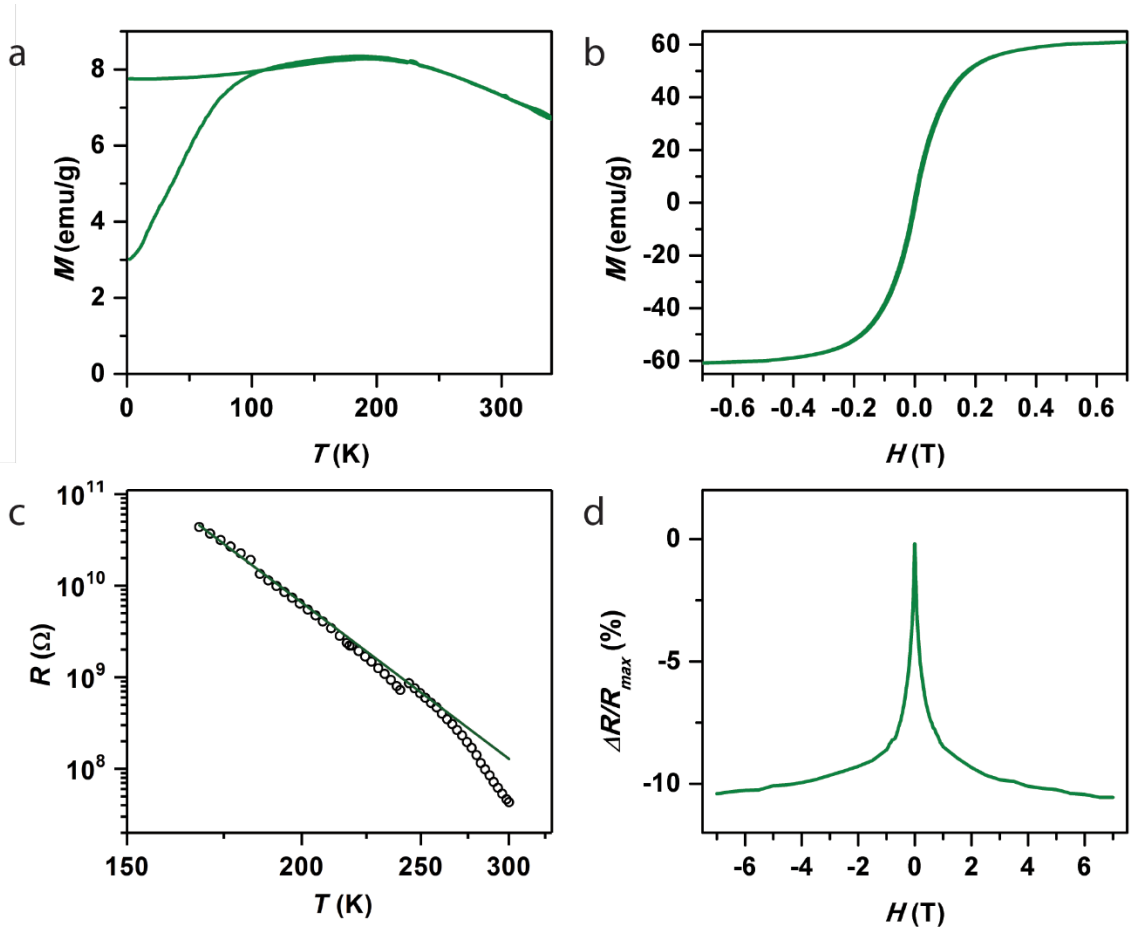


**Figure 4.9.** Summary of magnetic and magnetoresistance data for $d$ = 8.7 nm $Fe_3O_4$ nanoparticles. a) Magnetic moment vs temperature at 100 Oe under ZFC and FC conditions. b) Field dependence of the magnetic moment at 300 K. c) Temperature dependent zero-field resistance. The linear ln($R$) vs. $T^{-0.5}$ behavior is indicative of an intergranular tunneling mechanism. The discontinuity at $T$ = 240 K is due to a changeover in the measurement parameters necessitated by the large resistance values. d) Room temperature magnetoresistance behavior of $d$ = 8.7 nm $Fe_3O_4$ nanoparticles.

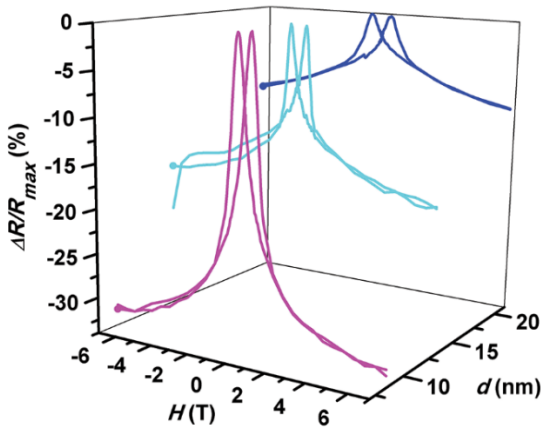


**Figure 4.10.** Magnetoresistance curves for $CoFe_2O_4$ nanoparticles (d = 8.4-20.7 nm) at 175 K. Low temperature data could not be obtained for the $CoFe_2O_4$ ($d$ = 5.3 nm) sample because its resistance at 175 K was greater than the instrument limits.

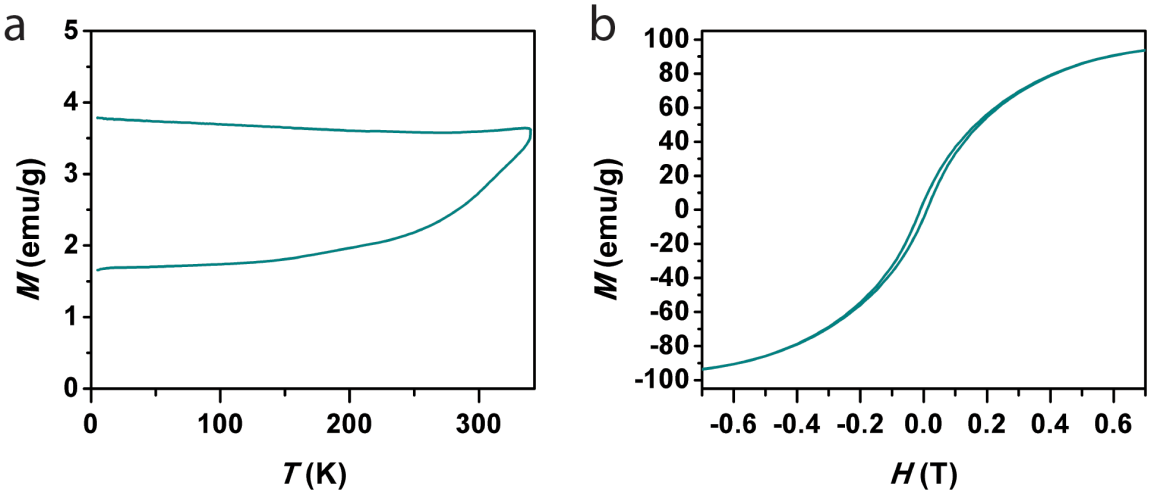


**Figure 4.11.** a) Magnetic moment vs. temperature under ZFC and FC conditions at 100 Oe. b) Field dependence of the magnetic moment of the truncated octahedral $CoFe_2O_4$ nanoparticles ($d$ = 12.9 nm) at 300 K.

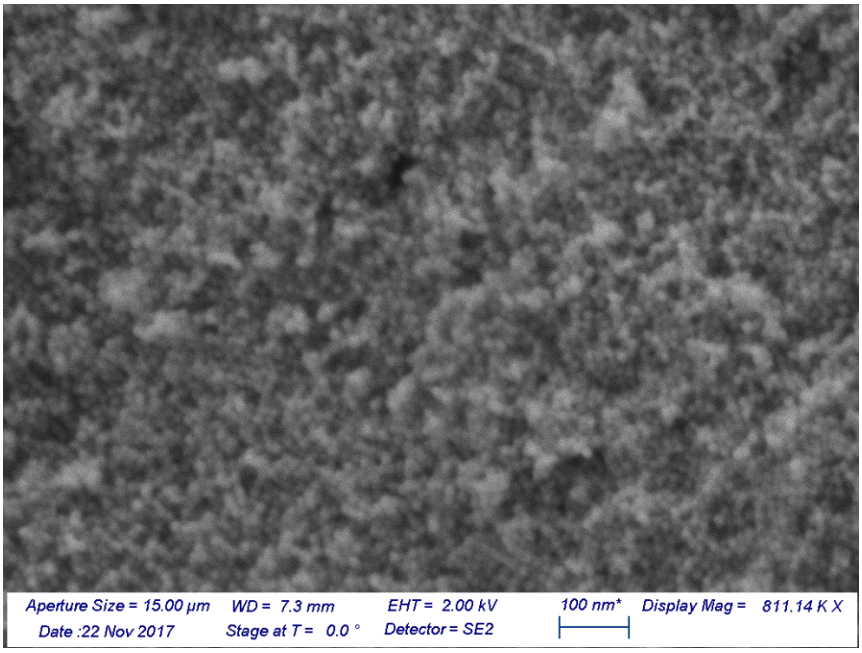


**Figure 4.12.** Scanning electron micrograph of the truncated octahedral 12.9 nm $CoFe_2O_4$ pellet.

**Table 4.1.** Summary of magnetic parameters for each nanoparticle sample

| Nanoparticle Type | $T_B^*$ | $H_C$ (300 K) | $M_R$ (300 K)** | $M_S$ (300 K) | ΔR/R (300 K, 7 T) |
|---|---|---|---|---|---|
| $Fe_3O_4$ ($d$ = 8.7 nm) | 187 K | 0 mT | 0 emu/g | 65 emu/g | 10.40% |
| $CoFe_2O_4$ ($d$ = 5.3 nm) | 175 K | 0 mT | 0 emu/g | 46 emu/g | 19.15% |
| $CoFe_2O_4$ ($d$ = 8.4 nm) | >340 K | 8 mT | 4 emu/g | 62 emu/g | 18.41% |
| $CoFe_2O_4$ ($d$ = 12.7 nm) | >340 K | 19 mT | 19 emu/g | 78 emu/g | 6.61% |
| $CoFe_2O_4$ ($d$ = 12.9 nm) | >340 K | 10 mT | 5 emu/g | 103 emu/g | 2.23% |
| $CoFe_2O_4$ ($d$ = 20.7 nm) | >340 K | 137 mT | 35 emu/g | 90 emu/g | 6.14% |

* Estimated from the peak in the zero-field cooled magnetization curve.

** $M_R$ is the remanent magnetization (magnetic moment at $H$ = 0 T).

## 4.7 References


1. Baibich, M. N.; Broto, J. M.; Fert, A.; Vandau, F. N.; Petroff, F.; Eitenne, P.; Creuzet, G.; Friederich, A.; Chazelas, J., Giant Magnetoresistance of (001)Fe/(001)Cr Magnetic Superlattices. *Phys. Rev. Lett.* **1988,** *61* (21), 2472-2475.

2. Binasch, G.; Grunberg, P.; Saurenbach, F.; Zinn, W., Enhanced Magnetoresistance in Layered Magnetic-Structures with Antiferromagnetic Interlayer Exchange. *Phys. Rev. B* **1989,** *39* (7), 4828-4830.

3. Pannetier-Lecoeur, M.; Fermon, C.; de Vismes, A.; Kerr, E.; Vieux-Rochaz, L., Low Noise Magnetoresistive Sensors for Current Measurement and Compasses. *J. Magn. Magn. Mater.* **2007,** *316* (2), e246-e248.

4. Michelena, M. D.; Oelschlägel, W.; Arruego, I.; del Real, R. P.; Mateos, J. A. D.; Merayo, J. M., Magnetic Giant Magnetoresistance Commercial off the Shelf for Space Applications. *J. Appl. Phys.* **2008,** *103* (7), 07e912.

5. Chiang, C.-Y.; Jeng, J.-T.; Lai, B.-L.; Luong, V. S.; Lu, C.-C., Tri-Axis Magnetometer with In-Plane Giant Magnetoresistance Sensors for Compass Application. *J. Appl. Phys.* **2015,** *117* (17), 17a321.

6. Issadore, D.; Park, Y. I.; Shao, H.; Min, C.; Lee, K.; Liong, M.; Weissleder, R.; Lee, H., Magnetic Sensing Technology for Molecular Analyses. *Lab Chip* **2014,** *14* (14), 2385-2397.

7. Martins, V. C.; Cardoso, F. A.; Germano, J.; Cardoso, S.; Sousa, L.; Piedade, M.; Freitas, P. P.; Fonseca, L. P., Femtomolar Limit of Detection with a Magnetoresistive Biochip. *Biosens. Bioelectron.* **2009,** *24* (8), 2690-2695.

8. Gaster, R. S.; Xu, L.; Han, S.-J.; Wilson, R. J.; Hall, D. A.; Osterfeld, S. J.; Yu, H.; Wang, S. X., Quantification of Protein Interactions and Solution Transport Using High-Density GMR Sensor Arrays. *Nat. Nanotechnol.* **2011,** *6* (5), 314-320.

9. Huang, C. C.; Zhou, X.; Hall, D. A., Giant Magnetoresistive Biosensors for Time-Domain Magnetorelaxometry: A Theoretical Investigation and Progress Toward an Immunoassay. *Sci. Rep.* **2017,** *7*, 45493.

10. Lange, J.; Kotitz, R.; Haller, A.; Trahms, L.; Semmler, W.; Weitschies, W., Magnetorelaxometry - a New Binding Specific Detection Method Based on Magnetic Nanoparticles. *J. Magn. Magn. Mater.* **2002,** *252* (1-3), 381-383.

11. Dogaru, T.; Smith, S. T., Giant Magnetoresistance-Based Eddy-Current Sensor. *IEEE Trans. Magn.* **2001,** *37* (5), 3831-3838.

12. Pelkner, M.; Neubauer, A.; Reimund, V.; Kreutzbruck, M.; Schütze, A., Routes for GMR-Sensor Design in Non-Destructive Testing. *Sensors* **2012,** *12* (9), 12169-12183.

13. Sahoo, D. R.; Sebastian, A.; Häberle, W.; Pozidis, H.; Eleftheriou, E., Scanning Probe Microscopy Based on Magnetoresistive Sensing. *Nanotechnol.* **2011,** *22* (14), 145501.

14. Schneider, C. A.; Rasband, W. S.; Eliceiri, K. W., NIH Image to ImageJ: 25 Years of Image Analysis. *Nat. Methods* **2012,** *9* (7), 671-675.

15. Berkowitz, A. E.; Mitchell, J. R.; Carey, M. J.; Young, A. P.; Zhang, S.; Spada, F. E.; Parker, F. T.; Hutten, A.; Thomas, G., Giant Magnetoresistance in Heterogeneous Cu-Co Alloys. *Phys. Rev. Lett.* **1992,** *68* (25), 3745-3748.

16. Xiao, J. Q.; Jiang, J. S.; Chien, C. L., Giant Magnetoresistance in Nonmultilayer Magnetic Systems. *Phys. Rev. Lett.* **1992,** *68* (25), 3749-3752.

17. Coey, J. M. D.; Berkowitz, A. E.; Balcells, L.; Putris, F. F.; Parker, F. T., Magnetoresistance of Magnetite. *Appl. Phys. Lett.* **1998,** *72* (6), 734-736.

18. Mitra, A.; Barick, B.; Mohapatra, J.; Sharma, H.; Meena, S. S.; Aslam, M., Large Tunneling Magnetoresistance in Octahedral $Fe_3O_4$ Nanoparticles. *AIP Adv.* **2016,** *6* (5), 055007.

19. Lv, Z. P.; Luan, Z. Z.; Cai, P. Y.; Wang, T.; Li, C. H.; Wu, D.; Zuo, J. L.; Sun, S. H., Enhancing Magnetoresistance in Tetrathiafulvalene Carboxylate Modified Iron Oxide Nanoparticle Assemblies. *Nanoscale* **2016,** *8* (24), 12128-12133.

20. Lv, Z. P.; Luan, Z. Z.; Wang, H. Y.; Liu, S.; Li, C. H.; Wu, D.; Zuo, J. L.; Sun, S. H., Tuning Electron-Conduction and Spin Transport in Magnetic Iron Oxide Nanoparticle Assemblies via Tetrathiafulvalene-Fused Ligands. *ACS Nano* **2015,** *9* (12), 12205-12213.

21. Wang, S.; Yue, F. J.; Wu, D.; Zhang, F. M.; Zhong, W.; Du, Y. W., Enhanced Magnetoresistance in Self-Assembled Monolayer of Oleic Acid Molecules on $Fe_3O_4$ Nanoparticles. *Appl. Phys. Lett.* **2009,** *94* (1), 012507.

22. Wang, W.; Yu, M.; Batzill, M.; He, J.; Diebold, U.; Tang, J., Enhanced Tunneling Magnetoresistance and High-Spin Polarization at Room Temperature in a Polystyrene-Coated $Fe_3O_4$ Granular System. *Phys. Rev. B* **2006,** *73* (13), 134412.

23. Liu, K.; Zhao, L.; Klavins, P.; Osterloh, F. E.; Hiramatsu, H., Extrinsic Magnetoresistance in Magnetite Nanoparticles. *J. Appl. Phys.* **2003,** *93* (10), 7951-7953.

24. Kohiki, S.; Kinoshita, T.; Nara, K.; Akiyama-Hasegawa, K.; Mitome, M., Large, Negative Magnetoresistance in an Oleic Acid-Coated $Fe_3O_4$ Nanocrystal Self-Assembled Film. *ACS Appl. Mater. Interfaces* **2013,** *5* (22), 11584-9.

25. Kohiki, S.; Okada, K.; Mitome, M.; Kohno, A.; Kinoshita, T.; Iyama, K.; Tsunawaki, F.; Deguchi, H., Magnetic and Magnetoelectric Properties of Self-Assembled $Fe_{2.5}Mn_{0.5}O_4$ Nanocrystals. *ACS Appl. Mater. Interfaces* **2011,** *3* (9), 3589-93.

26. Poddar, P.; Fried, T.; Markovich, G., First-Order Metal-Insulator Transition and Spin-Polarized Tunneling in $Fe_3O_4$ Nanocrystals. *Phys. Rev. B* **2002,** *65* (17), 172405.

27. Zeng, H.; Black, C. T.; Sandstrom, R. L.; Rice, P. M.; Murray, C. B.; Sun, S., Magnetotransport of Magnetite Nanoparticle Arrays. *Phys. Rev. B* **2006,** *73* (2), 020402.

28. Lv, Z.-P.; Wang, T.; Ge, J.-Y.; Luan, Z.-Z.; Wu, D.; Zuo, J.-L.; Sun, S., Controlling the Assembly and Spin Transport of Tetrathiafulvalene Carboxylate Coated Iron Oxide Nanoparticles. *J. Mater. Chem. C* **2017,** *5* (29), 7200-7206.

29. Kohiki, S.; Nara, K.; Mitome, M.; Tsuya, D., Magnetoresistance of Drop-Cast Film of Cobalt-Substituted Magnetite Nanocrystals. *ACS Appl. Mater. Interfaces* **2014,** *6* (20), 17410-17415.

30. Chen, J.; Ye, X.; Oh, S. J.; Kikkawa, J. M.; Kagan, C. R.; Murray, C. B., Bistable Magnetoresistance Switching in Exchange-Coupled $CoFe_2O_4$-$Fe_3O_4$ Binary Nanocrystal Superlattices by Self-Assembly and Thermal Annealing. *ACS Nano* **2013,** *7* (2), 1478-86.

31. Anil Kumar, P.; Ray, S.; Chakraverty, S.; Sarma, D. D., Engineered Spin-Valve Type Magnetoresistance in $Fe_3O_4$-$CoFe_2O_4$ Core-Shell Nanoparticles. *Appl. Phys. Lett.* **2013,** *103* (10), 102406.

32. Sun, S.; Zeng, H.; Robinson, D. B.; Raoux, S.; Rice, P. M.; Wang, S. X.; Li, G., Monodisperse $MFe_2O_4$ (M = Fe, Co, Mn) Nanoparticles. *J. Am. Chem. Soc.* **2004,** *126* (1), 273-9.

33. Yu, Y.; Mendoza-Garcia, A.; Ning, B.; Sun, S., Cobalt-Substituted Magnetite Nanoparticles and Their Assembly into Ferrimagnetic Nanoparticle Arrays. *Adv. Mater.* **2013,** *25* (22), 3090-3094.

34. Dong, A.; Ye, X.; Chen, J.; Kang, Y.; Gordon, T.; Kikkawa, J. M.; Murray, C. B., A Generalized Ligand-Exchange Strategy Enabling Sequential Surface Functionalization of Colloidal Nanocrystals. *J. Am. Chem. Soc.* **2011,** *133* (4), 998-1006.

35. Inoue, J.; Maekawa, S., Theory of Tunneling Magnetoresistance in Granular Magnetic Films. *Phys. Rev. B* **1996,** *53* (18), R11927-R11929.

36. Zabet-Khosousi, A.; Dhirani, A. A., Charge Transport in Nanoparticle Assemblies. *Chem. Rev.* **2008,** *108* (10), 4072-4124.

37. Robinson, E. H.; Turo, M. J.; Macdonald, J. E., Controlled Surface Chemistry for the Directed Attachment of Copper(I) Sulfide Nanocrystals. *Chem. Mater.* **2017,** *29* (9), 3854-3857.

38. Gupta, S.; Wu, W.-Y.; Chakrabortty, S.; Li, M.; Wang, Y.; Ong, X.; Chan, Y., Hierarchical Multicomponent Nanoheterostructures via Facet-to-Facet Attachment of Anisotropic Semiconductor Nanoparticles. *Chem. Mater.* **2017,** *29* (21), 9075-9083.

# Chapter 5

# Pseudo Spin Valve Behavior in Colloidally Prepared Nanoparticle Films

## 5.1 Introduction

Soon after the revolutionary discovery of giant magnetoresistance (GMR) in multilayered structures,[1-2] an analogous effect was observed for magnetic grains in conducting or insulating matrices.[3-7] In this formulation, the matrix material acts as the spin-selecting junction between magnetically-oriented grains, and the lack of structural precision is compensated by the sheer number of junctions. This alternative realization of magnetoresistance offers the tantalizing prospect of tunable, versatile functionality from a single-layer deposition. Advances in colloidal nanosynthesis and characterization have largely shifted research from milled and biphasic solid-state materials to nanoparticle solids. These materials have led to increasing magnetoresistance ratios ($\Delta R/R_{max}$) and an emerging understanding of how particle composition[8-10], size[11], shape[12], and surface chemistry[13-17] modulate the tunneling magnetoresistance (TMR) that arises from intrinsic tunnel barriers between individual particles.

Continuing exploration in materials composition and device formulation promise large improvements in the properties of these nanocomposite magnetoresistors, yet the fundamental structure that enabled magnetoresistance to occupy a central role in technology for the last 25 years is still missing: *the*

*spin valve*.[18-19] A spin valve pins the moment of one magnetic component of the magnetoresistor (the fixed or hard layer) using exchange bias or intrinsic anisotropy (the latter mechanism is sometimes referred to as a pseudo-spin valve). Pinning the fixed layer allows very small magnetic fields to flip the orientation of the other component (the free or soft layer), leading to highly sensitive step function responses in resistance. Conversely, in a granular or nanocomposite magnetoresistor, application of an external magnetic field results in individual particle moments deviating from their original alignment with the local anisotropy axes ($\Delta R/R_{max}$; Figure 5.1a–ii,iv) towards parallel alignment with the external field axis (minimum $\Delta R/R$; Figure

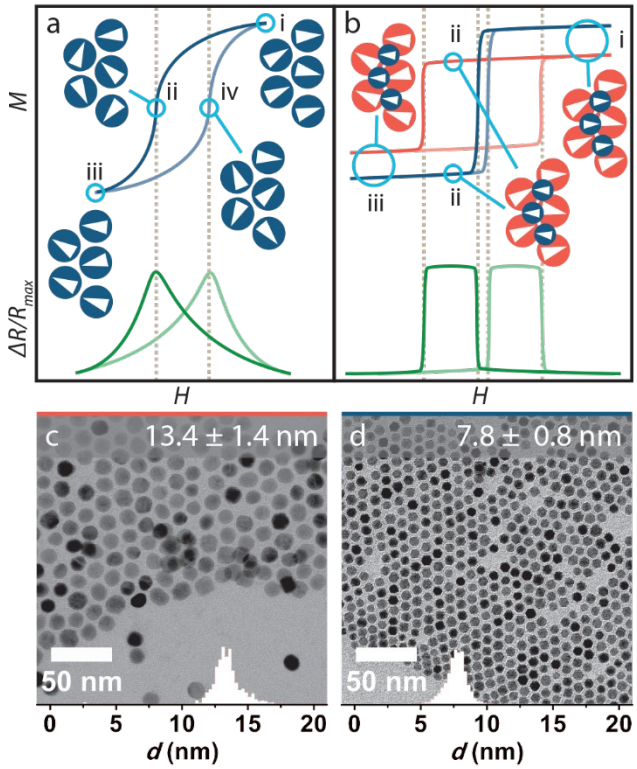


**Figure 5.1.** The relationship between the micromagnetic state and magnetoresistance of a) single component and b) multi-component nanogranular materials. Magnetization vectors of nanoparticles within the granular material are indicated by arrowheads in blue (high coercivity material) and orange (low coercivity material) circles. In b) the orange and blue hysteresis curves depict the independent magnetic switching behavior of high and low coercivity components of the material, respectively, leading to a pseudo spin valve magnetoresistance behavior. Diagrams indicate magnetic saturation, (low resistance; i, iii) and coercive field points (maximum resistance; ii, iv). Below are transmission electron micrographs (TEM) and size histograms of c) $CoFe_2O_4$ and d) $Fe_3O_4$ nanoparticles.

5.1a–i,iii). While the shift in $\Delta R/R_{max}$ can be large, its sensitivity with respect to applied field is severely limited due to switching between an ordered and disordered micromagnetic structure.

To achieve spin valve behavior in a nanocomposite magnetoresistor, we envisioned a monolithic structure composed of hard and soft magnetic nanoparticles. (Figure 5.1b) While there have been reports of multi-component nanoparticle MR materials, they either do not consist of hard and soft magnetic nanoparticles,[20] or involve magnetically coupled components.[21-22] In this work, we produce a series of nanocomposite films from high coercivity $CoFe_2O_4$ and low coercivity $Fe_3O_4$ nanoparticles. By limiting magnetic coupling between the materials, we are able to generate the first example of any form of nanocomposite spin valve magnetoresistance. Excitingly, these devices display magnetoresistive behavior that is both predictable from the magnetism of the individual nanoparticles and has magnetoresistive sensitivity exceeding either component.

## 5.2 Results and Discussion

### 5.2.1 Synthesis and Physical Characterization of Nanoparticles

$CoFe_2O_4$ and $Fe_3O_4$ nanoparticles were synthesized according to modified literature procedures.[23-25] Complexes of Fe(III) or Fe(III)/Co(II) oleate were decomposed in the presence of oleic acid in octadecene. The resulting nanoparticles were washed through precipitation with ethanol and centrifugation. Transmission electron microscopy (TEM) revealed monodisperse spherical nanoparticles of $CoFe_2O_4$ ($d$ = 13.4±1.4 nm) and $Fe_3O_4$ ($d$ = 7.8±0.8 nm) (Figure 5.1c,d). Powder-averaged X-ray diffraction (pXRD) data are consistent with the inverse spinel crystal structure of $AB_2O_4$ ferrites (Figure 5.5). These synthetic components were chosen as our initial formulation to balance three factors: (1) the components possessed size, shape, and size distribution homogeneity to maximize the chances of a random mixture upon deposition, (2) nanoparticle sizes were small enough to expect significant $\Delta R/R_{max}$ (%) according to our previously observed size dependence,[11] and (3) the coercivity difference between $CoFe_2O_4$ and $Fe_3O_4$ was large enough to impose a definitive spin valve effect.

### 5.2.2 Fabrication of Nanoparticle Magnetoresistance Devices

In layered devices, the pseudo spin valve effect is achieved by deposition of three different material layers (hard, spacer, and soft), a process complicated by lattice mismatch and interdiffusion between layers. In this granular system, the interfaces between hard and soft materials are created simply by the intimate mixing of $Fe_3O_4$ and $CoFe_2O_4$ nanoparticles in colloidal suspensions. Hexane suspensions of $Fe_3O_4$ and $CoFe_2O_4$ of equal concentration (4 mg/mL) were mixed in the desired proportion by volume (1:0, 3:1, 1:1, 1:3, and 0:1 $CoFe_2O_4$:$Fe_3O_4$). These mixed suspensions were subsequently stripped of their native oleic acid ligands by treatment with $NOBF_4$ in dichloromethane[26] in order to improve the conductivity of the final nanoparticle films. Devices for MR measurements were formed by dropcasting films from dimethylformamide suspension onto lithographically patterned gold electrodes on silicon substrates (Figure 5.6). Energy-dispersive X-ray spectroscopy shows an even distribution of both cobalt and iron throughout the films (Figure 5.7), consistent with a lack of segregation of $CoFe_2O_4$ and $Fe_3O_4$ nanoparticles upon deposition.

### 5.2.3 Magnetic Characterization of the Constituent Nanoparticles

A pseudo spin valve requires that hard and soft materials have individual coercive fields as different as possible and that the composite material lacks exchange coupling between the materials. Thus, magnetic measurements were performed to characterize the individual $CoFe_2O_4$ and $Fe_3O_4$ nanoparticle magnetic characteristics. Ideally, $CoFe_2O_4$ (our hard material) should have a maximal coercive field and remanent moment, while $Fe_3O_4$ (our soft material) should have a low coercive field, high susceptibility, and large saturation moment. The pure $CoFe_2O_4$ and $Fe_3O_4$ nanoparticle films were characterized by measuring magnetic moment vs field between −7 and 7 T at 200 K. The soft magnetic character of the $Fe_3O_4$ sample is shown by the negligible coercive field and steep saturation of its moment in Figure 5.2e. Conversely the magnetically hard $CoFe_2O_4$ sample (Figure 5.2a) has a coercive field of nearly 0.5 T and retains 40% of its moment at $H = 0$ T. Saturation magnetizations for nanoparticles of $CoFe_2O_4$ ($M_S$ = 56 emu/g) and $Fe_3O_4$ ($M_S$ = 63 emu/g) are slightly reduced compared to the ideal bulk values of $M_S$ = 85 and 92 emu/g,

respectively, due to their increased surface to volume ratio. Magnetic effects associated with size reduction are somewhat beneficial for $Fe_3O_4$ nanoparticles, as their coercivity is diminished, making them an ideal candidate for the soft component of the spin valve. Size reduction does limit the coercivity of the $CoFe_2O_4$ nanoparticles, however, especially at high temperatures. To mitigate the lowering of the coercivity, magnetic and resistance characterization was performed at 200 K, enhancing the coercivity difference between $CoFe_2O_4$ and $Fe_3O_4$ components while still working within a reliable resistance range for our instrumentation (10 kΩ to 1 GΩ). Future optimization to study the effects of enhancing these characteristics will involve larger particles, stronger intrinsic magnetic phases, and oriented deposition. Nanoparticle films deposited for magnetoresistance measurements show magnetic characteristics consistent with restrained powders of the as-synthesized nanoparticles, indicating that ligand exchange and film processing causes minimal magnetic alteration (Figure 5.8).

The effect of mixed-particle film formation on magnetic properties was studied by measuring magnetic moment vs field at 200 K. Each mixed film displays characteristics of the parent nanoparticles in

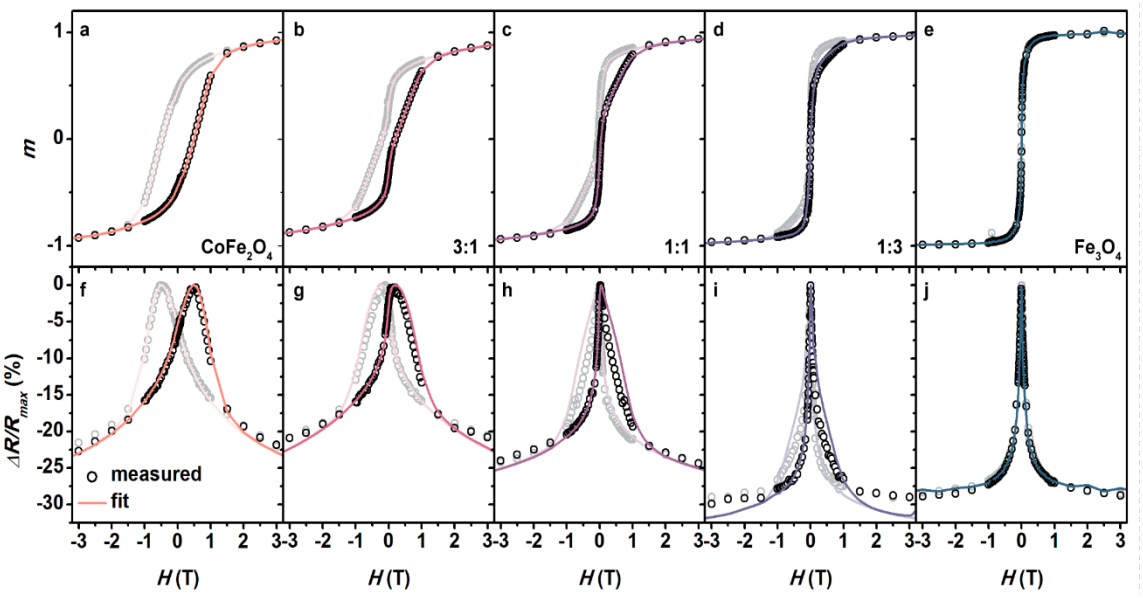


**Figure 5.2.** (Top row, a–e) Reduced magnetization (magnetization normalized to the saturation value, circles) at 200 K vs magnetic field for a series of nanoparticle films with composition varying from pure $CoFe_2O_4$ to pure $Fe_3O_4$. Plots for the mixed composition films show agreement with a mass-weighted linear combination (colored lines) of the magnetizations of the component nanoparticles. (Bottom row, f–j) $\Delta R/R_{max}$ (%) (circles) for films at 200 K with fits to Equation 5.1 (lines). The reverse scans (+7 to –7 T) in each plot are faded to enhance the clarity of the plots.

proportion to their composition. The 3:1 film shows an open hysteresis loop similar to the pure $CoFe_2O_4$ film, but with significantly increased low-field susceptibility due to the addition of $Fe_3O_4$ (Figure 5.2b). The low-field susceptibility of the multi-component films was further enhanced by increasing the $Fe_3O_4$ content. Tracking the experimental moment vs field behavior of the mixed films with a simple model using a linear combination of mass-weighted individual $CoFe_2O_4$ and $Fe_3O_4$ moments demonstrated that cooperative magnetic effects between nanoparticles are negligible. The linear combinations were performed by allowing the mass fraction of $CoFe_2O_4$ to vary in order to optimize the fit to the measured curve. The best fits (Figure 5.2b–d) resulted from $Fe_3O_4$ mass fractions of 0.18, 0.46, and 0.79, reasonable matches to the 3:1, 1:1, and 1:3 $CoFe_2O_4$:$Fe_3O_4$ ratios used in the suspensions from which the film was deposited. The agreement of the measured data with the linear combination indicates that the moments of the $CoFe_2O_4$ and $Fe_3O_4$ nanoparticles in the film are magnetically decoupled, which is key for maintaining sensitivity in pseudo spin valve magnetoresistance.

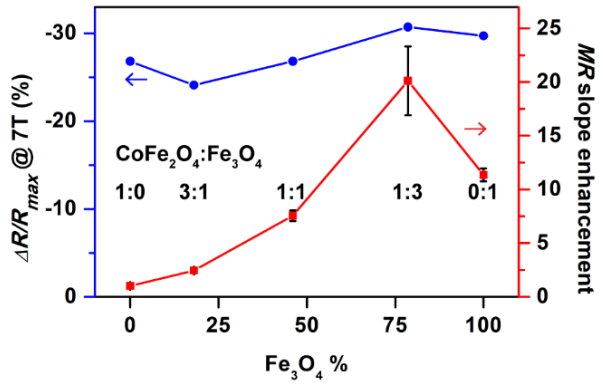


**Figure 5.3.** Dependence of the maximum MR and MR slope enhancement at 200 K on the $Fe_3O_4$ content. The MR slope enhancement is defined as the ratio of the maximum slope in $\Delta R/R_{max}$ vs $H$ of a sample, compared to the maximum slope of the $CoFe_2O_4$ film. The $Fe_3O_4$ wt% of each film was determined by fitting its magnetization curve to a mass-weighted linear combination of the pure components' magnetization curves, as shown in the top row of Figure 5.2. Error bars correspond to the 95% confidence interval of the slope in the linear fit of the $\Delta R/R_{max}$ vs $H$ for a given sample; the error for the 1:0 and 3:1 composites is smaller than their symbols.

At 200 K, the films of each composition were subjected to $H = -7$ T, and their resistance was measured as the magnetic field was increased to $H = 7$ T (Figure 5.2f–j). Each film reaches its minimal resistance at large positive and negative fields, reflecting their maximally aligned magnetic state ($m \approx \pm 1$).

As the magnetization of the films approaches zero at small fields (the minimally aligned magnetic state, $m = 0$; $H = H_C$), their resistance reaches its maximum. While the MR of the magnetically hard $CoFe_2O_4$ film shows a gradual change in resistance across the entire field range and a separation between forward and reverse scans, the soft $Fe_3O_4$ film peaks sharply at zero field and has no distinction between the two scan directions due to the $Fe_3O_4$ nanoparticles' lack of magnetic hysteresis. This sharp change in resistance near $H = 0$ T gives the $Fe_3O_4$ film a high low-field sensitivity, but the $CoFe_2O_4$ film has the advantage of more distinct on/off states due to the separation of its resistance peaks and the minimal change in its resistance around its peak value.

Each multi-component film displays a pseudo spin valve type magnetoresistance with characteristics of both the hard $CoFe_2O_4$ and soft $Fe_3O_4$. For example, adding approximately 25% $Fe_3O_4$ to $CoFe_2O_4$ increases the low-field sensitivity (measured by the maximum slope of the $\Delta R/R_{max}$ vs $H$ plots in the bottom row in Figure 5.2, and plotted in Figure 5.3) of the film while retaining much of the hysteretic character of the $CoFe_2O_4$. Further addition of $Fe_3O_4$ further enhances the low-field sensitivity of the films. Qualitatively, the *MR* curves of the multi-component films in Figure 5.2 appear to vary continuously between the properties of the $CoFe_2O_4$ and $Fe_3O_4$ films, which is confirmed by their fit to

$$\frac{\Delta R}{R} = Am^2 \qquad \textbf{Equation 5.1}$$

which describes the tunneling magnetoresistance of granular materials;[27] $A$ is a proportionality constant and $m$ is the reduced magnetization, which serves as a convenient measure of the relative alignment of the nanoparticles in the film. The match between the measured magnetoresistance of the film and Equation 5.1, shown in the bottom row of Figure 5.2, demonstrates the ability to tune the magnetoresistance behavior of a granular material by controlling its composition. Our ability to predict the MR behavior of these multi-component nanoparticle films from their magnetic properties, and to predict the films' collective magnetic properties from the individual components' magnetic properties, demonstrates the modularity of this approach to designing magnetoresistive materials.

Comparing the maximum $\Delta R/R_{max}$ (achieved at $H = \pm 7$ T) and the maximum slope of the MR curves at different film compositions in Figure 5.3 confirms the monotonic variation of the properties of the multi-component films. The maximum slope was measured from a linear fit to the steepest section of the MR curves covering a decrease in resistance of 5%, which in all cases occurred around $H = 0$ T. The criterion of a 5% decrease in resistance was chosen to prevent noise in the data from generating artificially high slopes. Interestingly, the pure $CoFe_2O_4$ and $Fe_3O_4$ films do not conform to the trend of the multi-component films exactly. An exciting development is the slope of the 3:1 $Fe_3O_4$:$CoFe_2O_4$ film nearly doubling the slope of the $Fe_3O_4$, showing that these multi-component films are not constrained between the properties of their parent materials (Figure 5.3, Figure 5.9). This improvement in the sensitivity of the composite material beyond the $Fe_3O_4$ is a clear indication of the spin valve structure suggested in Figure 5.1.

Comparison of the magnetoresistance curves in Figure 5.2f–j with the scheme in Figure 5.1b or with data from multilayer devices reveals that the nanocomposite films in this work do not reach the full

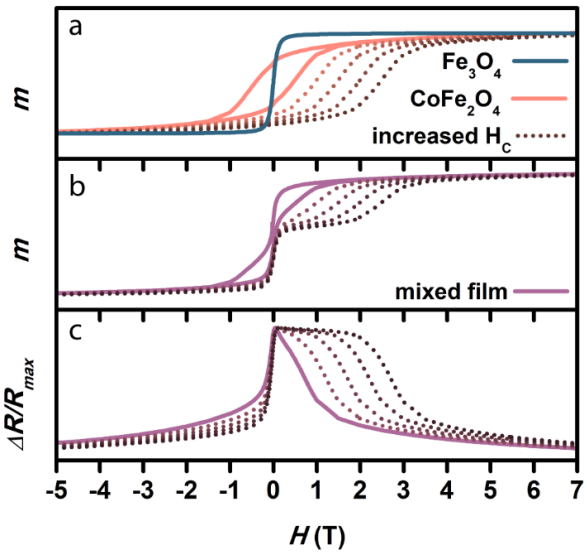


**Figure 5.4.** Demonstration of the modular design of pseudo spin valve nanocomposites. a) The reduced magnetization vs field hysteresis loops of $Fe_3O_4$ and $CoFe_2O_4$ nanoparticles (solid lines) is shown along with theoretical forward scans of hard materials with increasing $H_C$ (dotted lines). b) The resulting magnetization behavior of mixtures of nanoparticles of $Fe_3O_4$ with the $CoFe_2O_4$ (solid lines) or increased $H_C$ materials (dotted lines), generated from the sum of the individual component curves in a). c) Magnetoresistance curves of the nanocomposites, based on Equation 1, showing that increased $H_C$ materials improve both the low-field sensitivity and the distinction between on and off states of the magnetoresistors.

potential of a pseudo spin valve. However, the lack of magnetic coupling between components, demonstrated by the additive moment vs field curves in Figure 5.2b–d, indicates that the nanocomposites can be improved simply by modifying their components. Figure 5.4 demonstrates the effect of substituting the $CoFe_2O_4$ with a more coercive material, generated by shifting the forward scan of the $CoFe_2O_4$ moment to the right. The increased coercive field of the new material induces a more stepwise increase in the moment of the mixed film (Figure 5.4b), resulting in a sharper increase in resistance from small negative fields to $H = 0$ T. The increased $H_C$ materials also preserve a plateau in resistance at small positive fields, which is important for creating distinct on and off states of the nanocomposite magnetoresistor. From this basic calculation, it can be predicted that improving the hard material's coercivity from 0.5 T to 1.5 T would generate the desired resistance plateau. It is clear that with improved magnetic nanoparticle building blocks, even more sensitive magnetoresistors can be constructed without further engineering.

## 5.3 Conclusions

In this study, magnetically hard $CoFe_2O_4$ and soft $Fe_3O_4$ nanoparticles were prepared and mixed in varying ratios to mimic the pseudo spin valve magnetoresistance of layered materials with 'hard' and 'soft' layers. Our results show that magnetoresistive materials can be designed in a modular fashion; a multi-component material's magnetoresistive properties are predicted by its magnetic behavior, which in turn is determined by its components' properties. Furthermore, this combination of materials results in emergent properties, such as the 1:3 $CoFe_2O_4$:$Fe_3O_4$ film having a maximum slope in its MR nearly double that of the $Fe_3O_4$ film alone; it also offers a route to convenient modification of materials, as in the improved sensitivity of the 3:1 $CoFe_2O_4$:$Fe_3O_4$ film compared to the pure $CoFe_2O_4$, while maintaining its hysteretic character. This work demonstrates the ease with which this type of colloidally prepared nanoparticle material can be used to screen materials and their mixtures.

## 5.4 Experimental

### 5.4.1 Materials

The nanoparticle synthesis reagents used were cobalt(II) chloride hexahydrate (98%, Sigma Aldrich), iron(III) chloride hexahydrate (97% Alfa Aesar), sodium oleate (97% TCI), oleic acid (90%, Alfa Aesar), and 1-octadecene (90% Sigma Aldrich). Nitrosonium tetrafluoroborate ($NOBF_4$, 98%) was purchased from Alfa Aesar. HPLC grade dichloromethane (DCM), and ACS grade acetone, hexane, ethanol, isopropanol and toluene were purchased from Fisher. ACS grade Dimethyl formamide (DMF) was purchased from EMD Millipore. All chemicals were used as received.

### 5.4.2 Synthesis of Metal Oleate Precursors

The iron oleate and cobalt/iron mixed oleate were synthesized according to literature procedures.[23-24] Iron(III) chloride hexahydrate (8.1 g, 30 mmol) and sodium oleate (27.4 g, 90 mmol), or a 1:2 molar mixture of cobalt(II) chloride hexahydrate (2.4 g, 10 mmol) and iron(III) chloride hexahydrate (5.4 g, 20 mmol) and sodium oleate (24.4 g, 80 mmol) were combined in a solvent mixture of water (45 mL), ethanol (60 mL), and hexane (105 mL). This reaction mixture was brought to reflux (60$^{o}$C) for 4 h. After being cooled to room temperature, the upper organic layer was washed with water (30 mL) three times. Finally, hexane was evaporated from the product, leaving the viscous, oily metal oleate complex. The cobalt/iron mixed oleate was aged for a month in the dark at room temperature before being used in nanoparticle synthesis.

### 5.4.3 Synthesis of $CoFe_2O_4$ and $Fe_3O_4$ Nanoparticles

$CoFe_2O_4$ and $Fe_3O_4$ nanoparticles were synthesized according to modified literature procedures.[23-25] Iron or cobalt/iron oleate (1.4 mmol) was mixed with oleic acid (0.2 g, 0.7 mmol for $CoFe_2O_4$, 1 g, 3.5 mmol for $Fe_3O_4$) and 1-octadecene (7 g) in a 50 mL three-neck Morton flask. The reaction mixture was degassed under vacuum at 110$^{o}$C for 1 h, after which the atmosphere was backfilled with dinitrogen. Throughout the rest of the reaction, 100 sccm of dinitrogen was flowed through the reaction system into a

side neck of the Morton flask and out the condenser attached to the middle neck. The reaction mixture was heated to 320ºC at 3ºC/min, where it was refluxed for 0.5 h then cooled to room temperature. When the temperature reached 318ºC, 5 sccm of dioxygen was added to the dinitrogen stream and flowed continuously to the end of the reaction.

The resulting nanoparticles were isolated from the other reaction byproducts by addition of hexane (25 mL) and ethanol (40 mL). The nanoparticles were collected by centrifugation at 8500 rpm and redispersed in hexane (10 mL). After another cycle of precipitation with ethanol and centrifugation, the nanoparticles were stored in hexane.

### 5.4.4 Ligand Exchange of Nanoparticles and Deposition into Films

The nanoparticles were stripped of their long-chain organic ligands according to a modified literature procedure.[26] Hexane suspensions of $CoFe_2O_4$ and $Fe_3O_4$ nanoparticles were diluted to 4 mg/mL. The two suspensions were then mixed in 1:3, 1:1, and 3:1 ratios by volume. A 1 mL aliquot of each hexane suspension was concentrated by evaporating approximately half the volume of hexane with flowing dinitrogen. About 2 mL of a saturated solution of $NOBF_4$ in DCM was added to the concentrated suspension, which was then shaken until the nanoparticles visibly flocculated. The nanoparticles were collected with a magnet and the supernatant was discarded; they were then redispersed in DMF and precipitated out by addition of toluene. This final precipitate was redispersed in DMF (1 mL) at a concentration of 4 mg/mL for storage and deposition.

Substrates with gold electrode patterns were cleaned by a 10 min. sonication each in acetone then isopropanol. The substrates were dried and placed on a 60ºC hotplate. 3 µL of a DMF suspension of a given nanoparticle mixture was then dropcast onto a substrate, drying within a few minutes. The films were then fully dried under vacuum at 150ºC for 1.5 h

### 5.4.5 Deposition of Gold Electrodes on Silicon Substrates

Gold electrodes on silicon substrates were patterned at the Nano3 cleanroom at the San Diego Nanotechnology Infrastructure (SDNI) of UCSD. AZ1518MIF photoresist was spun onto a 4” silicon

wafers with 300 nm of thermal oxide. The wafer was exposed to the pattern in Figure 5.6, on a Karl Suss MA6 Mask Aligner and developed with AZ MIF 300. Finally, approximately 10 nm of a Ti adhesion layer and 100 nm of Au were sputtered onto the wafer in an AJA DC sputter deposition tool, with final lift-off done in acetone.

### 5.4.6 Characterization

Transmission electron microscopy (TEM) was performed with an FEI Spirit TEM operating at 120kV, with images collected by a 2k x 2k Gatan CCD camera. Samples were prepared by air-drying a dilute hexane solution of nanoparticles on carbon-coated copper grids. Particle sizes were analyzed using ImageJ using the Huang thresholding algorithm on sample sizes of N = 747, and 3,578 for $CoFe_2O_4$ and $Fe_3O_4$.[28] Scanning electron microscopy (SEM) and energy-dispersive X-ray spectroscopy (EDS) was performed with a Zeiss Sigma 500. Magnetic and magnetoelectric measurements were performed using a Quantum Design MPMS3 SQUID Magnetometer equipped with an Electrical Transport Option. Powder X-ray diffraction (XRD) was performed on a Bruker Diffractometer with a Mo K$\alpha$ radiation source and an Apex II Area Detector. The XRD patterns were fit using FullProf[29].

## 5.5 Acknowledgements

The authors would like to thank Han Nguyen and the UCSD Crystallography Facility for his assistance with fitting of powder XRD data. This research was funded through the Office of Naval Research Young Investigator Award N00014-16-1-2917. This work was performed in part at the San Diego Nanotechnology Infrastructure (SDNI) of UCSD, a member of the National Nanotechnology Coordinated Infrastructure, which is supported by the National Science Foundation (Grant ECCS-1542148).

Chapter 5 is a reformatted reprint from the manuscript entitled “Pseudo Spin Valve Behavior in Prepared Nanoparticle Films” by Zhou, B.H. and Rinehart, J.D. The dissertation author was the primary researcher and author of this paper. Reprinted with permission from *ACS Appl. Electron. Mater.* **2019**, *1*,1065–1069. Copyright 2019 American Chemical Society.

## 5.6 Additional Figures

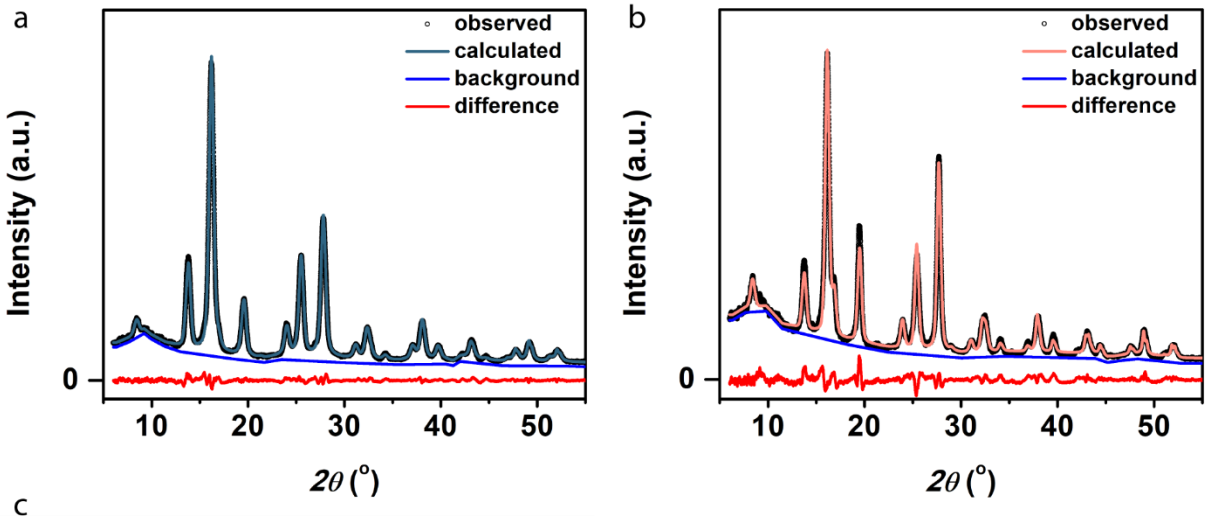


c

| sample | $R_b$ | $R_{wp}$ | $a_{observed}$ (Å) | $a_{reference}$ (Å) | Difference in *a* |
|---|---|---|---|---|---|
| $Fe_3O_4$ | 1.76 | 5.74 | 8.357(3) | 8.3941(7) (ICSD coll. code 26410) | −0.4384% |
| $CoFe_2O_4$ | 1.32 | 4.97 | 8.391(6) | 8.3860(3) (ICSD coll. code 192790) | 0.06642% |

**Figure 5.5.** Powder X-ray diffraction patterns of a) $Fe_3O_4$ and b) $CoFe_2O_4$ nanoparticles. The patterns were fit by the Le Bail method in FullProf,[29-30] with the fit parameters shown in c).

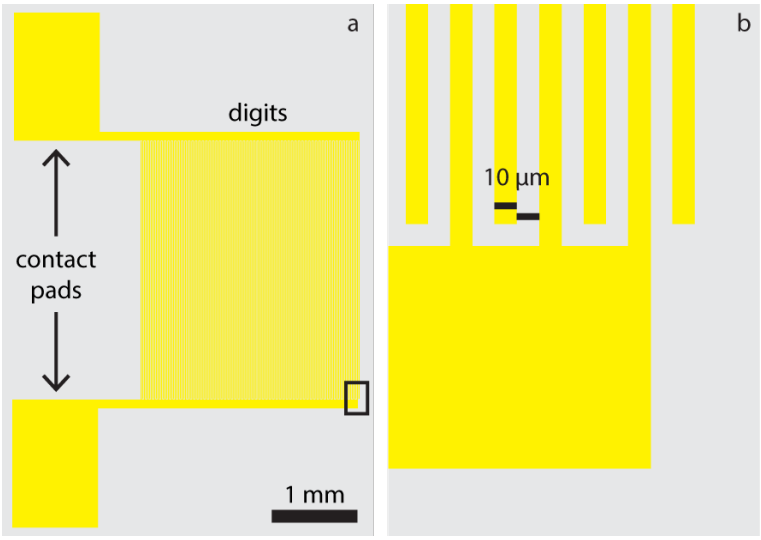


**Figure 5.6**. a) Overall schematic and b) detailed view (corresponding to the box in Figure 5.6a) of the interdigitated electrode pattern. The design consists of 64 digits per side, with 3 mm of overlapping length between digits. The spacing between the digits is 10 µm.

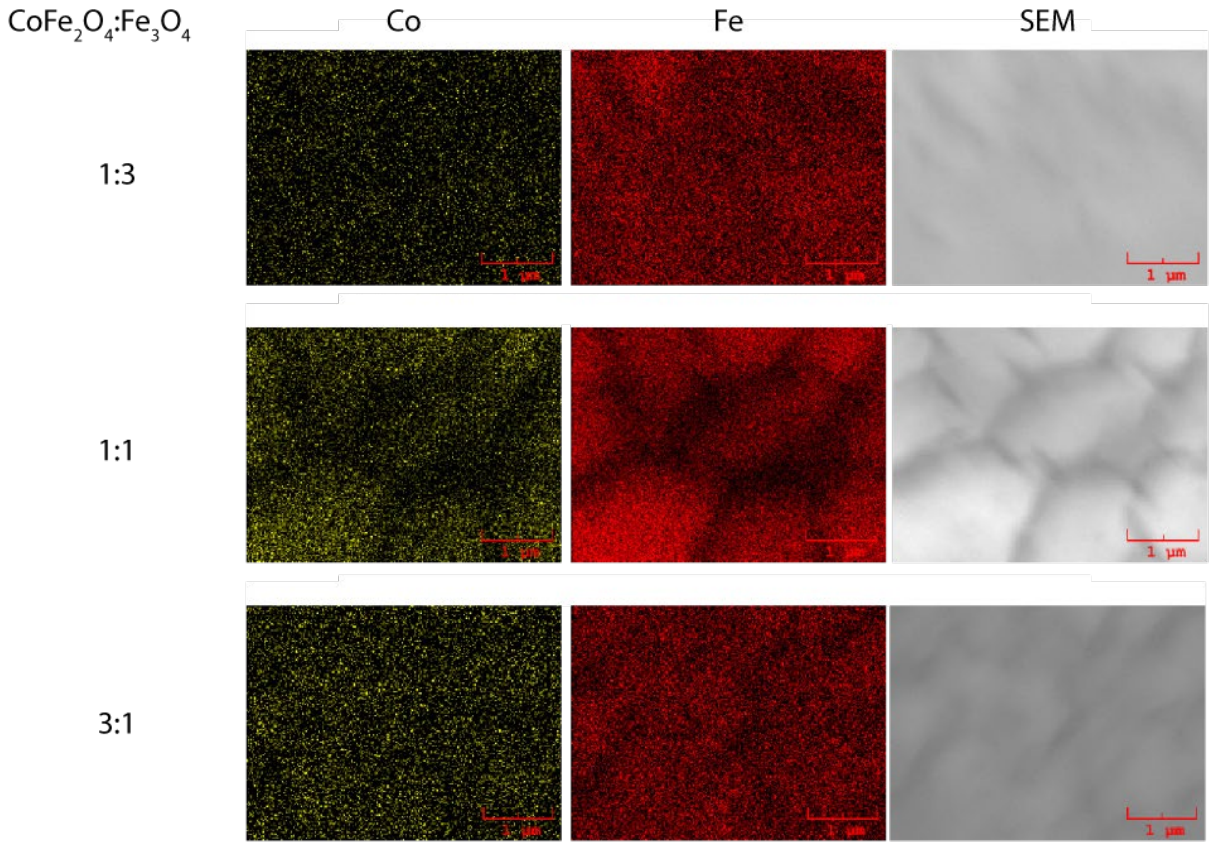


**Figure 5.7.** Energy dispersive X-ray spectroscopy element maps and corresponding scanning electron micrographs for the multi-component films.

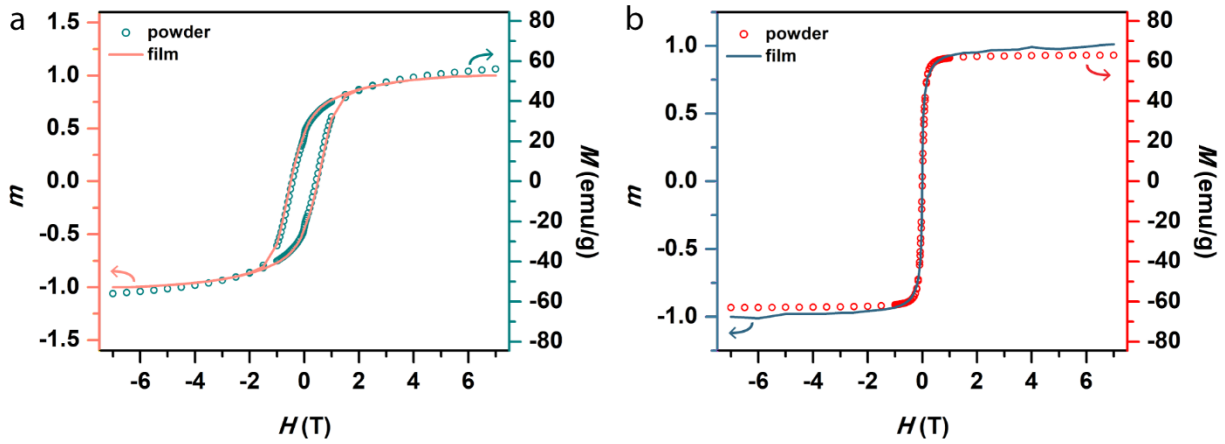


**Figure 5.8.** Magnetization and reduced magnetization vs magnetic field for a) $CoFe_2O_4$ and b) $Fe_3O_4$ nanoparticles. Circles and the right axes correspond to measurements performed on powders of the as-synthesized nanoparticles, while lines and the left axes correspond to measurements performed on the nanoparticles after ligand exchange and processing into films. The agreement between the powder and film data demonstrate the stability of the nanoparticles' properties throughout processing, as well as their retention of single particle properties. The powder and film data deviate from each other increasingly at larger fields; this is likely due to difficulty in accurately subtracting the diamagnetic contribution of the film substrate from the overall magnetic moment.

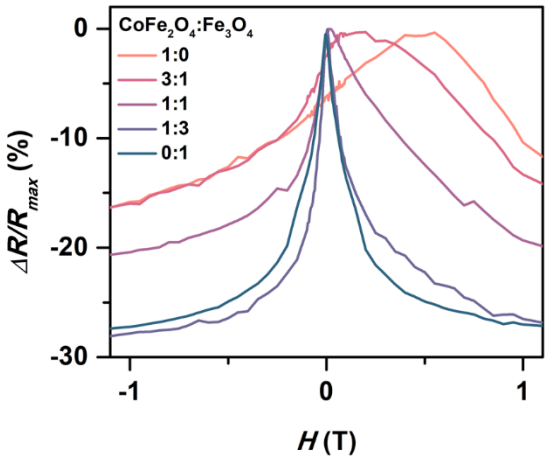


**Figure 5.9.** Overlaid plots of *ΔR/R* vs magnetic field (scanned from –7 to +7 T) at 200 K for each nanoparticle film. The combined figure emphasizes how sensitivity of the pure magnetite is improved through introduction of low-sensitivity cobalt ferrite due to the spin valve effect.

## 5.7 Reference


1. Baibich, M. N.; Broto, J. M.; Fert, A.; Vandau, F. N.; Petroff, F.; Eitenne, P.; Creuzet, G.; Friederich, A.; Chazelas, J., Giant Magnetoresistance of (001)Fe/(001) Cr Magnetic Superlattices. *Phys. Rev. Lett.* **1988,** *61* (21), 2472-2475.

2. Binasch, G.; Grunberg, P.; Saurenbach, F.; Zinn, W., Enhanced Magnetoresistance in Layered Magnetic-Structures with Antiferromagnetic Interlayer Exchange. *Phys. Rev. B* **1989,** *39* (7), 4828-4830.

3. Berkowitz, A. E.; Mitchell, J. R.; Carey, M. J.; Young, A. P.; Zhang, S.; Spada, F. E.; Parker, F. T.; Hutten, A.; Thomas, G., Giant Magnetoresistance in Heterogeneous Cu-Co Alloys. *Phys. Rev. Lett.* **1992,** *68* (25), 3745-3748.

4. Coey, J. M. D.; Berkowitz, A. E.; Balcells, L.; Putris, F. F.; Barry, A., Magnetoresistance of Chromium Dioxide Powder Compacts. *Phys. Rev. Lett.* **1998,** *80* (17), 3815-3818.

5. Coey, J. M. D.; Berkowitz, A. E.; Balcells, L.; Putris, F. F.; Parker, F. T., Magnetoresistance of Magnetite. *Appl. Phys. Lett.* **1998,** *72* (6), 734-736.

6. Xiao, J. Q.; Jiang, J. S.; Chien, C. L., Giant Magnetoresistance in the Granular Co-Ag System. *Phys. Rev. B* **1992,** *46* (14), 9266-9269.

7. Xiao, J. Q.; Jiang, J. S.; Chien, C. L., Giant Magnetoresistance in Nonmultilayer Magnetic Systems. *Phys. Rev. Lett.* **1992,** *68* (25), 3749-3752.

8. Kohiki, S.; Nara, K.; Mitome, M.; Tsuya, D., Magnetoresistance of Drop-Cast Film of Cobalt-Substituted Magnetite Nanocrystals. *ACS Appl. Mater. Interfaces* **2014,** *6* (20), 17410-17415.

9. Kohiki, S.; Okada, K.; Mitome, M.; Kohno, A.; Kinoshita, T.; Iyama, K.; Tsunawaki, F.; Deguchi, H., Magnetic and Magnetoelectric Properties of Self-Assembled $Fe_{2.5}Mn_{0.5}O_4$ Nanocrystals. *ACS Appl. Mater. Interfaces* **2011,** *3* (9), 3589-93.

10. Wang, T.; Luan, Z. Z.; Ge, J. Y.; Liu, L.; Wu, D.; Lv, Z. P.; Zuo, J. L.; Sun, S. H., Enhancing Low-Field Magnetoresistance in Magnetite Nanoparticles via Zinc Substitution. *Phys. Chem. Chem. Phys.* **2018,** *20* (25), 17245-17252.

11. Zhou, B. H.; Rinehart, J. D., A Size Threshold for Enhanced Magnetoresistance in Colloidally Prepared CoFe2O4 Nanoparticle Solids. *ACS Cent. Sci.* **2018,** *4* (9), 1222-1227.

12. Mitra, A.; Barick, B.; Mohapatra, J.; Sharma, H.; Meena, S. S.; Aslam, M., Large Tunneling Magnetoresistance in Octahedral $Fe_3O_4$ Nanoparticles. *AIP Adv.* **2016,** *6* (5), 055007.

13. Lv, Z. P.; Luan, Z. Z.; Cai, P. Y.; Wang, T.; Li, C. H.; Wu, D.; Zuo, J. L.; Sun, S. H., Enhancing Magnetoresistance in Tetrathiafulvalene Carboxylate Modified Iron Oxide Nanoparticle Assemblies. *Nanoscale* **2016,** *8* (24), 12128-12133.

14. Lv, Z. P.; Luan, Z. Z.; Wang, H. Y.; Liu, S.; Li, C. H.; Wu, D.; Zuo, J. L.; Sun, S. H., Tuning Electron-Conduction and Spin Transport in Magnetic Iron Oxide Nanoparticle Assemblies via Tetrathiafulvalene-Fused Ligands. *ACS Nano* **2015,** *9* (12), 12205-12213.

15. Lv, Z.-P.; Wang, T.; Ge, J.-Y.; Luan, Z.-Z.; Wu, D.; Zuo, J.-L.; Sun, S., Controlling the Assembly and Spin Transport of Tetrathiafulvalene Carboxylate Coated Iron Oxide Nanoparticles. *J. Mater. Chem. C* **2017,** *5* (29), 7200-7206.

16. Kohiki, S.; Kinoshita, T.; Nara, K.; Akiyama-Hasegawa, K.; Mitome, M., Large, Negative Magnetoresistance in an Oleic Acid-Coated $Fe_3O_4$ Nanocrystal Self-Assembled Film. *ACS Appl. Mater. Interfaces* **2013,** *5* (22), 11584-11589.

17. Wang, S.; Yue, F. J.; Wu, D.; Zhang, F. M.; Zhong, W.; Du, Y. W., Enhanced Magnetoresistance in Self-Assembled Monolayer of Oleic Acid Molecules on $Fe_3O_4$ Nanoparticles. *Appl. Phys. Lett.* **2009,** *94* (1), 012507.

18. Dieny, B.; Speriosu, V. S.; Gurney, B. A.; Parkin, S. S. P.; Wilhoit, D. R.; Roche, K. P.; Metin, S.; Peterson, D. T.; Nadimi, S., Spin-Valve Effect in Soft Ferromagnetic Sandwiches. *J. Magn. Magn. Mater.* **1991,** *93*, 101-104.

19. Dieny, B., Giant Magnetoresistance in Spin-Valve Multilayers. *J. Magn. Magn. Mater.* **1994,** *136* (3), 335-359.

20. Del Bianco, L.; Spizzo, F.; Tamisari, M.; Allia, P., Magnetoresistance of Nanogranular Ni/NiO Controlled by Exchange Anisotropy. *J. Magn. Magn. Mater.* **2013,** *339*, 94-99.

21. Chen, J.; Ye, X.; Oh, S. J.; Kikkawa, J. M.; Kagan, C. R.; Murray, C. B., Bistable Magnetoresistance Switching in Exchange-Coupled $CoFe_2O_4$-$Fe_3O_4$ Binary Nanocrystal Superlattices by Self-Assembly and Thermal Annealing. *ACS Nano* **2013,** *7* (2), 1478-86.

22. Anil Kumar, P.; Ray, S.; Chakraverty, S.; Sarma, D. D., Engineered Spin-Valve Type Magnetoresistance in $Fe_3O_4$-$CoFe_2O_4$ Core-Shell Nanoparticles. *Appl. Phys. Lett.* **2013,** *103* (10), 102406.

23. Park, J.; An, K. J.; Hwang, Y. S.; Park, J. G.; Noh, H. J.; Kim, J. Y.; Park, J. H.; Hwang, N. M.; Hyeon, T., Ultra-Large-Scale Syntheses of Monodisperse Nanocrystals. *Nat. Mater.* **2004,** *3* (12), 891-895.

24. Herrera, A. P.; Polo-Corrales, L.; Chavez, E.; Cabarcas-Bolivar, J.; Uwakweh, O. N. C.; Rinaldi, C., Influence of Aging Time of Oleate Precursor on the Magnetic Relaxation of Cobalt Ferrite Nanoparticles Synthesized by the Thermal Decomposition Method. *J. Magn. Magn. Mater.* **2013,** *328*, 41-52.

25. Unni, M.; Uhl, A. M.; Savliwala, S.; Savitzky, B. H.; Dhavalikar, R.; Garraud, N.; Arnold, D. P.; Kourkoutis, L. F.; Andrew, J. S.; Rinaldi, C., Thermal Decomposition Synthesis of Iron Oxide Nanoparticles with Diminished Magnetic Dead Layer by Controlled Addition of Oxygen. *ACS Nano* **2017,** *11* (2), 2284-2303.

26. Dong, A.; Ye, X.; Chen, J.; Kang, Y.; Gordon, T.; Kikkawa, J. M.; Murray, C. B., A Generalized Ligand-Exchange Strategy Enabling Sequential Surface Functionalization of Colloidal Nanocrystals. *J. Am. Chem. Soc.* **2011,** *133* (4), 998-1006.

27. Inoue, J.; Maekawa, S., Theory of Tunneling Magnetoresistance in Granular Magnetic Films. *Phys. Rev. B* **1996,** *53* (18), R11927-R11929.

28. Schneider, C. A.; Rasband, W. S.; Eliceiri, K. W., NIH Image to ImageJ: 25 Years of Image Analysis. *Nat. Methods* **2012,** *9* (7), 671-675.

29. Rodríguez-Carvajal, J., Recent Advances in Magnetic Structure Determination by Neutron Powder Diffraction. *Phys. B: Condens. Matter* **1993,** *192* (1-2), 55-69.

30. Le Bail, A., Whole Powder Pattern Decomposition Methods and Applications: A Retrospection. *Powder Diffr.* **2012,** *20* (4), 316-326.